University of Nevada, Reno

Using Copper Nanoparticle Additive to Improve the Performance of Silicon Anodes in Lithium-Ion Batteries

A thesis submitted in partial fulfillment of the requirements for the degree of
Master of Science in Materials Science and Engineering

By

Gabrielle Bachand

Dr. Dev Chidambaram / Thesis Advisor

December, 2017

© by Gabrielle Bachand 2017
All Rights Reserved

THE GRADUATE SCHOOL

We recommend that the thesis
prepared under our supervision by

GABRIELLE BACHAND

entitled

Using Copper Nanoparticle Additive to Improve the Performance of Silicon Anodes in Lithium-Ion Batteries

be accepted in partial fulfillment of the
requirements for the degree of

MASTER OF SCIENCE

Dr. Dev Chidambaram, Advisor

Dr. Dhanesh Chandra, Committee Member

Dr. Indira Chatterjee, Graduate School Representative

David W. Zeh, Ph.D., Dean, Graduate School

December, 2017

Abstract

In the foreseeable future, global energy demand is expected to rapidly increase as a result of the swelling population and higher standards of living. Current energy generation and transportation methods predominantly involve the combustion of non-renewable fossil fuels, and greenhouse gas emissions from these processes have been shown to contribute to global climate change and to be detrimental to human and environmental health. To satisfy future energy needs and to reduce greenhouse gas emissions, the advancement of renewable energy generation and electric vehicles is important. The proliferation of intermittent renewable energy sources (such as solar and wind) and electric vehicles depends upon reliable, high-capacity energy storage to serve the practical needs of society. The present-day lithium-ion battery offers excellent qualities for this purpose; however, improvements in the capacity and cost-effectiveness of these batteries are needed for further growth.

As an anode material, silicon has exceptionally high theoretical capacity and is an earth-abundant, low-cost option. However, silicon also suffers from poor conductivity and long-term stability, prompting many studies to investigate the use of additive materials to mitigate these issues. This thesis focuses on the improvement of silicon anode performance by using a nanoparticulate copper additive to increase material conductivity and an inexpensive, industry-compatible anode fabrication process. Three main fabrication processes were explored using differing materials and heat treatment techniques for comparison. Anodes were tested using CR2032 type coin cells. The final anodes with the most-improved characteristics were fabricated using a high-temperature heating step for the anode material, and an additional batch was formed to test the viability of the copper additive functioning as a full substitute for carbon black, which is the traditional choice of conductive additive for electrode materials. Anodes materials were characterized using a variety of techniques including scanning electron microscopy (SEM), electron dispersive spectroscopy (EDS), inductively coupled plasma optical emission spectrometry (ICP-OES), Raman spectroscopy, and X-ray diffraction (XRD) to evaluate surface qualities and material content. Electrochemical techniques including electrochemical impedance spectroscopy (EIS) and charge/discharge cycling were also used to determine the conductivity and functional behavior of the anode materials.

Anodes from the final experimental study achieved initial capacities of 309 mAg^{-1} and 957 mAg^{-1} for the silicon-only control and silicon with copper additive anodes, respectively, demonstrating an over 300% increase in specific capacity. Si-Cu (NC) anodes also showed superior performance over control anodes with an initial capacity of 775 mAg^{-1}. For all three anodes, high efficiencies of over 96% were achieved for the testing duration of 100 cycles and reached near or over 99% in final cycles. Results also show a significant decrease in the resistance of anodes with copper additive, contributing to the improved performance of these anodes.

Acknowledgements

My deepest gratitude is extended to the many individuals who contributed their time, knowledge, and support to this study. I thank my advisor, Dr. Dev Chidambaram for the opportunity to pursue this work and for his guidance throughout this process. His insight and experience have been invaluable to the progress of this work and to my education. I also thank my committee members for their time and expertise: I am grateful to have been a student of Dr. Dhanesh Chandra and to have had the encouragement of Dr. Indira Chatterjee throughout my collegiate career.

This research was supported by the Office of Vice President for Research Innovation at the University of Nevada, Reno via an AIRE grant. Characterization of electrodes was conducted by Materials Characterization Nevada.

I thank Zachary Karmiol and Dr. Joel DesOrmeau for their technical assistance with SEM-EDS analysis. I thank Akira Nordmeier for his assistance in ICP-OES analysis and for his consideration in answering my many, many questions. I thank Vickram Singh for his assistance in Raman analysis. I am appreciative of all members of the MER Lab for their knowledge and advice including Mackenzie Parker, Mary Lou Lindstrom, William Phillips, Kodi Summers, James Mulcahy, Jeremy Moon, Jared Olson, Gabriel Martins, Chris Bruneau, Sarah Yang, and Dr. Thorunn Snorradottir. I thank Dr. Augustus Merwin and Dr. David Rodriguez for introducing me to this research group and to nitrogen ice cream.

I am honored to have been a part of the Engineering Communications teaching team throughout my graduate career, and I am especially grateful to Dr. Candice Bauer for her ever-present kindness and mentorship. I thank you for being my real-life fairy godmother. I appreciate Nicholas Maus, Jamie Fry, and Mirica Krajewski for all of the laughter, candy, and support. I thank you for being my second family.

Finally, I thank Shruti Arun for the afternoon tea breaks, the long hours of listening, and her unwavering friendship. I thank Nolan Nicholson for the delicious meals, the endless encouragement, and his wonderfulness through it all. I am forever grateful to my parents for providing every comfort and for their continuous support and love. I thank you for being my inspiration. Lastly, to Mr. Darcy, shown in Fig. 0. Thank you for waiting to walk until I finished working.

Fig. 0: Thank you to Mr. Darcy.

Table of Contents

Abstract i

Acknowledgements iii

List of Tables vii

List of Figures viii

Chapter 1: Introduction 1

- 1.1 Global Energy Requirements 1
  - 1.1.1 Energy Consumption 1
  - 1.1.2 Renewable Energy 2
- 1.2 Energy Storage 3
  - 1.2.1 Forms of Energy Storage 3
  - 1.2.2 Batteries 6
  - 1.2.3 Batteries for Electric Vehicles 8
- 1.3 Lithium-ion Batteries 11
  - 1.3.1 Functionality 11
  - 1.3.2 Research 18
- 1.4 Silicon-Based Anodes 19
  - 1.4.1 Silicon Anodes 19
  - 1.4.2 Carbon Additives 21
  - 1.4.3 Transition Metal Additives 22
  - 1.4.4 Copper Additives 23
  - 1.4.5 Current State of Research 28

Chapter 2: Experimental 30

- 2.1 Sample Preparation 30
  - 2.1.1 Low-Temperature Anodes 30
  - 2.1.2 Initial High-Temperature Anodes 34
  - 2.1.3 Final High-Temperature Anodes 37
- 2.2 Sample Characterization 44
  - 2.2.1 Scanning Electron Microscopy / Energy Dispersive Spectroscopy 44

    - 2.2.2 Inductively Coupled Plasma Optical Emission Spectrometry 45
    - 2.2.3 Raman Spectroscopy 46
    - 2.2.4 X-ray Diffraction 47
  - 2.3 Electrochemical Measurement 48
    - 2.3.1 Electrochemical Impedance Spectroscopy 48
    - 2.3.2 Charge/Discharge Cycle Testing 48
- Chapter 3: Results and Discussion 51
  - 3.1 Low-Temperature Anodes 51
  - 3.2 Initial High-Temperature Anodes 61
    - 3.2.1 Sample Characterization 61
    - 3.2.2 Electrochemical Measurement 65
  - 3.3 Final High-Temperature Anodes 69
    - 3.3.1 Sample Characterization 70
    - 3.3.2 Electrochemical Measurement 87
- Chapter 4: Conclusions 95
- Chapter 5: Future Work 98
- Scholarly Work 100
- References 101
- Appendix A: Silicon Anodes 110
- Appendix B: Fundamental Electrode Work 116
- Appendix C: Permission for Figure Publication 124

List of Tables

Table 1: Comparison of attributes of main battery types for energy storage...................... 7

Table 2: Materials and quantities for low-temperature anode study................................. 31

Table 3: Materials and quantities for initial high-temperature anode study. 35

Table 4: Materials and quantities for final high-temperature anode study. 38

Table 5: Weight percentages of silicon, oxygen, and copper for the Si only, Si-Cu, and Si-Cu (NC) anodes determined using EDS mapping analysis. Results confirm the low copper content present in Si-Cu and Si-Cu (NC) materials. 76

Table 6: ICP-OES results showing the copper content of the Si only, Si-Cu, and Si-Cu (NC) materials following the heat treatment process. 81

Table 7: Peak positions and identification from the XRD patterns for final high-temperature anodes with copper additive. 86

List of Figures

Fig. 1: Energy storage form comparison. The figure is an amalgamation of similar figures to compare the system power ratings, level of readiness for deployment, and efficiency of top energy storage technologies......................5

Fig. 2: Diagram illustrating the functionality of a Li-ion cell under charge and discharge conditions. The directional movement of the Li ions, electrons, and current is shown...14

Fig. 3: Basic structure of a CR2032-type coin cell with labeled components. Cathode, anode, and separator can vary in composition and appearance. 18

Fig. 4: The equilibrium phase diagram for the Si-Cu system is shown in the range of 65 to 90 atomic percent copper content. The enlargement illustrates the regions for the η, η’, and η” Cu_3Si phases [88]...25

Fig. 5: MTI Planetary ball mill used to reduce the particle size of dry material. The ball mill was operated for 30 minutes...32

Fig. 6: Image of a typical slurry cast using a Mayer rod onto a copper current collector foil. Application of the slurry should be smooth and without large grains or bubbles. This method was used throughout all studies...............33

Fig. 7: MTI vacuum oven used for low temperature heat treatment of the coated foils. Foils were heated at 120ºC for 12 hours. 34

Fig. 8: Image of coated foil curling over and held in place with a glass slide. Ethanol-based slurries exhibited curling during the drying process. 36

Fig. 9: MTI tube furnace used for high temperature heat treatment of the coated foils. Foils were annealed under argon for 700°C for 15 minutes. A graphite stage was made to keep the foils flat while inside the tube...................37

Fig. 10: Image showing the two $CuCl_2$ materials. The smaller grains of the $CuCl_2$ on the right did not require an additional milling step and mixed more homogeneously in the slurry. 38

Fig. 11: MTI disc punch for preparing separator discs from sheets of Celgard tri-layer PP/PE/PP membrane. Discs of 18 mm diameter were used. 40

Fig. 12: Glove box used for coin cell assembly. Glove box conditions were maintained with water and oxygen content less than 1.0 ppm. 41

Fig. 13: MTI electric crimper housed inside the glove box. Following assembly by hand, coin cells were crimped to seal contents. 42

Fig. 14: De-crimped coin cell after electrochemical testing with labeled components in assembly order. 43

Fig. 15: Hitachi S-4800 scanning electron microscope (SEM) and attached Oxford energy-dispersive X-ray spectroscopy (EDS) system used for surface characterization of the samples. 44

Fig. 16: PerkinElmer inductively couples plasma optical emission spectrometer (ICP-OES) 8000 used to assess the copper content of anode materials after heat treatment. 45

Fig. 17: Thermo Scientific DXR Raman Microscope used for characterization of the anode disc surfaces. Data were obtained at 10x magnification and a spot size of 50μm. 46

Fig. 18: Rigaku SmartLab X-ray diffractometer (XRD) used to characterize the anode samples. All patterns were collected over the range of $2\theta = 20°$ to $100°$ with a step size of 0.07º and at a scan rate of 0.5ºmin^{-1}.............................47

Fig. 19: MTI multichannel battery analyzer with attached laptop (above) and coin cell testing board (below). The laptop display shows the battery analyzer software used to program the test schedules for the eight channels. 49

Fig. 20: MTI coin cell testing board which houses eight coin cells. The board is an attachment to the battery analyzer. 50

Fig. 21: Example plot of the performance for three anodes of the same batch (low-temperature Si-Cu) for comparison. Noticeable variabilities exist between the different samples; therefore, the data from the most-average sample from the group (Sample 2 in this scenario) is used as a representative for the batch. 52

Fig. 22: Charge/discharge cycling results for 50 cycles for low-temperature Si only and Si-Cu anodes cycled at 250 mAg^{-1} current density. Initial capacities reached above 700 $mAhg^{-1}$ and 1000 $mAhg^{-1}$ for Si-only and Si-Cu anodes, respectively; however, capacity retention is poor for both materials with over 50% loss within the first 10 cycles. 53

Fig. 23: Coulombic efficiency results from the 50 cycles for low-temperature Si only and Si-Cu anodes. Efficiency behavior is shown to be erratic and have poor stability within the first 30 cycles. 54

Fig. 24: Charge/discharge cycling results for 50 cycles for Si only and Si-Cu ball-milled anodes cycled at 250 mAg^{-1} current density. Results are similar to the previous low-temperature anode results with significant immediate capacity loss. 56

Fig. 25: Coulombic efficiency results for the Si only and Si-Cu ball-milled anodes. Efficiency results are also similar to the initial low-temperature results. 57

Fig. 26: SEM images of the overall surfaces of the (a) Si only and (b) Si-Cu anodes at 30x magnification. Surfaces are grainy in texture, but large grains are dispersed evenly across the surface for both materials. 62

Fig. 27: SEM images showing the particle sizing and texture of the (a) Si only and (b) Si-Cu anodes at 20k-x magnification. Agglomerates of smaller particles ranging in size on the nanometer scale compose the base layer of the coating. Large copper particles are also found on the Si-Cu anode surface. 63

Fig. 28: EDS line scan of a copper particle on the anode surface at 40k-x magnification. Colored graphs show the elemental composition across the sample scan line through the particle, and they indicate a clear confirmation that the particle is copper against the primarily silicon base layer. 64

Fig. 29: Charge/discharge cycling results for 100 cycles for Si only and Si-Cu initial high-temperature anodes cycled at 250 mAg^{-1} current density. Though results yield lower initial capacity values than those of the low-temperature anodes, capacity retention and long-term stability is much improved. 66

Fig. 30: Coulombic efficiency results for the Si only and Si-Cu initial high-temperature anodes. Efficiency results show greater stability compared to low-temperature results and overall improvement over cycling duration. 67

Fig. 31: SEM images showing the particle sizing and texture of the (a) Si-Cu initial high-temperature and (b) Si-Cu final high-temperature anodes at 1k-x magnification and YAG BSE mode. The initial Si-Cu anode visibly has larger copper particles in greater amount than the final Si-Cu anode. 71

Fig. 32: SEM images using 20 kV accelerating voltage at 40k-x magnification of the anode surfaces prior to cycle testing for (a) Si only, (b) Si-Cu, (c) Si-Cu (NC). The initial surfaces of all three coatings show a similar, homogeneous dispersion of particles with an average size range from 5 nm to 20 nm. 73

Fig. 33: EDS elemental mapping of the dispersion of copper for the (a) Si-Cu and (b) Si-Cu (NC) samples at 40k-x magnification shows the confirmation of the integrated copper nanoparticles. Copper was uniformly distributed in the silicon-based coating. 75

Fig. 34: SEM images using 20 kV accelerating voltage at 30x magnification of the anode surfaces after cycle testing for (a) Si only, (b) Si-Cu, (c) Si-Cu (NC). 77

Fig. 35: SEM images using 20 kV accelerating voltage at 40k-x magnification of the anode surfaces after cycle testing for (a) Si only, (b) Si-Cu, (c) Si-Cu (NC). 78

Fig. 36: SEM images showing the surface characteristics of the Si-Cu final high-temperature anodes (a) before cycling and (b) after cycling at 1k-x magnification. 80

Fig. 37: Raman spectra of Si only, Si-Cu, and Si-Cu (NC) anode disc surface at 10x magnification. Silicon peaks are visible at 520 cm^{-1} and 950 cm^{-1}, and the prevalence of the amorphous carbon structure is shown from the D and G carbon bands at 1350 cm^{-1} and 1580 cm^{-1} in each of the three samples. 82

Fig. 38: XRD patterns of the Si only, Si-Cu, and Si-Cu (NC) materials between the range of $2\theta = 20°$ to 100°. Peaks indicating the presence of Si, Cu, and Cu_3Si were identified for anodes with copper additive. 84

Fig. 39: Narrower region of the XRD pattern for the Si-Cu (NC) material in the range of $2\theta = 40°$ to 60° shows the distinguished first and second Cu_3Si peaks. 85

Fig. 40: EIS curves of the experimental data for the sample anodes prior to cycle testing. Resistance values are 94.04 Ω, 55.39 Ω, and 57.28 Ω for the Si only, Si-Cu, and Si-Cu (NC) samples, respectively. Thus, the addition of copper leads to increased conductivity in anodes. 88

Fig. 41: Charge/discharge cycling results for 100 cycles for Si only and Si-Cu final high-temperature anodes cycled at 250 mAg^{-1} current density. Results show high initial capacity compared to previous high-temperature anodes, improved capacity retention compared to low-temperature anodes, and increased capacity for anodes with copper additive. 90

Fig. 42: Coulombic efficiency results for the Si only and Si-Cu final high-temperature anodes. Efficiency results show relative consistency between samples and overall improvement over the cycling duration. 91

Fig. 43: Compilation graph showing the specific capacities of all anode types from this study with respect to cycling. Final high-temperature anodes demonstrated high initial and final capacity with gradual capacity fade with cycle testing. 93

Chapter 1: Introduction

1.1 Global Energy Requirements

1.1.1 Energy Consumption

According to the U.S. Energy Information Administration, global energy consumption reached 575 quadrillion British thermal units (Btu) in 2015, and the value is predicted to increase by 28% (736 quadrillion Btu) by 2040 [1]. Energy consumption continues to increase rapidly due to two main factors: population growth and higher standards of living. World population stabilization is improbable for this century in the absence of a concerted effort [2], and energy consumption is proportional to the increased demand for higher living standards. As the population gains access to higher quality resources and technologies, more energy is required to fuel these needs. Due to the relationship between these two factors, the energy needed to sustain both increasing trends will require exponential growth in energy generation to meet future demand.

Currently, global energy demand is predominantly fulfilled using nonrenewable fossil fuels. From the World Energy Council 2016 Summary, 85% of global energy consumption in 2015 derived from a fossil fuel sources: this includes oil, natural gas, and coal [3]. Because fossil fuel sources are finite in supply, alternative energy sources will ultimately be necessary to sustain the expected increase in energy demand. Also of concern is that the extensive usage of fossil fuels has already increased global atmospheric levels of greenhouse gases and other pollutants, resulting in climate change. The adverse effects of climate change are well documented and manifest in many forms including global temperatures increasing, oceanic warming and acidification, global sea level rising, and natural disaster exacerbation [4]. Excessive greenhouse gas emissions pose substantial risks to human health; the direct consequences of emissions are increased risk of respiratory illnesses and cancer while an indirect consequence of climate change is an increase in mortality from natural disasters such as intense droughts, floods, storms, and wildfires [5, 6]. In addition to anticipated fossil fuel shortages in the future, these issues have prompted global initiatives to reduce fossil fuel consumption.

1.1.2 Renewable Energy

To meet future energy requirements and to reduce greenhouse gas emissions, substantial progress has been made in developing effective renewable energy technologies. Renewable energy sources, such as wind, solar, hydro, geothermal, and biomass, are advantageous over fossil fuels due to their essentially infinite supply and reduced environmental impact [7]. Technologies utilizing wind and solar sources are of special interest as they generate no appreciable emissions during operation throughout their lifetime. Though these technologies have existed in some form for centuries, modern renewable energy sources make-up only a small fraction of global energy generation at approximately 10% [3, 8]. Recent interest has stimulated notable growth in the field: between 2005 and 2015, total global energy generated from renewable sources increased by 1.75% [3]. Though hydropower and biomass are the largest contributors of power in the category by a wide margin, both wind and solar energy have shown exponential growth trends for energy generation within the past ten years [8]. Wind turbines and solar photovoltaic (PV) systems in particular have declined drastically in cost as higher-performing materials have become commercially available and financial incentives have been offered for installations.

Despite this growth, wind and solar energy generation methods are hampered by their intermittent nature. Fluctuations in energy availability from these sources prevent them from becoming viable stand-alone energy options as grid connection or other backup generation methods remain necessary when wind or sun exposure is insufficient Intermittency of energy generation also creates issues in overloading the existing power grid and adds difficulty in forecasting energy needs [9]. Though goals of increasing renewable energy generation are crucial to reduce greenhouse gas emissions, solutions must be developed in tandem to mitigate the instability of these technologies. The implementation of energy storage systems is widely regarded as an effective means to address this issue.

1.2 Energy Storage

1.2.1 Forms of Energy Storage

Energy storage systems are imperative for the progression of intermittent renewable energy technologies such as wind and solar. Energy storage provides a means to save the excess energy generated during favorable conditions for later use and thus stabilizes the energy supply. Many of the main forms of energy storage include pumped hydro, compressed air, flywheel, superconducting magnetic, supercapacitor, hydrogen, thermal, and battery energy storage [10]. Pumped hydro is the most common energy storage form, constituting approximately 99% of all global grid-connected electricity storage; compressed air storage using underground caverns or large tanks is the next highest [10, 11]. However, both of these energy storage methods have specific geological and spatial requirements, limiting where they can be installed. The contributions of other energy storage technologies are expected to increase as more regions invest in energy storage and as their development continues.

All of these options span different stages of development from research to deployment to maturity, and each form offers unique advantages for specific applications [12]. Figure 1 shows a visual comparison between the various energy storage technologies with respect to system power ratings, level of readiness for deployment, and efficiency; the image is an amalgamation of figures in literature [11, 13, 14].

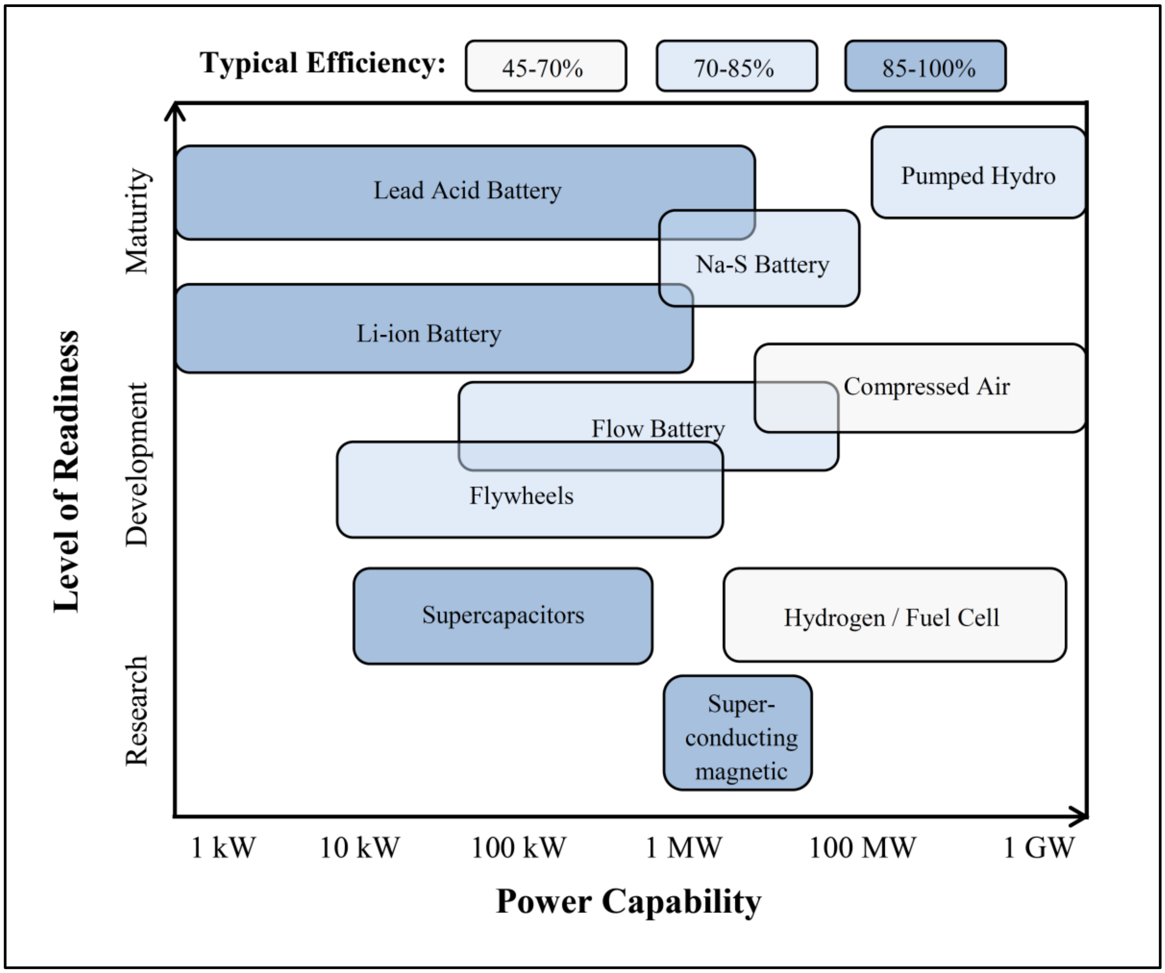

Fig. 1: Energy storage form comparison. The figure is an amalgamation of similar figures to compare the system power ratings, level of readiness for deployment, and efficiency of top energy storage technologies.

As shown, technologies in the battery category have the ability to power a wide range of applications including grid load support. Many types of batteries are sufficiently established that they are either already successfully installed or considered mature enough to be ready for greater deployment [14]. This concept of “readiness” is crucial as studies show that large-scale reductions in greenhouse gas emissions need to occur in the next 10-15 years to prevent severe climate change consequences [15]. For this reason, batteries are a highly attractive solution due to their maturity and low installation time.

The implementation of low-cost yet high-energy battery systems is a top strategy to achieve energy goals.

1.2.2 Batteries

The battery category encompasses many different forms of batteries of various chemical compositions. Batteries can be either primary (non-rechargeable) or secondary (rechargeable), and energy storage applications require the latter to store and deliver energy on demand. Several types of secondary batteries have proven successful over the years: lead acid, nickel-cadmium (Ni-Cd), nickel-metal-hydride (NiMH), sodium-sulfur (NaS), and lithium-ion (Li-ion). Flow batteries are also gaining popularity for large-scale storage applications. Batteries range widely in their compositions and attributes, rendering some more fit for certain applications than others. Table 1 shows a summarized comparison of the main types of battery candidates for energy storage [16-18].

Table 1: Comparison of attributes of main battery types for energy storage.

	Flow	**Lead Acid**	**Ni-Cd**	**NiMH**	**NaS**	**Li-ion**
Anode	Various	Pb	Cd	MH	Na	C
Cathode	Various	PbO_2	NiOOH	NiOOH	S	$Li(MO_2)$
Electrolyte	Various (aq)	H_2SO_4 (aq)	KOH (aq)	KOH (aq)	Solid	Organic
Nominal Voltage (V)	~ 1.5	2.0	1.2	1.2	2.0	4.0
Operating Temp. (^oC)	0 to 50	-40 to 60	-20 to 70	-20 to 65	300 to 350	-20 to 50
Energy Density	Low	Low	Moderate	Moderate	High	High
Mobility	Low	Moderate	Moderate	High	Low	High
Hazardous	Moderate	High	High	Low	Moderate	Low
Efficiency	~ 70-85%	~ 90%	~ 60-70%	~ 70-90%	~ 75-86%	~ 99%
Cost	Moderate	Low	Moderate	Moderate	High	High
Year Developed	~ 1970	~ 1800	~ 1950	~ 1990	~ 1960	~ 1990

Flow batteries have considerable advantages for large-scale energy storage. Because they are stationary and require spacious areas, flow batteries are well served for grid-tied application; however, their high operational maintenance and expensive membranes present challenges [19]. Lead acid batteries are the most mature battery option, and they have reliably served in vehicle and backup electricity applications. Low specific energy and relatively short service lifetime prevent the use of lead acid batteries in many applications, and toxicity is of concern. Ni-Cd batteries are also highly toxic, causing their use to decline despite their high specific energy [18]. NiMH batteries have excellent advantages in safety and performance, and they serve as a popular choice for hybrid electric vehicles. But the low operating voltage of NiMH batteries are unsatisfactory for 100% electric vehicles, and memory effects have proven problematic for some applications [18]. One of the most promising new battery types for grid support is the NaS battery in terms of energy storage capabilities and economic merit [20]. NaS has exceptional advantages in energy density, lifetime, and low maintenance needs, but the high operational temperature can cause safety concerns and prevents its use in mobile applications [10]. Lastly, Li-ion batteries are attractive for a variety of applications due to their light weight, low toxicity, and outstanding energy density. Most Li-ion batteries show favorable results in lifecycle assessments due to their long lifetime and high efficiency, though a lack of commercial-scale recycling will need to be addressed in the coming years [21]. Despite other disadvantages such as potential flammability and cost, Li-ion batteries remain one of the most versatile and high-performing battery options for both stationary and mobile applications.

1.2.3 Batteries for Electric Vehicles

The electricity generation sector is the common target for action to reduce greenhouse gas emissions, but other contributing sectors need to be held accountable also. In the United States, the transportation sector uses approximately 30% of the nation’s total energy, and at least 91% of this energy is derived from fossil fuels [22, 23]. Though solutions such carpool incentives, public transit development, alternative fuel blends, and more efficient vehicle designs are all viable options to reduce emissions, they suffer from short-term perspective. Unstable population growth and uncertain fossil fuel reserves necessitate a more long-term solution that addresses the root issue: the fuel source. Fortunately, recent advances in technology have enabled electric-powered vehicles (EVs) to become a more practical and economically viable option.

Preventing the global consequences of climate change is the goal often cited by electric vehicle proponents. But one of the greatest benefits of electric vehicles is their positive effect on local air quality. Conventional vehicles emit airborne pollutants such as sulfur dioxide, nitrous dioxide, volatile organic compounds, and other harmful particulates in addition to greenhouse gases. These pollutants are known to be linked to increased risks of respiratory illness, heart disease, and cancer and can concentrate at the local level [24]. Electric vehicles are therefore an attractive option to combat air quality issues as they have no emissions for operation. Areas with congested traffic patterns would be able to see appreciable differences in local air quality with electric vehicles substituting conventional fossil fuel vehicles, and billions of dollars in health care cost savings would result [25].

But currently, the high price and limited miles-per-charge of the average EV makes it difficult to compete with conventional vehicles. When predicting the growth of the EV market, most economic analyses show that the greatest influence is the cost of the battery [15]. Though the EV has proven to be competitive in terms of safety, practicality, and performance capabilities, the key development for EV market growth is an overall decrease in battery costs and increase in battery energy density. Battery costs have decreased steadily in recent years: as of 2015, the costs (in USD/kWh) are approximately one third of the costs from 2008 [26]. However, battery costs from 2015 will need to further decrease by half, and battery energy density will need to increase by nearly 45%, to meet 2022 industry goals [26].

Though EVs have zero tailpipe emissions, the total greenhouse gas emissions savings of EVs are dependent on the energy generation methods used to fabricate and charge vehicle batteries [27, 28]. Charging the batteries of electric vehicles requires electricity currently supplied by the electric grid, which continues to use primarily fossil fuels for energy generation. With this in mind, literature remains undecided on whether electric vehicles actually generate more or less indirect emissions in their lifetime than conventional vehicles. Reports show both drastic reductions in emissions [28, 29] and a net increase in emissions [30] depending upon local energy generation methods, charging time of day, and other key variables. Thus batteries contribute to the EV market twofold: battery development increases the functionality and economic viability of the vehicles directly, and it indirectly reduces vehicle lifecycle emissions by bolstering renewable energy generation.

The preferred battery for EVs is the Li-ion battery for two main reasons: it is lightweight and has high energy density. The drivable range of the EV is dependent upon these two requirements, making the Li-ion battery the best candidate for the application [29].

Further development of Li-ion batteries is needed to address several concerns including cost, safety, capacity, and lifetime, yet manufacturers already heavily rely on these batteries due to their current performance capabilities.

1.3 Lithium-ion Batteries

1.3.1 Functionality

Since its initial development in the 1970s and subsequent commercialization in 1991 by Sony Corporation, the Li-ion battery has become widely integrated into modern society [31]. Most electronic devices such as cameras, cellular phones, computers, and other gadgets have a secondary Li-ion battery as a power supply. Other markets such as EVs and energy generation are also using larger stacks or blocks of connected Li-ion batteries in recent years.

Batteries are comprised of three main components: two electrodes (anode and cathode) and an electrolyte. The electrodes store the chemical energy of the battery which can be used as electrical energy for an application. The cell hosts a chemical reduction-oxidation reaction specific to the chemistries of the electrodes: the anode functions as the reductant, and the cathode is the oxidant for the charge reaction. In a standard Li-ion battery, Equation 1 shows the reaction at the cathode during charging of the cell. Equation 2 shows the reaction during discharge. In the equations, the term MO_2 stands for any metal oxide used as the active material of the cathode. A variety of lithium transition metal oxides can be used as the active material such as $LiCoO_2$, $LiMn_2O_4$, and $LiFePO_4$. $LiCoO_2$ was developed by Goodenough and Mizushima. Other layered-structured materials such as $LiNiMnCoO_2$ and $LiNiCoAlO_2$ are also widely used [16].

$$\textit{(charge)}\ \ LiMO_2 \rightarrow Li_{1-x}MO_2 + x\,Li^+ + x\,e^- \tag{1}$$

$$\textit{(discharge)}\ \ Li_{1-x}MO_2 + x\,Li^+ + x\,e^- \rightarrow LiMO_2 \tag{2}$$

Equation 3 shows the reaction at the anode during charging of the cell, and Equation 4 shows the reaction during discharge. The term *A* stands for the active material of the anode, which is commonly replaced with symbols for graphite or for silicon.

$$\textit{(charge)}\ \ A + y\,Li^+ + y\,e^- \rightarrow Li_yA \tag{3}$$

$$\textit{(discharge)}\ \ Li_yA \rightarrow A + y\,Li^+ + y\,e^- \tag{4}$$

The third component, the electrolyte, facilitates the movement of the ionic components for the reaction between the two electrodes. In Li-ion batteries, an ion-permeable separator soaked in the electrolyte solution is also included between the two electrodes to prevent direct electrode contact. The most common electrolyte choice for Li-ion cells is a solution of lithium salt and organic liquid; however, other options include lithium salts in nonorganic liquids, fused lithium salts, and ionically conductive materials such as polymers and ceramics [32]. The electrolyte also contributes to the formation of a stable passivating layer on the surface of each electrode. This layer, the solid-electrolyte-interphase (SEI), is formed during the first charge of the cell as the organic solvent of the electrolyte decomposes on the electrode surface [32]. Initially speculated as a hindrance to the cell, the SEI layer is now understood to function as a protective, electrically insulating layer on the electrode while remaining permeable for ion transport [33].

Li-ion battery functionality is unique because it involves the ‘intercalation’ of Li ions for the cell reaction. When the cell is charging, Li ions shuttle from the cathode, through the permeable separator, and to the anode where they intercalate into the layered material. The phenomenon is reversed during the discharging of the cell. The intercalation of the Li ions occurs quickly and reversibly; the reaction is also attractive because there are no recrystallization or phase changes that occur, only Li-ion insertion and desertion in the active materials [32]. Figure 2 includes a diagram outlining the functionality of a Li-ion cell; the directional movement of the Li^+ ions and electrons is shown in relation to the cell components.

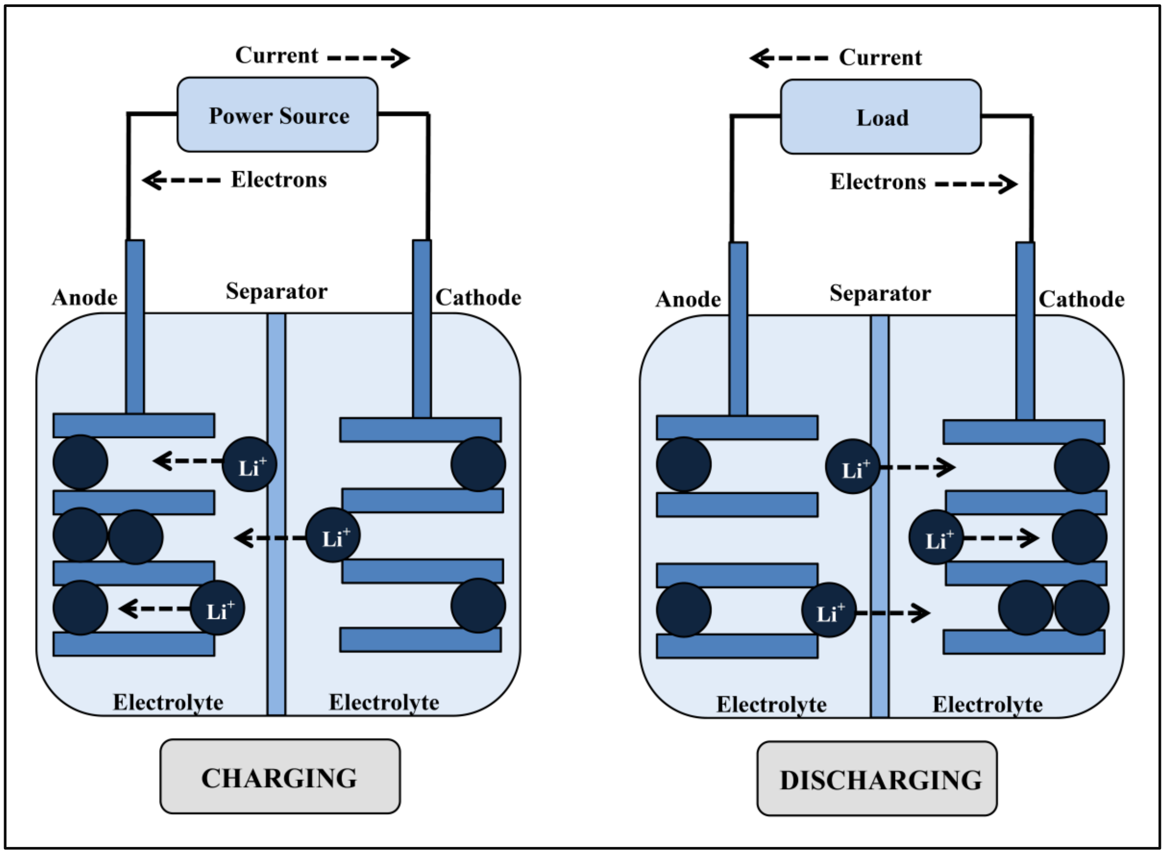
Current
Power Source
Electrons
Anode
Separator
Cathode
Li+
Li+
Li+
Electrolyte
Electrolyte
CHARGING
Current
Load
Electrons
Anode
Separator
Cathode
Li+
Li+
Li+
Electrolyte
Electrolyte
DISCHARGING

Fig. 2: Diagram illustrating the functionality of a Li-ion cell under charge and discharge conditions. The directional movement of the Li ions, electrons, and current is shown.

For a fundamental understanding of the overall cell functionality, the main thermodynamic and kinetic principles that govern the electrochemical reactions are included. Equation 5 is obtained by relating the maximum work of the cell to the change in free energy per one mole of the reaction. The maximum energy that the cell can supply can be calculated from the thermodynamic relationship

$$\Delta G = -n F E_{cell} \tag{5}$$

where ΔG is the Gibbs free energy of the reaction, n is the number of moles transferred in the reaction, F is the Faraday constant, and E_{cell} is the cell potential as calculated from the electrode potentials of each half reaction for the cell. Since a “cell” can also be represented by a half-reaction and a standard hydrogen electrode, the relationship in Equation 5 can be applied using electrode potentials. The resulting equation, the Nernst equation, shows the relationship between the electrode potential of a half reaction, its standard electrode potential, and the activities of the reaction species [34, 35]. The Nernst equation is shown in Equation 6

$$E = E^{\theta} + (R\,T / n\,F)[\,\ln(a_{ox} / a_{red})] \qquad (6)$$

where E is the electrode potential of the half reaction, E^{θ} is the standard electrode potential relative to the standard hydrogen electrode, R is the universal gas constant, T is the temperature, a_{ox} is the activity of the oxidizing species, and a_{red} is the activity of the reducing species. Using basic thermodynamic principles, the electrode kinetics can be derived and yield the Butler-Volmer equation as shown by Equation 7. The net current of the electrode is related to the cathodic and anodic contributions from the reaction as defined by

$$i = i_o\,[\exp(-\alpha_c\,n\,F\,\eta / R\,T) - \exp(\alpha_a\,n\,F\,\eta / R\,T)] \qquad (7)$$

where i is the net current of the anode and cathode, i_o is the exchange current, α_c is the cathodic transfer coefficient, α_a is the anodic transfer coefficient, and η is the overpotential. The overpotential is defined as the difference in potential between the thermodynamically calculated value and the experimental value. The overpotential of the cell can also be related to the basic definition of power as shown in Equations 8 and 9.

With secondary cells, the equations can apply for either charging or discharging conditions of the cell.

$$P = I \times V \tag{8}$$

$$V = V_{oc} + \eta \tag{9}$$

In the equations, P is the charging/discharging power of the cell, I is the charging/discharging current, V is the charging/discharging voltage, and V_{oc} is the open circuit voltage [36]. A number of different variables can affect the overpotential of the cell, including the cell internal resistance. The cell resistance can be calculated with the following summation

$$R_{cell} = R_e + R_{ct} \tag{10}$$

where R_{el} is the resistance across the electrolyte and R_{ct} is the sum of resistances across the electrode and SEI layer. Another important aspect of performance for secondary batteries is the Coulombic efficiency of the cell as shown in Equation 11. This parameter shows the relationship between the charge and discharge capacities of the cell, indicating how much stored charge is recovered for the cycle.

$$Coulombic\ efficiency = (Q_{dis} / Q_{ch}) \times 100\% \tag{11}$$

From the equation, Q_{dis} is the discharge capacity of the cell and Q_{ch} is the charge capacity of the cell. Capacity refers to the amount of charge provided by the cell, and the specific capacity is generally provided in literature in units of mAhg^{-1}. Here, the mass includes only the mass of the active materials, excluding the current collector foil mass.

For manufacturing, these components are packaged in different forms such as coin cell, cylindrical cell, pouch cell, or prismatic cell depending upon the size and power requirements of the battery. Most commercial Li-ion battery electrodes are fabricated using the same process: slurry mixtures of the anode and cathode materials are cast onto copper and aluminum current collector foils, respectively. The slurry mixtures consist of the active material (commonly graphite for the anode and a lithium-metal-oxide for the cathode), a conductive additive (typically carbon), and a binding agent (for adherence to the foil) dissolved in a solvent. From the coated foils, electrodes are cut to fit the size of the designated battery. As lithium is highly reactive when exposed to water even in atmospheric concentrations, Li-ion batteries are assembled under anhydrous conditions and with non-aqueous electrolytes. The coin cell configuration is small and involves a simple assembly process, making it a popular choice in research applications. Two additional components, spacers and springs, are used in coin cell assembly to ensure even contact for the anode-separator-cathode stack. Figure 3 illustrates the basic structure of a Li-ion battery in a CR2032-type coin cell configuration with its labeled components as modified from a diagram by MTI Corporation [37].

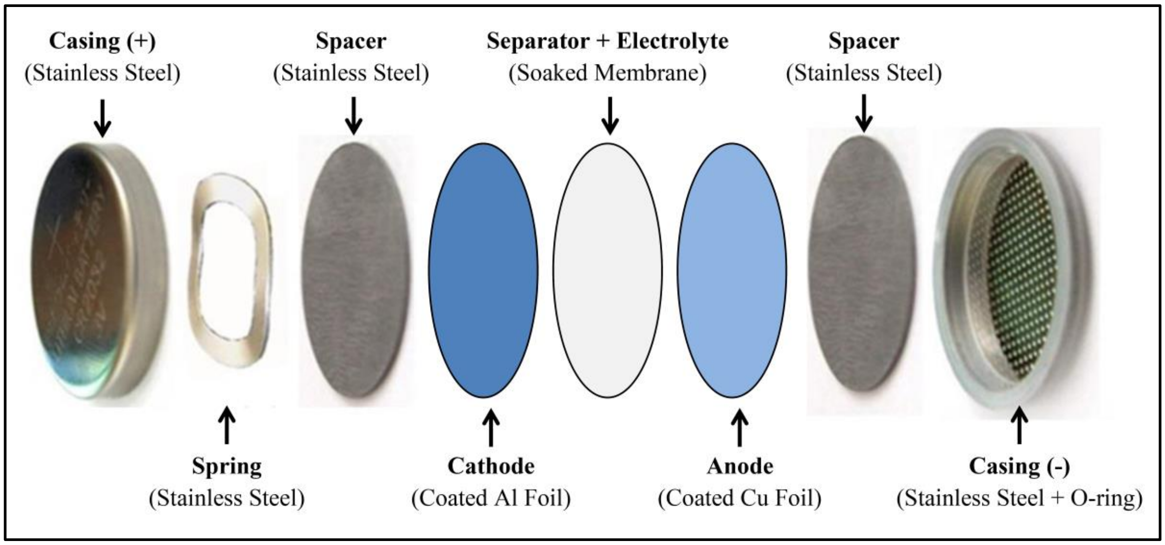
Casing (+)
(Stainless Steel)
Spacer
(Stainless Steel)
Separator + Electrolyte
(Soaked Membrane)
Spacer
(Stainless Steel)
Spring
(Stainless Steel)
Cathode
(Coated Al Foil)
Anode
(Coated Cu Foil)
Casing (-)
(Stainless Steel + O-ring)

Fig. 3: Basic structure of a CR2032-type coin cell with labeled components. Cathode, anode, and separator can vary in composition and appearance.

Once assembled, coin cells can be tested using charge and discharge cycling equipment to determine important performance characteristics of the cell such as cycle completion time, charge and discharge capacities, and efficiency.

1.3.2 Research

There are three major markets that depend on the improvement of batteries, particularly the Li-ion battery: (1) portable devices, (2) electric vehicles, and (3) energy generation. Though new forms of batteries show great promise for energy storage applications, industry will continue to invest in Li-ion batteries for the near future due to their advantageous properties as previously described [38]. However, the improvement of the Li-ion battery remains an important topic in research. Further improvements in Li-ion batteries can enable the advancement of important new technologies in each of the aforementioned fields, particularly electric vehicles and renewable energy methods [31, 39].

Specifically, the development of high capacity yet low-cost electrode materials remains a high priority for researchers to fulfill greater energy storage needs [31, 40]. There is also significant pressure for new electrode material research to be conscientious of environmental effects and to exhibit sustainable processing techniques [41]. With these qualifications in mind, there are a limited number of compounds that can be practically utilized. Research into the viability of new cathode materials is extremely active, but special attention to anode development using silicon has become prominent in literature.

1.4 Silicon-Based Anodes

1.4.1 Silicon Anodes

The majority of commercial Li-ion battery manufacturers use graphite (C) as the anode material. Graphite has many desirable characteristics, and its ability to facilitate the intercalation of Li ions allows the material to have low volume expansion (< 7%) when lithiated and delithiated [42]. Low volume expansion helps to preserve the integrity of the electrode and preserve the SEI layer. However, graphite suffers from low theoretical capacity (~ 372 $mAhg^{-1}$), and this proves problematic for meeting increasing energy demands [43].

One of the most expansively studied anode materials is silicon, and it continues to be a compelling choice due to its high theoretical capacity (~ 4200 $mAhg^{-1}$) and proven functionality [43, 44]. Silicon also shines as a sustainable material option due to its general natural abundance and non-toxicity [43, 45, 46]. However, several unfavorable characteristics of silicon prevent the material from becoming more prominently utilized. The characteristic that provides silicon with such high capacity also causes one of its greatest flaws. Unlike graphite, silicon participates in an alloying reaction with lithium rather than intercalation. This allows silicon to accommodate an uncommonly large stoichiometric ratio of lithium, but it also results in high volume expansion of the material (> 300%) [42]. The expansion stresses the structure of the material, leading to internal cracking and destruction of the SEI layer. Literature indicates that using nano-sized silicon particles and structures can enhance the stress resiliency of the anode, but decomposition eventually prevails over long-term cycling [47]. The large volume changes upon lithiation/delithiation of the anode and overall poor capacity retention have hindered the commercial viability of predominantly silicon based anodes [45, 48, 49]. Some commercial manufacturers, such as Panasonic, have begun incorporating a percentage of silicon in their graphite anode to improve capacity [50]. Partial substitution of graphite can help boost performance, but the ultimate goal of full replacement is still widely sought-after.

Another prominent issue that plagues the silicon anode is the low electrical conductivity of silicon (resistivity of 2.3×10^3 Ωm, 20ºC). Though silicon has high theoretical capacity, poor electrical conductivity limits the actual capacity to substantially lower values [51]. Initial electrical conductivity is also further worsened with the lithiation expansion of the material over cycling [47, 52]. Because the advancement of practical silicon anodes depends upon overcoming these limitations, much of silicon anode research involves slight modification of either the anode surface or the silicon structure. To increase the cycling stability and the electrical conductivity of silicon anodes, numerous techniques involving additive materials have been tested throughout literature as described in the following section.

1.4.2 Carbon Additives

The most common approach to mitigate issues of stability and conductivity is to supplement silicon with a form of carbon. Conductive carbon is commonly used in industry as a conductive additive for both anode and cathode slurry mixtures. However, conductive carbon black does not contribute to the capacity of the anode, so adding carbon black is typically restrained to small weight percentages [53]. Many new efforts in improving silicon anodes have focused on the minimization or total elimination of carbon black in the anode material to maximize capacity. For example, a study conducted by Zhang *et al.* used reduced graphene oxide as a conductive additive to a standard silicon slurry [53]. Carbon black content was reduced by over 50% and supplemented by one weight percent of the graphene additive; results showed improved capacity retention for cells with the additive over those with only carbon black. Multiple studies also utilize strategies involving graphene, showing higher capacities and improved conductive networking throughout the material with varying degrees of success

[54, 55]. Though impressive, these strategies are currently limited by the complex and expensive processes needed to produce graphene at a large scale.

Many studies have utilized creative means to form silicon/carbon structures including carbon coated silicon [56-58] and silicon/carbon embedded frameworks [59]. One study by Liu *et al.* showed that carbon-coated silicon particle anodes reach capacities as high at 1000 $mAhg^{-1}$ and are sustained for over 50 cycles at a cycling rate of 300 mAg^{-1} [58]. Variations of silicon/carbon composites are also prevalent in literature with successful results [60-62]. These composites have shown immense promise for accommodating the expansion of silicon upon lithiation and improving conductivity [63]. Some composites were formed using relatively facile methods such as ball milling, but the majority involved more complex energy-intensive processes [63]. Silicon/carbon materials are successful on their own, and they are often also used as a foundational material to which other components, such as transition metals, can be added.

1.4.3 Transition Metal Additives

Though silicon/carbon integration methods have proven successful in demonstrating increased capacity, positive results have also been achieved with the addition of metallic components. The addition of different transition metals such as silver, tin, and germanium has been shown to enhance the performance of silicon-based anodes [64-66]. One such study by Zhong *et al.* demonstrated how tin nanoparticles function as a successful conductive additive [65]. Tin nanoparticles were introduced to a silicon-based slurry via small weight percentages of tin dichloride, and results showed improved capacities of over 1100 mAhg^{-1} when cycled at 280 mAg^{-1} and over 50% reduction in the resistivity of the anodes. Tin has shown to be a popular material in anode literature due to its good conductivity (resistivity of 1.09×10^{-7} Ωm, 20ºC), lithiation capacity, and general nontoxicity [67, 68].

There is extensive research investigating silicon/metal composite materials [63]. Many of these reports showed that increased capacities of over 1000 mAhg^{-1} can be achieved using a variety of methods to combine silicon and transition metals [63]. Metal frameworks, such as the nickel scaffold described in Zhang *et al.*, have also shown success in accommodating the expansion of silicon and increasing conductivity of the anode [69]. But research in metal additives must be conscientious of the abundance and cost of materials in addition to the fabrication processes. Positive results have also been shown from using copper in a variety of strategies with silicon anodes.

1.4.4 Copper Additives

The benefits of using copper additives in silicon-based anodes are well documented. Copper is well-known for having one of the highest electrical conductivities (resistivity of 1.68×10^{-8} Ωm, 20ºC), and it has been studied in forms such as arrays [70, 71], coatings [72, 73], and depositions [74, 75] with silicon. Copper coatings have been fabricated by coating the silicon anode surface with a thin layer of copper [72] and by coating the individual silicon particles in copper [73]; both methods demonstrated significant enhancement of the capacity and stability in comparison to silicon control anodes. Joyce *et al.* investigated the prospect of using a copper coating to function as both the conductive additive and the binding agent for a silicon anode, and the cycling results proved comparable for approximately 40 cycles [76].

Silicon/copper composites have also been synthesized and yield promising results in improving performance [77-80]. In the study by Cheng *et al.,* silicon/carbon/copper composite materials were formed using varying amounts of copper acetate combined with silicon [77]. The report showed how a 2.2 weight percent addition of copper in the anode material yielded an improved capacity (990 $mAhg^{-1}$) and conductivity. This report exhibited that even small weight percentages of additive can effect considerable change, and this has become an important theme in many projects. In several reports, the compound Cu_3Si was observed to form following the heat treatment step, and it was shown to be an effective contributor to improved stability as it can have a buffering effect to combat the silicon volume expansion [75, 77, 81-84]. Reports also indicate that, in addition to limiting the degradation effects caused by volume expansion, the addition of Cu_3Si increases the overall conductivity of the material [85, 86]. The high electrical conductivity of Cu_3Si facilitates improved electronic connection between particles in the anode material and thus contributes to the improved performance of silicon-based anode materials [81, 87].

Cu_3Si has been explored as a viable material for a variety of applications, especially for battery and solar cell technologies; knowledge of the material properties of the material has also progressed considerably from research. The silicon-copper phase diagram indicating the properties of the material in relation to temperature is shown in Fig. 4, and the three regions for the η, η’, and η” Cu_3Si phases are illustrated.

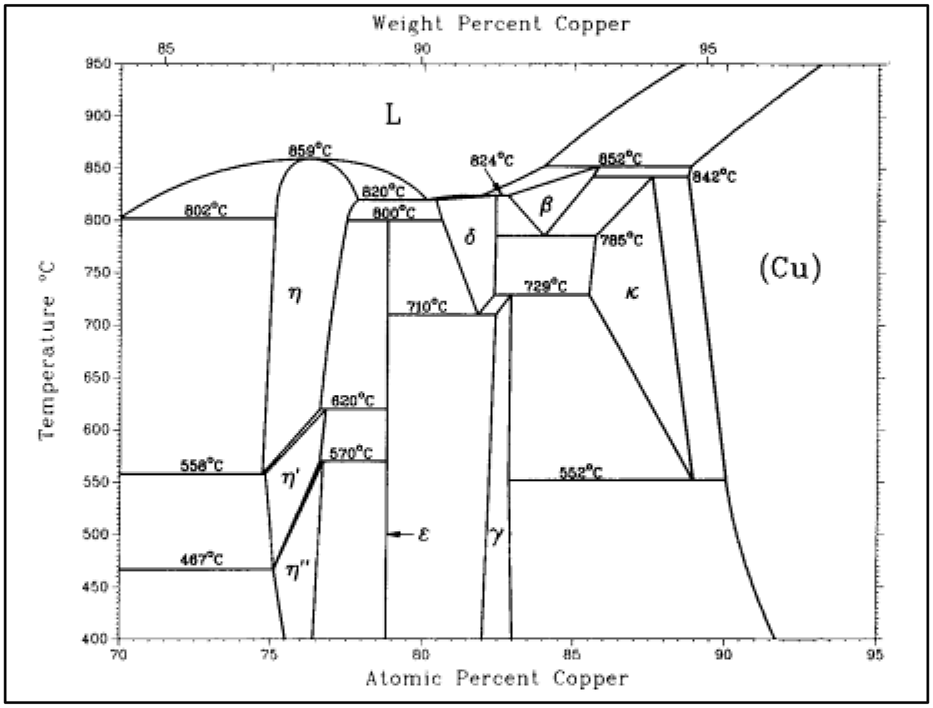

Fig. 4: The equilibrium phase diagram for the Si-Cu system is shown in the range of 65 to 90 atomic percent copper content. The enlargement illustrates the regions for the η, η’, and η” Cu_3Si phases [88].

The Cu_3Si η phase corresponds to very high temperature (above 558ºC) heat treatment process as utilized in several examples of anode fabrication in literature; the Cu_3Si η” phase is shown to be stable below 467ºC and thus at room temperature. In the structural analysis of Cu_3Si published by Solberg, the formation of Cu_3Si particles via the heating and subsequent cooling of dislocation-free silicon and copper additive is described [89]. Though η phase particles may have been grown using high temperatures, their probable phase transformation to the lower-temperature η” phase is assumed and well supported in literature [90]. In silicon anode research using copper additives, reports often indicate the presence of both copper particles and Cu_3Si. Though the copper may be integrated into the silicon based structure of the anode at the time of anode fabrication, copper can be expected to either relocate or precipitate as Cu_3Si over time because copper has poor solubility in silicon at room temperature [91, 92]. Eventually, copper can manifest at defect sites, grain boundaries, or the surface of the sample, or it can form the stable Cu_3Si phase.

In a study conducted by Kim *et al.*, the effects of copper additive into silicon-carbon anode material were investigated [87]. Copper was deposited on silicon particles, and the subsequent material was mixed and heated to 900ºC for two hours. Results confirmed the formation of Cu_3Si, and the composite material was shown to have Cu_3Si adhered to Cu and Si particles in a homogeneous distribution. A report by Yoon *et al*. also demonstrated this configuration by showing the adherence of Cu_3Si layers on silicon core particles with metallic Cu particles randomly dispersed throughout [83]. The report also showed the continued adherence of the Cu_3Si after electrochemical testing, demonstrating that the material was stable during charge/discharge cycling. This adherence is important as previous studies have shown that the detachment of additive materials (such as copper) from the silicon particles results in poor long-term cycling [93]. Though Cu_3Si has shown to improve the conductivity and stability of silicon-based anodes, studies have also shown that Cu_3Si is electrochemically inactive during the lithiation and delithiation processes of cycle testing [82, 83, 87].

Also from the study conducted by Kim *et al.*, specifically $CuCl_2$ was used as a precursor material in the silicon-based mixture to form the Si-Cu_3Si-Cu composite material, and the $CuCl_2$ to Si ratio was high at 2.683:1 [87]. An initial discharge capacity of 680 $mAhg^{-1}$ was attained for the this material during cycle testing at a low constant current of 50 $mAhg^{-1}$ [87]. The report asserts that most copper reacted with silicon to form Cu_3Si due to the very high diffusivity of copper in solid state reactions [87, 94]. Due to its proven benefits in providing stability to the anode material and its ease of formation, the addition of Cu_3Si is relatively common in literature and remains an important, popular topic.

Copper has also been studied as a nanoparticle additive for anode materials [78, 95, 96], and it is advantageous that the small particle size allows for thorough integration into the silicon anode structure. The work conducted by Fang *et al.* demonstrated a one-step process of directly adding copper nanoparticles to a standard silicon slurry [78]. The nanoparticles showed excellent dispersion in the silicon structure, and the cycling performance of cells with added copper were improved over a purely silicon-based control. However, the anodes suffered from poor capacity retentions of under 45% for all samples with the copper additive during cycle testing [78]. Though reports have achieved different levels of success in maintaining high capacity during cycling, all have shown that copper additives substantially improve performance when compared to control samples.

Though successful in increasing anode capacity and cycling stability, many of these studies involved varying degrees of complexity that would be difficult to accommodate at the industry scale. Most studies also included numerous process steps that add time and cost. Though copper proves to be an advantageous conductive additive, further research is needed to find a more commercially-compatible methodology for its utilization. The Li-ion battery market already struggles in cost-competitiveness, making simplistic and economic solutions all the more necessary.

1.4.5 Current State of Research

Few energy storage options can compete with Li-ion batteries for applications that require portability, high energy density, and longer-lasting discharge duration. However, improvements in cost and in performance capabilities remain necessary for Li-ion batteries to satisfy the increasing energy requirements of new technologies. Silicon-based materials are a highly desirable replacement for conventional graphite-based materials for anodes in Li-ion batteries due to silicon’s more favorable electrochemical properties. Although numerous strategies to help address the functional issues that hinder silicon-based anodes have been explored throughout the past decade, strategies thus far commonly involve complex or cost-intensive processes.

The motivation for this study derives from the concept of using a copper component to lessen the undesirable functional attributes of silicon as an anode. Though previously mentioned strategies have shown progress in this goal, the focus of this study was to utilize a more straightforward and economic method for the anode fabrication process. As Li-ion battery fabrication facilities swell in production size, simplicity and cost effectiveness of potential solutions are of significant interest and have a greater likelihood for success in industry [97]. *This study investigated the one-step addition of copper nanoparticles via* $CuCl_2$ *to a silicon-based anode mixture using benchtop-scale versions of industrywide techniques for electrode fabrication*. An experimental batch of anodes made with $CuCl_2$ as a substitute for conductive carbon was also assessed to determine the viability of using exclusively silicon with $CuCl_2$ as the active material. Chapter 2 of this report details the experimental process and equipment used to fabricate, characterize, and electrochemically test the anode materials. The chapter also includes the preliminary approaches that were tested in order to optimize the final fabrication process. Chapter 3 presents and discusses the results obtained from this study. Chapters 4 and 5 summarize the main conclusions and recommendations for future research, respectively, elucidated from the results of this study.

Chapter 2: Experimental

2.1 Sample Preparation

This section details all procedures and equipment used in fabricating the experimental silicon-based anodes. Though the fundamental method remained unchanged throughout the study as a whole, several processes evolved over time with the adoption of new techniques and materials. This project involved three main experimental procedures (low-temperature, initial high-temperature, and final high-temperature) that are outlined in the following sub-sections.

2.1.1 Low-Temperature Anodes

The initial slurry mixtures for silicon-based anodes with copper additive were fabricated with a procedure modified from the general preparation techniques and slurry composition reported by Cetinkaya *et al.* [98]. The following chemicals were procured: silicon nanopowder (Si, <100 nm, 98% purity, Sigma-Aldrich), polyvinylidene fluoride (PVDF, MTI), carbon black Super P (CB, 99% purity, Alfa Aesar), and copper dichloride ($CuCl_2$, Sigma-Aldrich). The $CuCl_2$ crystals were milled into a fine powder using a small mortar and pestle for several minutes. Table 2 compiles this information and shows the amounts of material used in the slurry mixtures.

Table 2: Materials and quantities for low-temperature anode study.

Material	Abbreviation	Details	Manufacturer	Amount
Silicon	Si	<100 nm powder 98% purity	Sigma-Aldrich	375 mg
Polyvinylidene fluoride	PVDF	powder	MTI	75 mg
Carbon black (Super P)	CB	powder 99% purity	Alfa Aesar	50 mg
Copper dichloride (dihydrate)	$CuCl_2 \cdot 2H_2O$	crystals 99+%	Sigma-Aldrich	10 mg

The materials were dry mixed and then dissolved in n-methyl-2-pyrrolidone (NMP, MTI) to form a homogeneous slurry using a magnetic stirrer at room temperature for one hour. The control batch consisted of all ingredients except $CuCl_2$, and this batch was denoted as “Si-only” for results. The second batch included the $CuCl_2$ and was denoted as “Si-Cu” for results. An additional test was conducted to determine if further reducing the particle size of the dry material would result in a more homogeneous slurry and improve anode performance. For this test, the dry materials were milled in a planetary ball mill (MTI) as shown in Fig. 5 for 30 minutes prior to mixing with NMP. Alumina milling jars and media were used for this step.

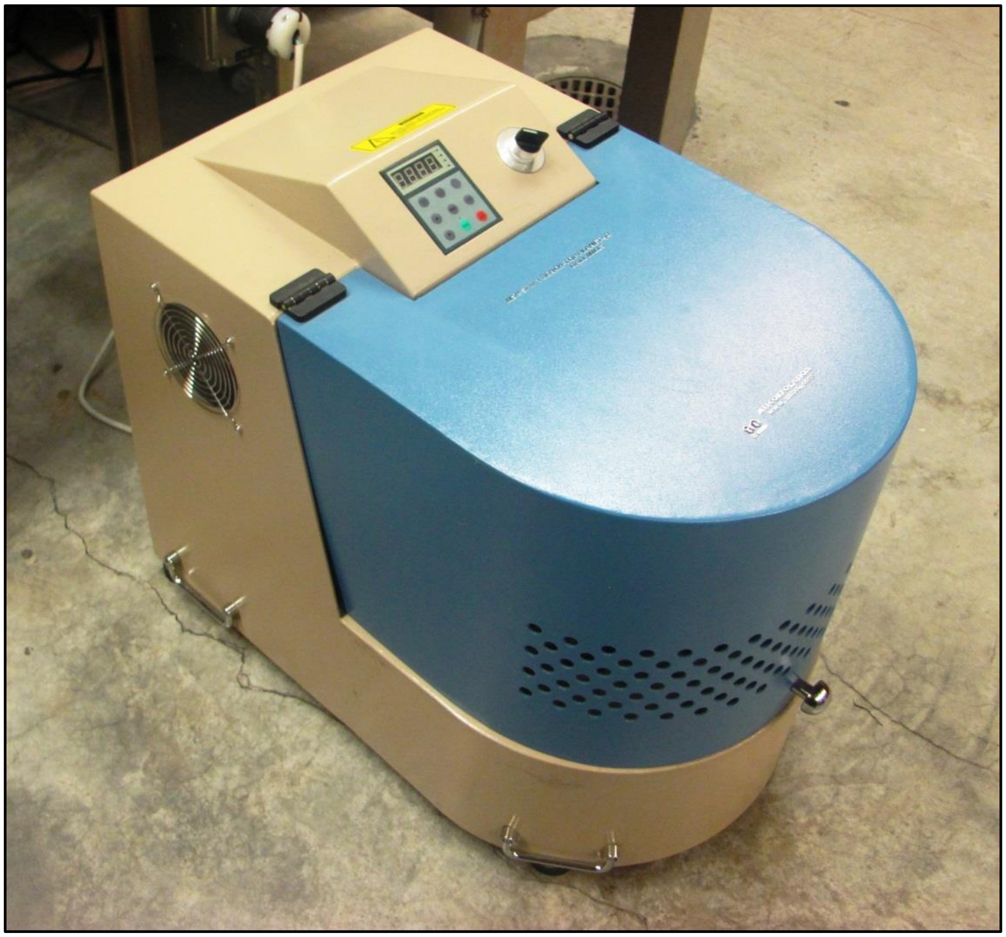

Fig. 5: MTI Planetary ball mill used to reduce the particle size of dry material. The ball mill was operated for 30 minutes.

After mixing, slurries were cast onto a strip of copper current collector foil. Foils were adhered to a clean, glass surface using ethanol and were wiped clean. Each slurry was then cast onto separate foil strips using a Mayer rod. A good casting was characterized by smooth, even application of material free from large grains or bubbles. Figure 6 shows a sample casting. Coated foils were then allowed two hours to air dry before heat treatment in the vacuum oven at 120 ºC for 12 hours. The vacuum oven (MTI) is shown in Fig. 7.

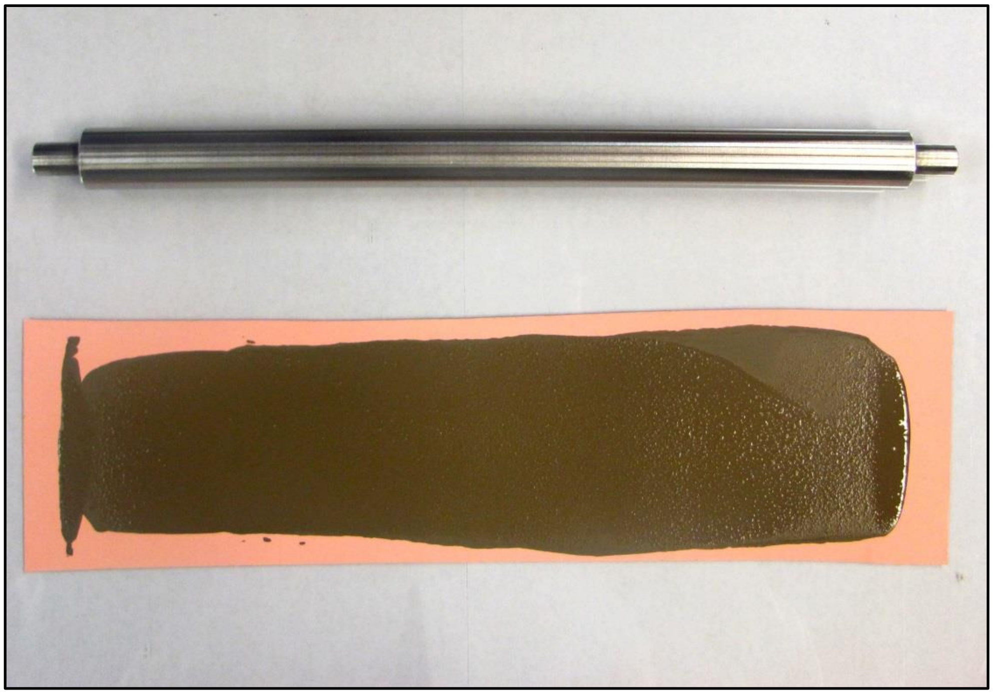

Fig. 6: Image of a typical slurry cast using a Mayer rod onto a copper current collector foil. Application of the slurry should be smooth and without large grains or bubbles. This method was used throughout all studies.

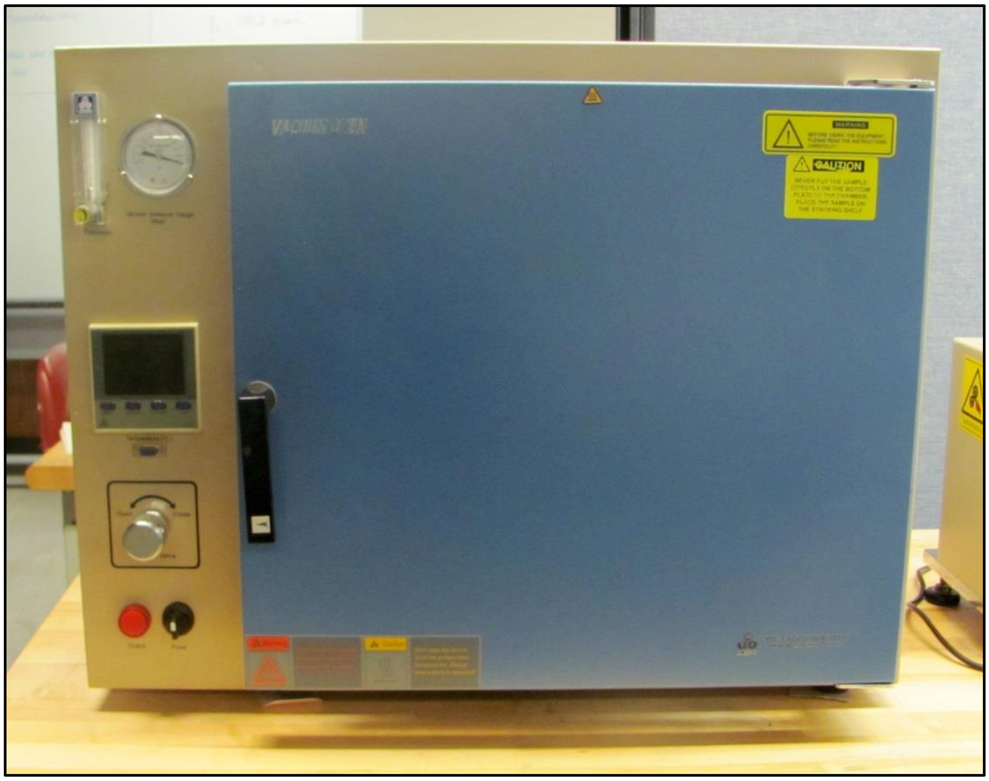

Fig. 7: MTI vacuum oven used for low temperature heat treatment of the coated foils. Foils were heated at 120ºC for 12 hours.

Then, anode discs of 1.3 cm diameter were punched from the foils using a handheld disc punch. A typical anode was measured to have approximately 0.08 mm thickness (foil included) and 0.3 mg cm^{-2} material loading (foil not included). Anode discs were then used to fabricate coin cells as detailed in Section 2.1.3.

2.1.2 Initial High-Temperature Anodes

After examining the results from testing the low-temperature anodes (results described in Chapter 3), further review of the literature was conducted to find alternative anode fabrication methods. Many literature studies included a higher temperature heat treatment step in their processes, and this note prompted the next study of high-temperature anodes for this project. The preparation techniques and slurry composition were adapted from those used by Zhong *et al.* [65]. Materials remained consistent from the previous study except the following alterations: the previous PVDF binder and solvent materials were substituted with polyvinylpyrrolidone (PVP, Sigma-Aldrich) and ethanol, respectively. Table 3 shows the adjusted materials list used for this study.

Table 3: Materials and quantities for initial high-temperature anode study.

Material	Abbreviation	Details	Manufacturer	Amount
Silicon	Si	<100 nm powder 98% purity	Sigma-Aldrich	200 mg
Polyvinylpyrrolidone	PVP	powder	Sigma-Aldrich	720 mg
Carbon black (Super P)	CB	powder 99% purity	Alfa Aesar	20 mg
Copper dichloride (dihydrate)	$CuCl_2 \cdot 2H_2O$	crystals 99+%	Sigma-Aldrich	20 mg

Materials were dry mixed and dissolved in ethanol to form a homogeneous slurry using a magnetic stirrer at room temperature for one hour. The methods of the two separate batches and denotations from the previous study were repeated. Following mixing, slurries were cast onto copper foil using the previous method. The films were allowed two hours to air-dry; foil coatings with ethanol-based slurries were subject to curling over during the drying process as shown in Fig. 8. To combat this, weights such as glass slides were placed on opposite ends of the foil. After drying, the coated foils were annealed under argon at 700 °C for 15 minutes in the tube furnace (MTI) shown in Fig. 9.

To maintain the flatness of the foils while in the tube furnace, a simple graphite stage was made and used throughout the following experiments.

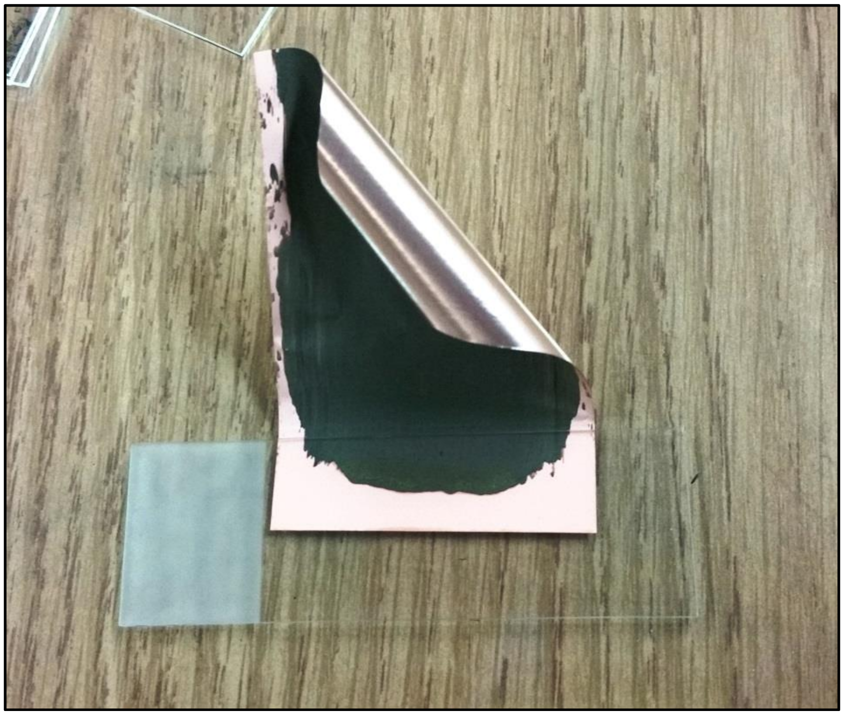

Fig. 8: Image of coated foil curling over and held in place with a glass slide. Ethanol-based slurries exhibited curling during the drying process.

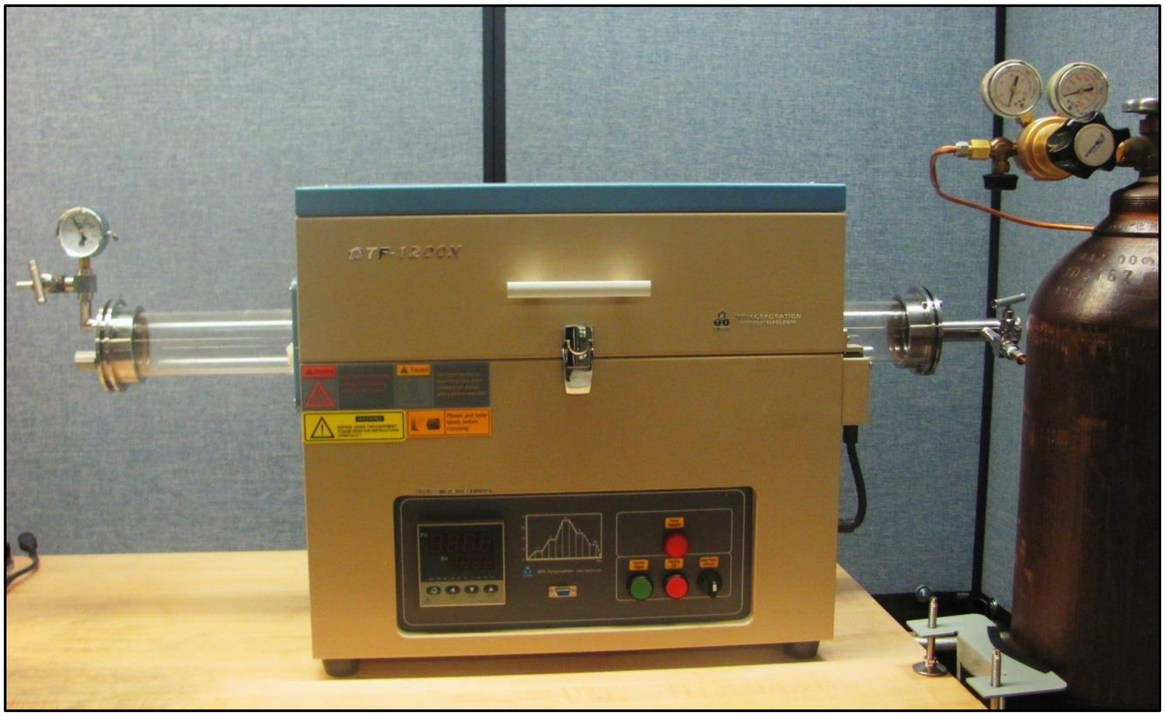

Fig. 9: MTI tube furnace used for high temperature heat treatment of the coated foils. Foils were annealed under argon for 700°C for 15 minutes. A graphite stage was made to keep the foils flat while inside the tube.

Anode discs of 1.3 cm diameter were punched from the foils and were measured to have approximately 0.07 mm thickness (foil included) and 0.4 mg cm^{-2} material loading (foil not included). Anodes were used to assemble coin cells and were characterized using the methods detailed in Section 2.1.3.

2.1.3 Final High-Temperature Anodes

To achieve improved integration of the copper additive and overall homogeneity of the slurry mixture, $CuCl_2$ with smaller particle sizing became a necessity. Copper dichloride anhydrous powder (99.995% purity, Beantown Chemical) was purchased and used throughout the remainder of experimentation. Figure 10 illustrates the visual differences between the two $CuCl_2$ materials. Table 4 includes the adjusted materials list for the final high-temperature anode study.

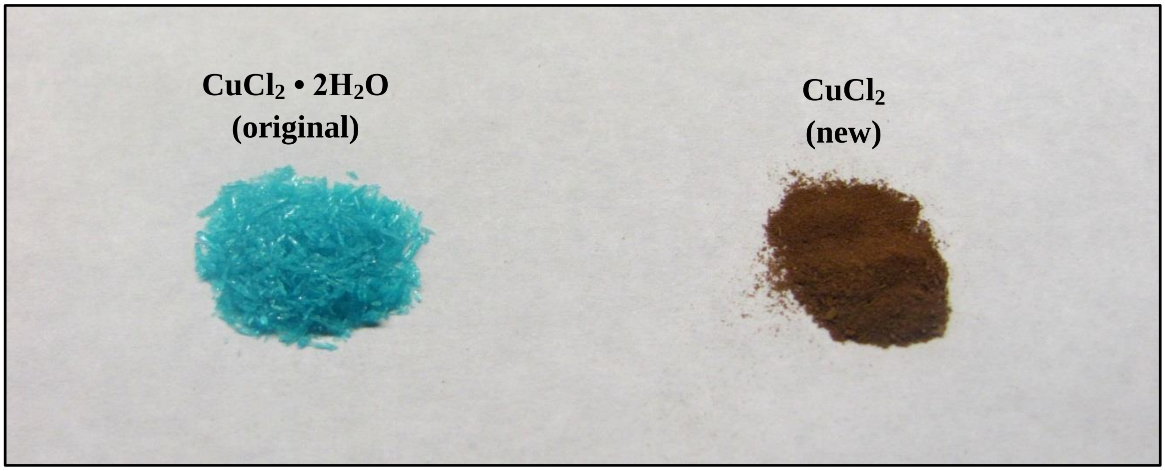

Fig. 10: Image showing the two $CuCl_2$ materials. The smaller grains of the $CuCl_2$ on the right did not require an additional milling step and mixed more homogeneously in the slurry.

Table 4: Materials and quantities for final high-temperature anode study.

Material	Abbreviation	Details	Manufacturer	Amount
Silicon	Si	<100 nm powder 98% purity	Sigma-Aldrich	200 mg
Polyvinylpyrrolidone	PVP	powder	Sigma-Aldrich	720 mg
Carbon black (Super P)	CB	powder 99% purity	Alfa Aesar	20 mg
Copper dichloride anhydrous	$CuCl_2$	powder 99.995% purity	Beantown Chemical	20 mg

Methods from the previous high-temperature study were replicated. The control batch followed this procedure with the omission of the $CuCl_2$ and was denoted as “Si only”. The procedure was replicated for a second batch with the addition of 20 mg copper dichloride, denoted as “Si-Cu”. A third batch was then made without CB and with 20 mg copper dichloride, denoted as “Si-Cu (NC)” where “NC” corresponds to “no conductive carbon”. This third batch was added to determine whether $CuCl_2$ would be a sufficient conductive additive to replace CB altogether. Following heat treatment, anode discs were punched from the foils in the same fashion.

For certain characterization methods, interference from the copper current collector foil prevented the accurate analysis of the copper content in the annealed materials. For this reason, a thin layer of each of the three sample slurries was also spread onto tantalum foil coupons. The coated coupons were allowed to air-dry for two hours, and then they were placed in the tube furnace to anneal under argon at 700°C for 15 minutes. Once cooled, the annealed coatings were removed from the tantalum platforms for characterization.

For electrochemical testing, the punched anode discs were used to fabricate CR2032-type coin cells. Cell separators were made from Celgard tri-layer PP/PE/PP membrane with 25 μm thickness (MTI), and separator discs were prepared using the disc punch shown in Fig. 11. Both anode and separator discs were then transferred to an argon-filled glove box for coin cell assembly. The glove box was maintained with water and oxygen at less than 1.0 ppm, and an image of the box is shown in Fig. 12. CR20232 coin cell casings, springs, and spacers for this study were procured from MTI.

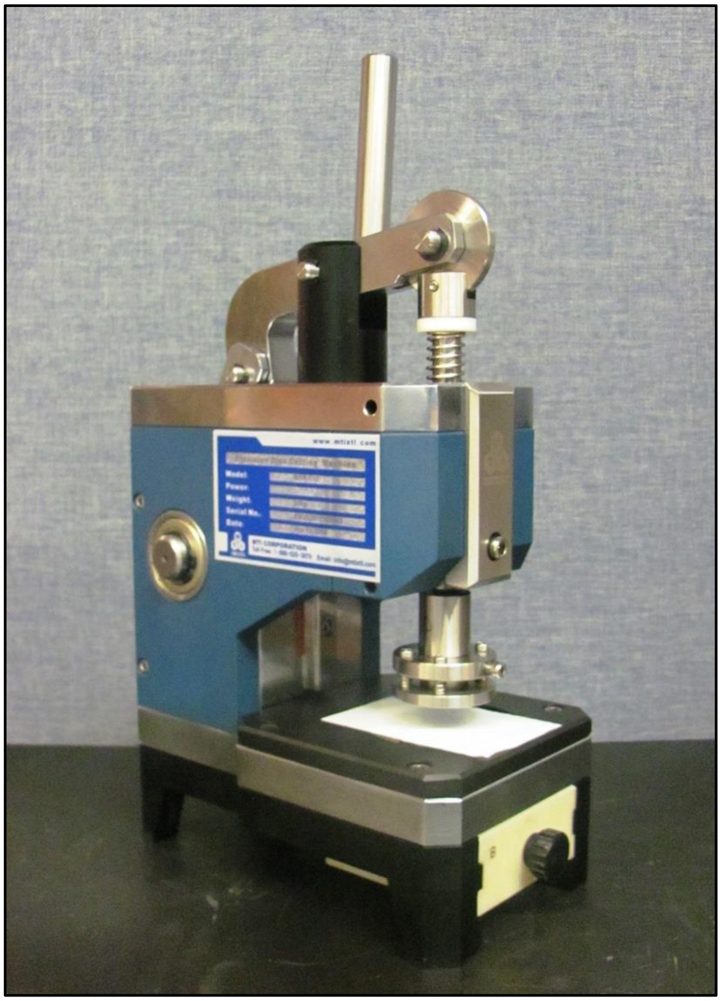

Fig. 11: MTI disc punch for preparing separator discs from sheets of Celgard tri-layer PP/PE/PP membrane. Discs of 18 mm diameter were used.

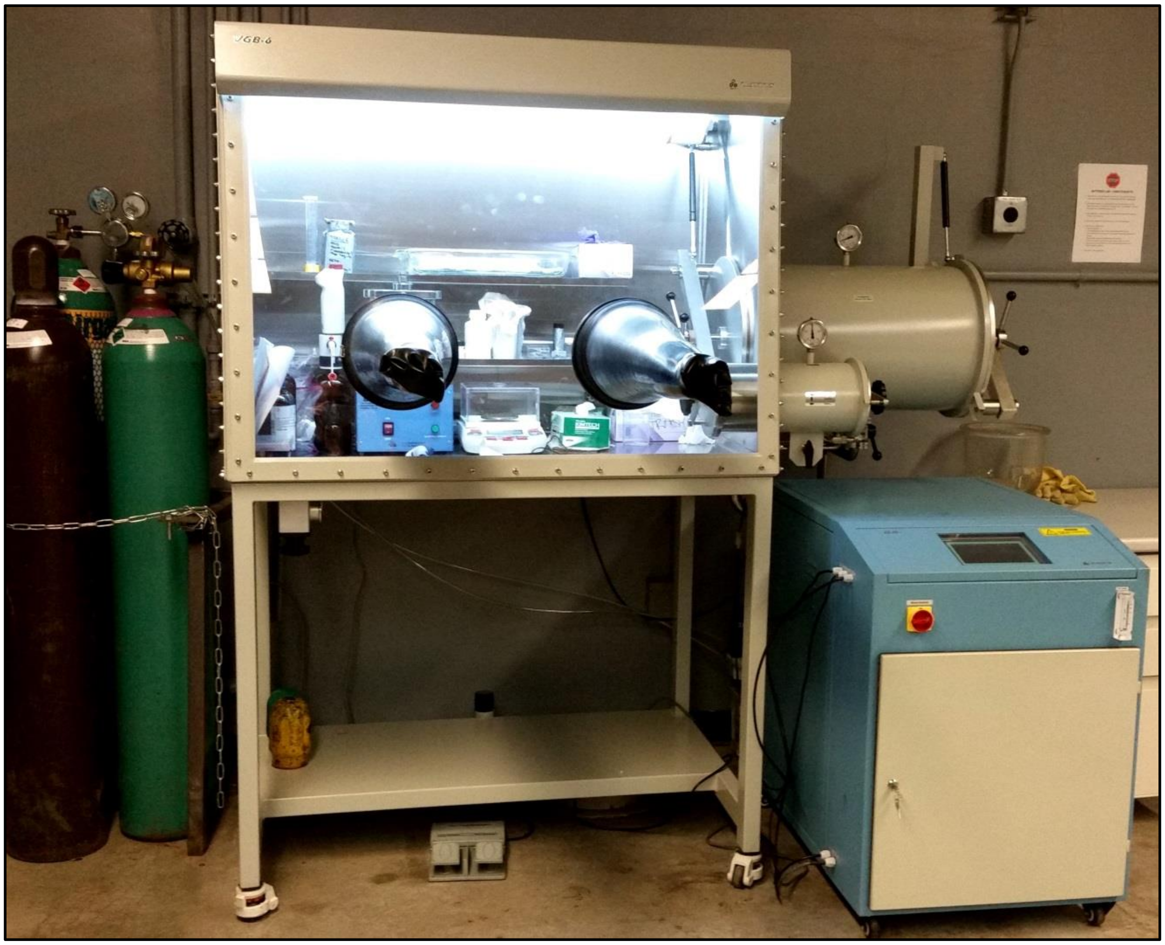

Fig. 12: Glove box used for coin cell assembly. Glove box conditions were maintained with water and oxygen content less than 1.0 ppm.

Inside the glove box, 1.3 cm diameter discs of lithium foil (Alfa Aesar) were punched to function as the cell counter and reference electrode. The electrolyte was a solution of 1.0M lithium hexafluorophosphate ($LiPF_6$) in ethylene carbonate (EC) and diethyl carbonate (DEC) with a 1:1 volume ratio (Sigma-Aldrich). Prior to coin cell assembly, separators were soaked in electrolyte solution for approximately 20 minutes. Coin cells were assembled in the order shown in Fig. 3 from Chapter 1. Once assembled, coin cells were sealed with an electric crimper (MTI) as shown in Fig. 13, cleaned of excess electrolyte, and labeled for testing.

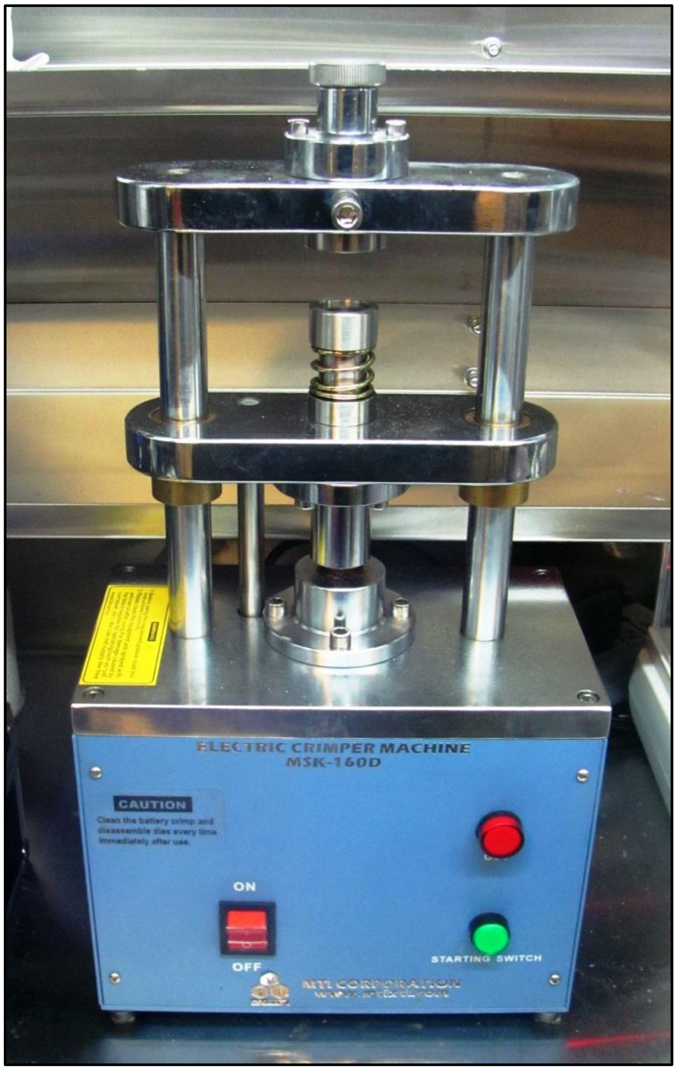
ELECTRIC CRIMPER MACHINE
MSK-160D
CAUTION
Clean the battery crimp and disassemble dies every time immediately after use.
ON
OFF
STARTING SWITCH
MTI CORPORATION

Fig. 13: MTI electric crimper housed inside the glove box. Following assembly by hand, coin cells were crimped to seal contents.

Coin cells were removed from the glove box and electrochemically tested. Following testing, successful coin cells were returned into the glove box for disassembly in order to qualitatively assess the effects of testing on the anode surfaces. The electric crimper was fitted with its de-crimping components to open the coin cells, and the anodes were gently extracted. Figure 14 shows a disassembled coin cell with labeled components aligned in assembly order.

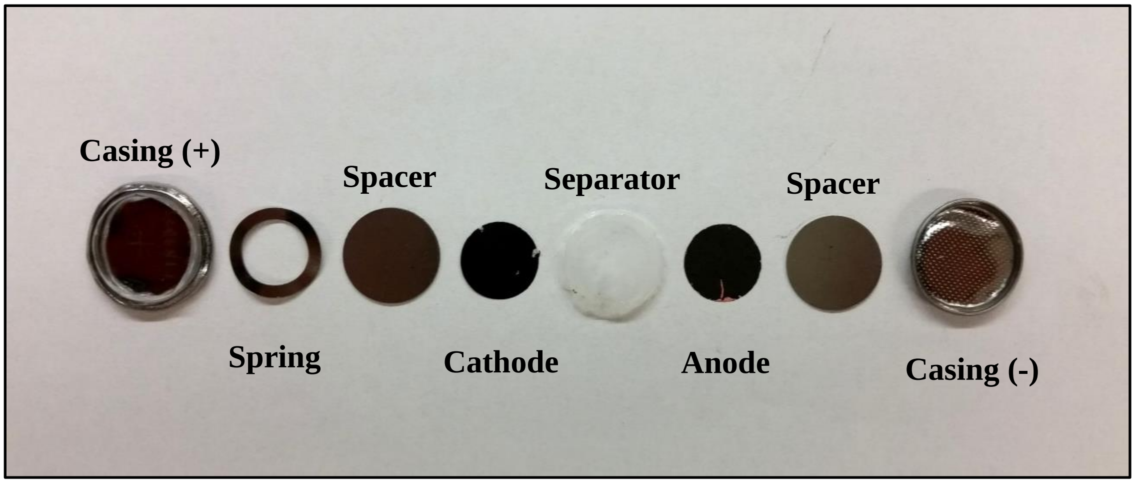

Fig. 14: De-crimped coin cell after electrochemical testing with labeled components in assembly order.

Anodes were washed in EC/DEC solvent to remove excess electrolyte from the coated surfaces per the post-mortem analysis protocol described in Waldmann *et al.* [99]. Care was taken not to scrape the delicate active material from the disc during the procedure. Washed anodes were allowed at least one week to dry undisturbed in the glove box before characterization. During transportation to the characterization equipment, the anodes were kept in containers under argon for as long as possible. The post-testing anodes were sputter-coated with gold prior to characterization to prevent further damage from exposure to atmosphere and the characterization process.

2.2 Sample Characterization

2.2.1 Scanning Electron Microscopy / Energy Dispersive Spectroscopy

The surface characteristics and particle sizing of the anode disc samples were examined using scanning electron microscopy (SEM) with a Hitachi S-4800 microscope. A working distance of 12 mm and acceleration voltage of 20 kV were retained throughout the imaging process. Energy-dispersive X-ray spectroscopy (EDS) was performed using an Oxford EDS system on both anode disc samples and sample coatings annealed on tantalum foil. Data were analyzed using the Oxford Instrument’s INCA and AZTEC software. An image of the equipment and setup are included in Fig. 15.

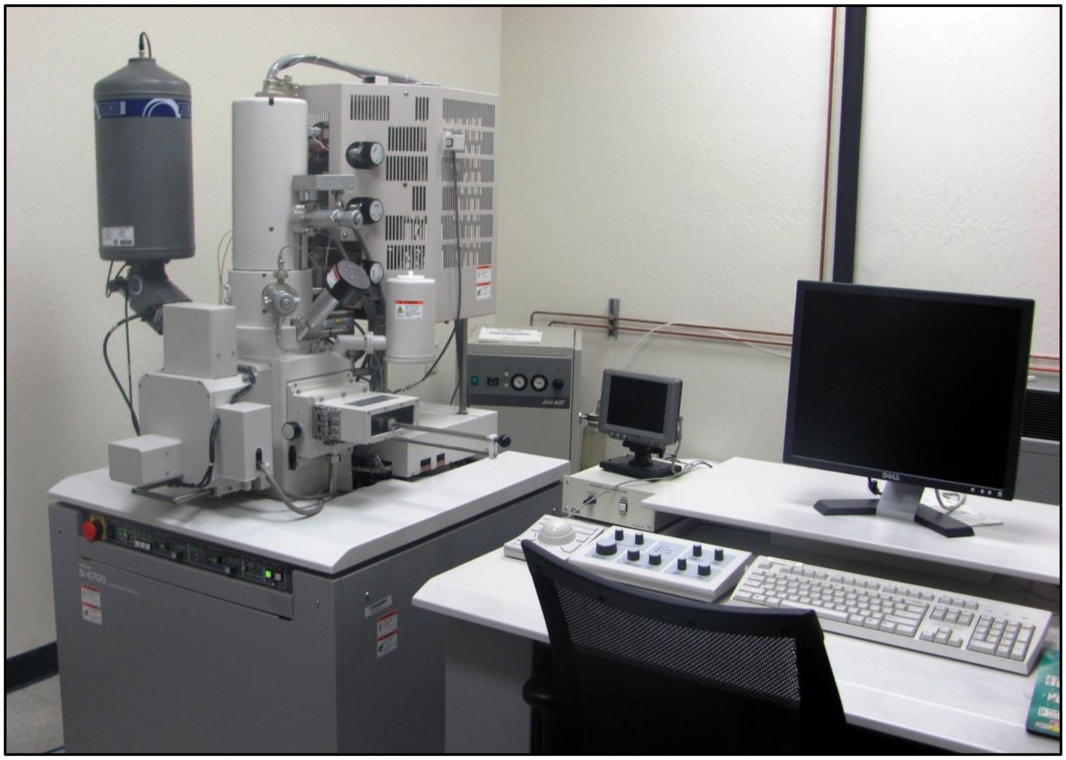

Fig. 15: Hitachi S-4800 scanning electron microscope (SEM) and attached Oxford energy-dispersive X-ray spectroscopy (EDS) system used for surface characterization of the samples.

2.2.2 Inductively Coupled Plasma Optical Emission Spectrometry

Inductively coupled plasma optical emission spectrometry (ICP-OES) analysis was conducted using a PerkinElmer ICP-OES 8000 to confirm the presence and composition of copper within the experimental samples. For ICP-OES, 0.1 g of each sample material annealed on tantalum foil was dissolved in 0.5 mL of nitric acid. Mixtures were heated in a boiling water bath for approximately 40 minutes, and then they were diluted with deionized water. Calibration standards were purchased from SCP Science, and reported results showed less than 3% relative standard deviation. An image of the equipment is shown in Fig. 16.

PerkinElmer
Optima 8000

Fig. 16: PerkinElmer inductively couples plasma optical emission spectrometer (ICP-OES) 8000 used to assess the copper content of anode materials after heat treatment.

2.2.3 Raman Spectroscopy

Raman spectroscopy was also performed on the materials to characterize the surface of the anode discs. This step was conducted using a Thermo Scientific DXR Raman Microscope with a 532-nm laser at 10 mW power. The Raman data were collected at 10x magnification and a spot size of 50 µm. Several spots were analyzed for this process, and results appeared consistent across the surface of the anode. The data reported is representative of the whole selection of data obtained across the sample. The instrument and setup for the microscope is shown in Fig. 17.

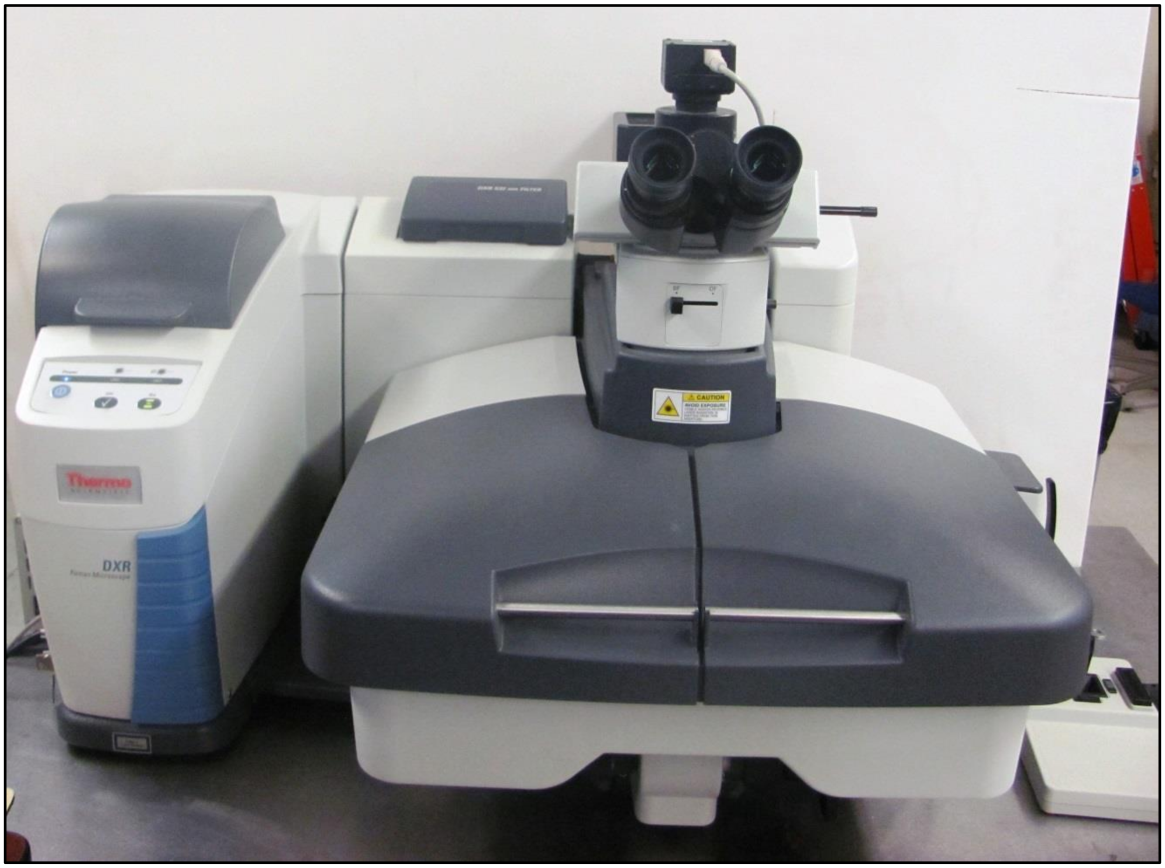

Fig. 17: Thermo Scientific DXR Raman Microscope used for characterization of the anode disc surfaces. Data were obtained at 10x magnification and a spot size of 50µm.

2.2.4 X-ray Diffraction

The samples were then investigated using X-ray diffraction (XRD) with a Rigaku SmartLab XRD using CuKα radiation. Samples coated on tantalum foil were ground into a fine powder and prepared on a glass stage for this step. All patterns were collected over the range of 2θ = 20° to 100° with a step size of 0.07º and at a scan rate of 0.5ºmin^{-1}. Rigaku PDXL2 analysis software and JCPDS cards were used in assessing the XRD data. Figure 18 shows the X-ray diffractometer.

X-RAYS ON
Rigaku
EMO
SmartLab
X-RAY DIFFRACTOMETER

Fig. 18: Rigaku SmartLab X-ray diffractometer (XRD) used to characterize the anode samples. All patterns were collected over the range of 2θ = 20° to 100° with a step size of 0.07º and at a scan rate of 0.5ºmin^{-1}.

2.3 Electrochemical Measurement

2.3.1 Electrochemical Impedance Spectroscopy

The fabricated coin cells were tested using electrochemical impedance spectroscopy (EIS) measurements performed with an Ametek PARSTAT 4000 instrument. A frequency range from 100 kHz to 0.01 Hz was used to test the coin cells containing the sample anodes. Reported data show the average plot from three test trials for each anode type.

2.3.2 Charge/Discharge Cycle Testing

To assess important performance variables for each anode material, charge and discharge cycling of the cells was performed using an MTI multichannel battery analyzer rated for use with a maximum voltage reading of 5.0 V and a maximum current reading of 1 mA. Test schedules were programmed using the MTI battery analyzer software. The cells were cycled galvanostatically in the voltage range from 0.01 V to 1.5 V at room temperature. To establish active layer lithiation and SEI layer development, cells were scheduled to first complete two cycles at a lower current density of 100 mAg^{-1} before proceeding to full testing [65]. These two cycles were considered preparatory and were thus not included in the reported results. Following this step, all sample tests were performed at a current density of 250 mAg^{-1}. The testing current rate for each cell was then calculated using this value and the active material mass loading for the anode type. Anodes from the low temperature study were tested for 50 cycles, and subsequent anodes were tested for 100 cycles. The battery analyzer apparatus setup is shown in Fig. 19.

Figure 20 shows a close view of the coin cell testing board attachment that houses eight coin cells for testing.

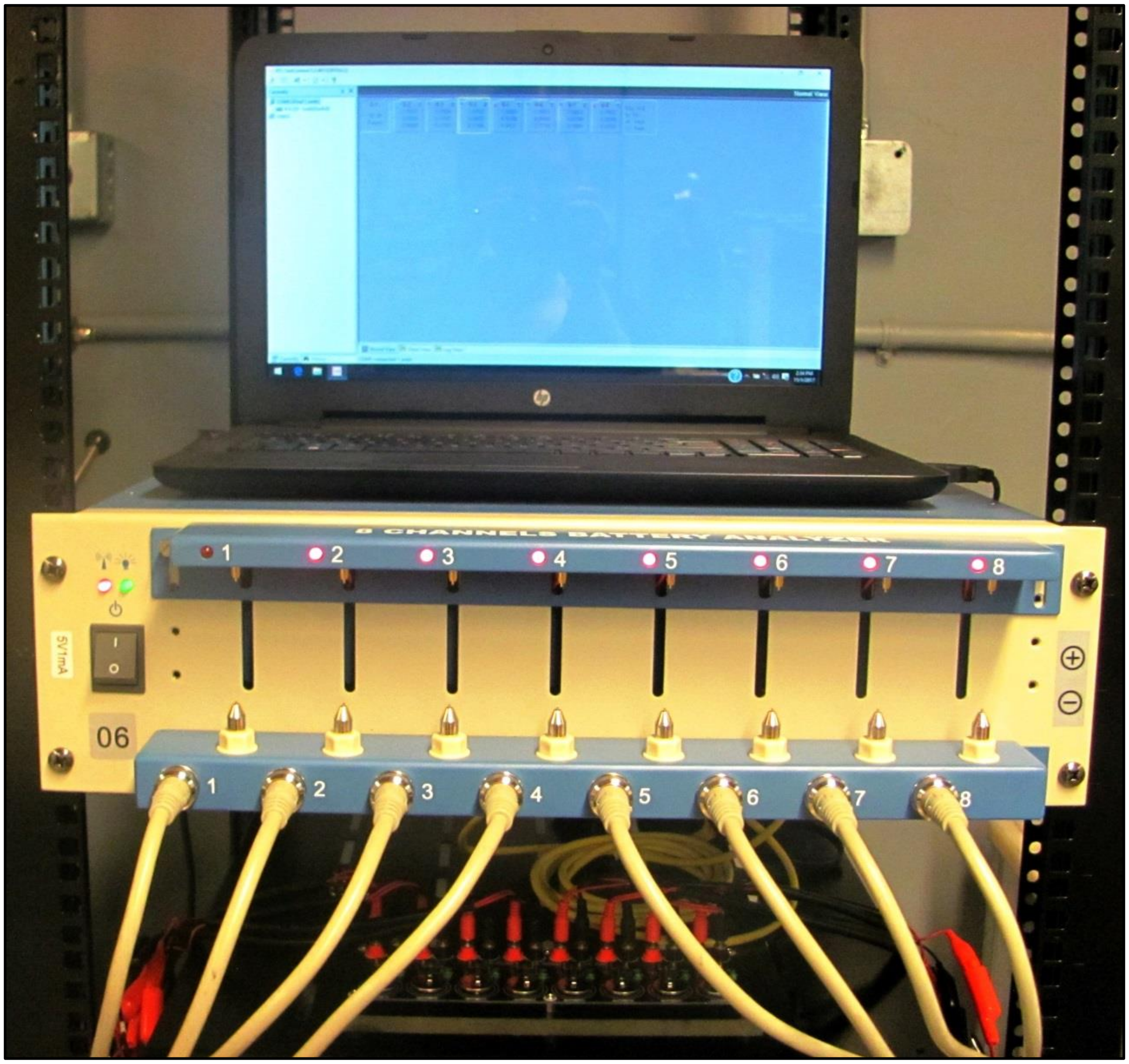
8 CHANNELS BATTERY ANALYZER
1
2
3
4
5
6
7
8
5V1mA
06
1
2
3
4
5
6
7
8

Fig. 19: MTI multichannel battery analyzer with attached laptop (above) and coin cell testing board (below). The laptop display shows the battery analyzer software used to program the test schedules for the eight channels.

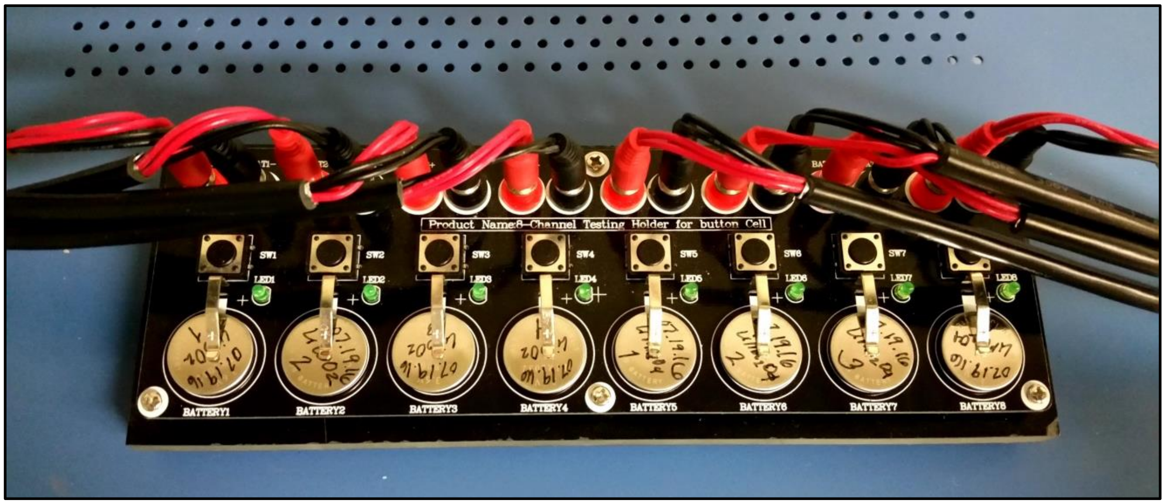
Product Name:8-Channel Testing Holder for button Cell
SW1
SW2
SW3
SW4
SW5
SW6
SW7
LED1
LED2
LED3
LED4
LED5
LED6
LED7
LED8
BATTERY1
BATTERY2
BATTERY3
BATTERY4
BATTERY5
BATTERY6
BATTERY7
BATTERY8

Fig. 20: MTI coin cell testing board which houses eight coin cells. The board is an attachment to the battery analyzer.

Chapter 3: Results and Discussion

3.1 Low-Temperature Anodes

This section includes the results from qualitative observations and electrochemical testing of the low-temperature anode materials. Two studies were conducted using the low-temperature heat treatment procedures as described in Chapter 2: one batch used the standard procedure while the other included an additional ball milling step. Discussion of the results is also provided to elucidate the main lessons learned from these studies.

Coin cells fabricated using anodes of the two different low-temperature materials (Si only and Si-Cu) were tested electrochemically to assess their performance characteristics. MTI analyzers were programmed to apply a lower current of 100 mAg^{-1} for two cycles followed by a current of 250 mAg^{-1} for 50 cycles as explained in the methods from Chapter 2. Applied current for each anode was calculated using the mass loading of active material for the specific anode. At least three anodes of the same batch were tested simultaneously to ensure the quality and consistency of the results. Variability between the anodes was common in testing, but outliers from the general trends of the batch were a rare occurrence. During data assessment, the results for a group of anodes were plotted together, and the data for the average anode were used as the representative of the batch. The methodology used for reporting cycling data is rarely included in literature, and reported data is typically shown for a single anode without indicators for deviation. This method was developed to ensure that data was accurately representative of the batch but was also compatible with the formatting of published reports. A visualization of the process of selecting the representative data for an anode batch is shown in Fig. 21.

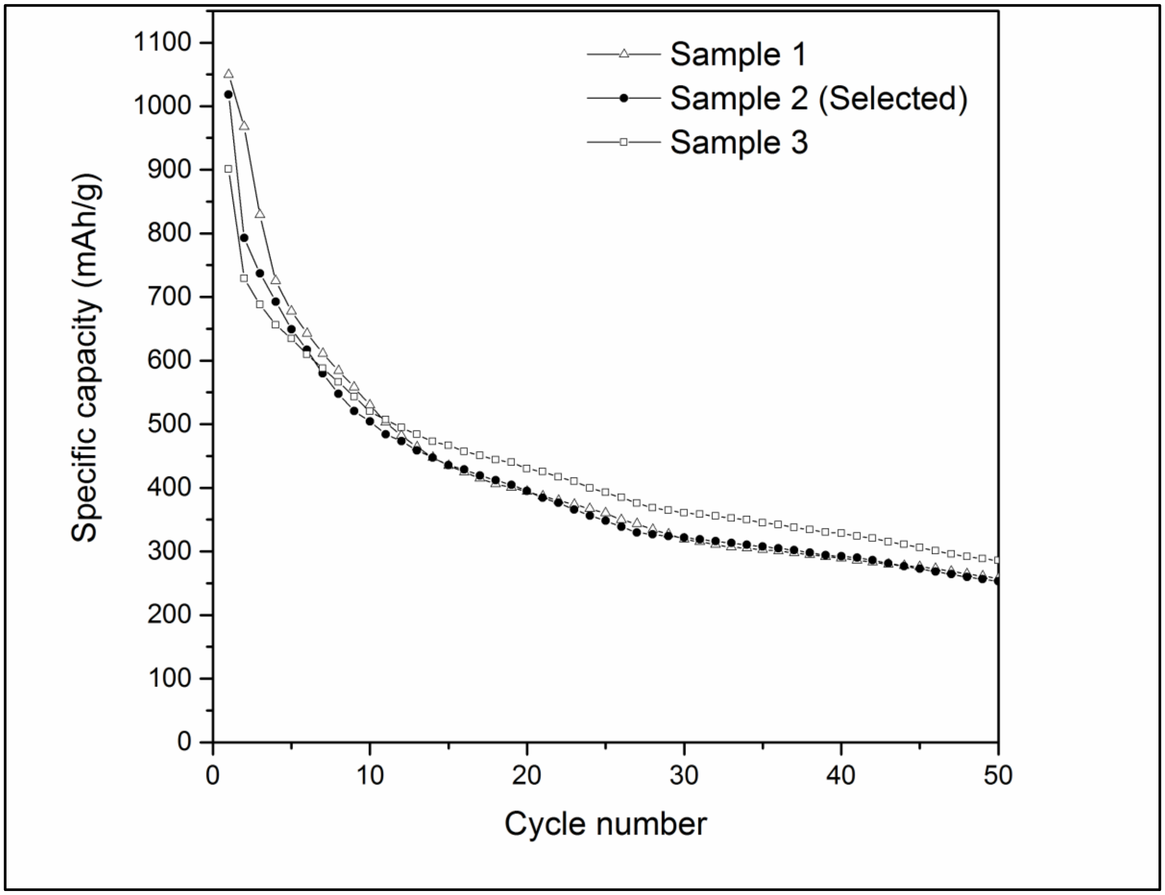

Fig. 21: Example plot of the performance for three anodes of the same batch (low-temperature Si-Cu) for comparison. Noticeable variabilities exist between the different samples; therefore, the data from the most-average sample from the group (Sample 2 in this scenario) is used as a representative for the batch.

The specific capacity values for the Si only and Si-Cu anodes are plotted as a function of cycling for the 50-cycle test, and this graph is shown in Fig. 22. Capacity values were maintained in specific terms per unit mass so that direct comparisons could be made for the material between anodes of different mass loading values. Figure 23 shows the Coulombic efficiencies of both Si only and Si-Cu anodes plotted as a function of cycling.

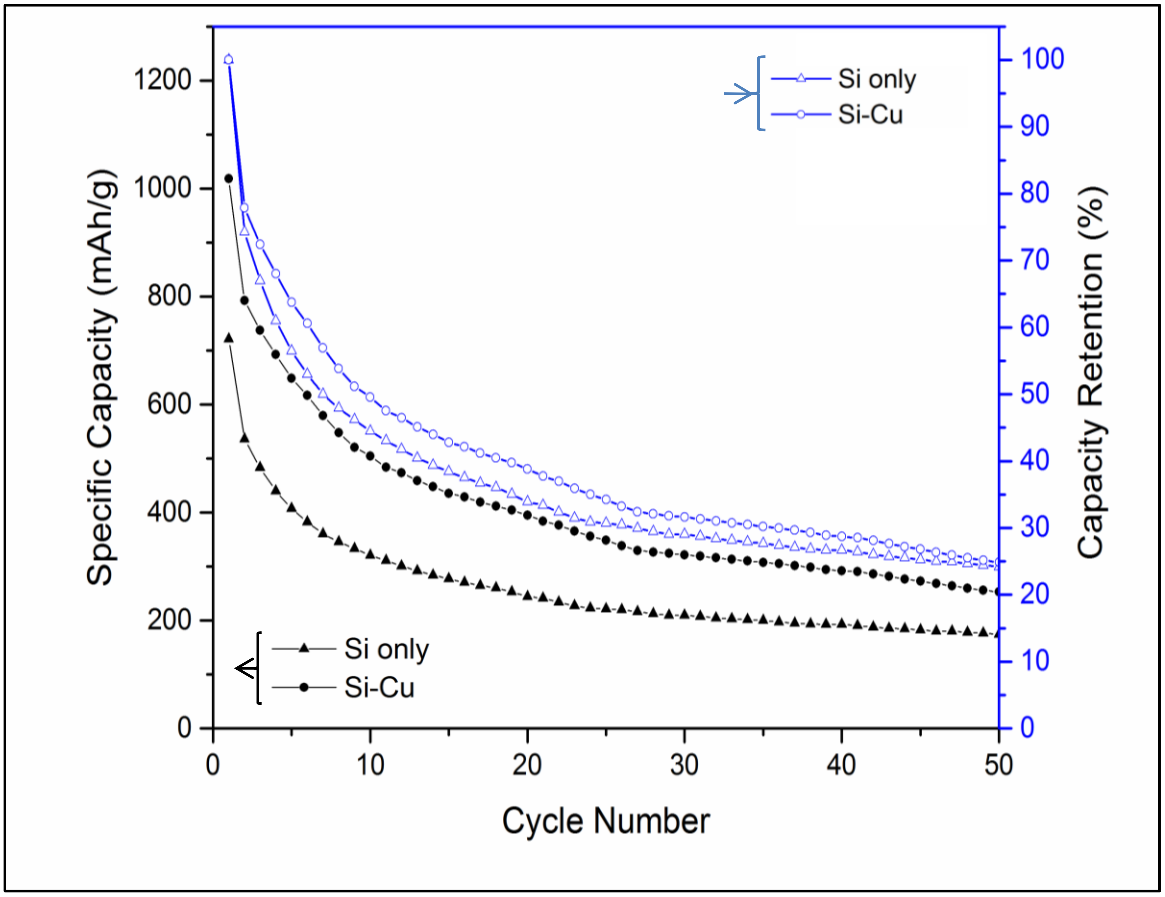

Fig. 22: Charge/discharge cycling results for 50 cycles for low-temperature Si only and Si-Cu anodes cycled at 250 mAg^{-1} current density. Initial capacities reached above 700 mAhg^{-1} and 1000 mAhg^{-1} for Si-only and Si-Cu anodes, respectively; however, capacity retention is poor for both materials with over 50% loss within the first 10 cycles.

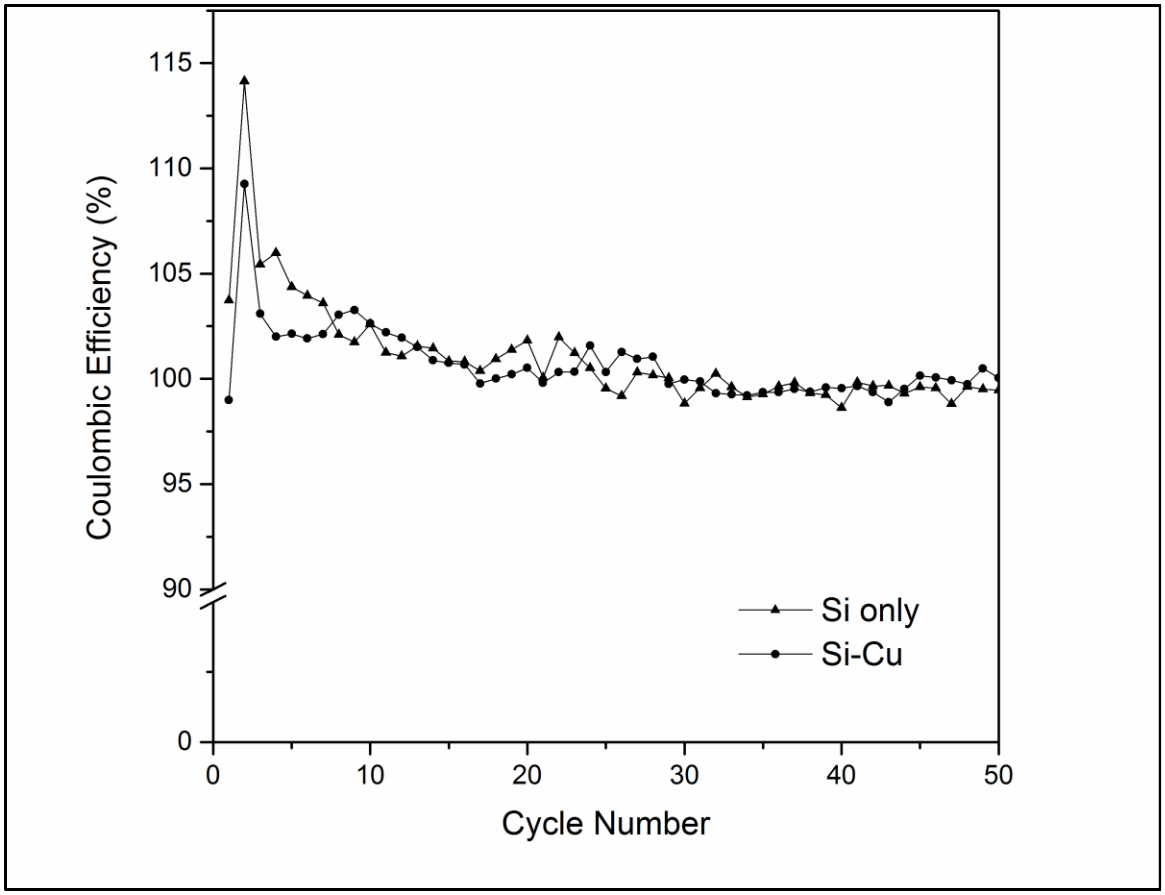

Fig. 23: Coulombic efficiency results from the 50 cycles for low-temperature Si only and Si-Cu anodes. Efficiency behavior is shown to be erratic and have poor stability within the first 30 cycles.

From the results shown in Fig. 22, the initial specific capacity values of 722 mAg^{-1} and 1018 mAg^{-1} were reached for the Si only and Si-Cu anodes, respectively. The Si-Cu anode maintained higher capacity throughout the duration of the test and completed 50 cycles with 253 mAg^{-1} capacity while the Si only anodes attained 174 mAg^{-1} capacity. Capacity retention for both cells is relatively low with over 50% capacity loss within the first 10 cycles of the test; over the 50 cycle duration, the anodes retained only 24% and 25% capacity for Si only and Si-Cu, respectively.

The Coulombic efficiency values for the Si only and Si-Cu anodes are shown to have significant irregularity and exceed unity for multiple cycles in Fig. 23. Though efficiency results shown in literature may occasionally include a data point of over 100% as an anomaly, the bulk of the data should generally reflect that the discharge capacity does not exceed the charge capacity during cycle testing. However, efficiency data was relatively repeatable across the groups of tested anodes for both the Si only and Si-Cu batches. As shown in Fig. 23, the two data sets follow approximately the same pattern of high initial efficiency and gradual convergence towards 100%.

Though these anodes were able to be successfully cycled over 50 times, the qualitative appearance of the anode surfaces also raised concern. The application of the slurry mixture on the current collector foil was smooth, but the texture of the coating had a visibly grainy nature before and after the heat treatment step. For this reason, a second set of low-temperature anode batches was made with an additional ball milling step for the dry active material in an attempt to reduce particle size. After ball milling, it was qualitatively noted that the material seemed to have fewer larger grains. However, the material also showed a tendency to form small clumps, and there was a significant loss of material from the sides of the ball milling containers. Slurry mixtures made from the milled material appeared to be slightly less grainy after the casting process. The anodes were electrochemically tested using the previously described method, and the specific capacity versus cycle number graph, shown in Fig. 24, compares the results for the Si only and Si-Cu anodes. Figure 25 shows the Coulombic efficiencies of the two anodes as a function of cycling.

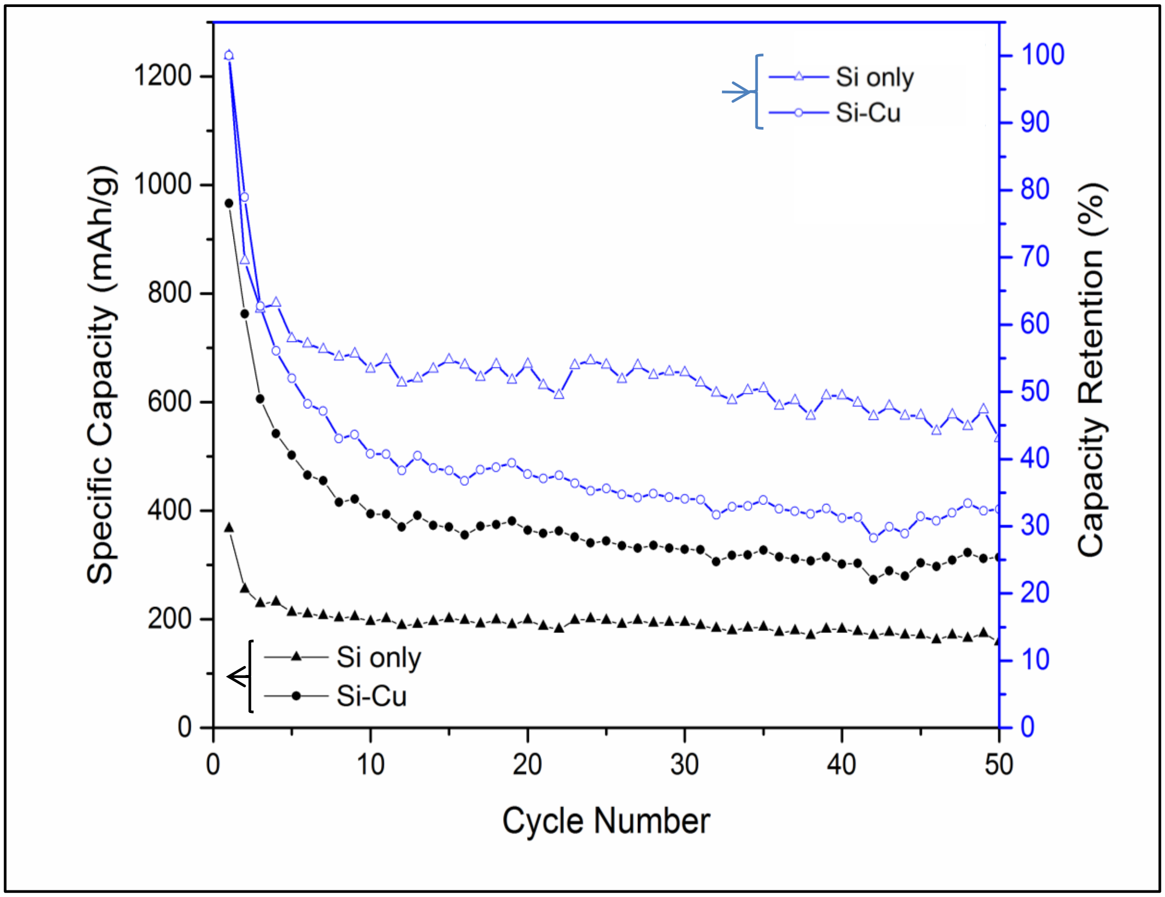

Fig. 24: Charge/discharge cycling results for 50 cycles for Si only and Si-Cu ball-milled anodes cycled at 250 mAg^{-1} current density. Results are similar to the previous low-temperature anode results with significant immediate capacity loss.

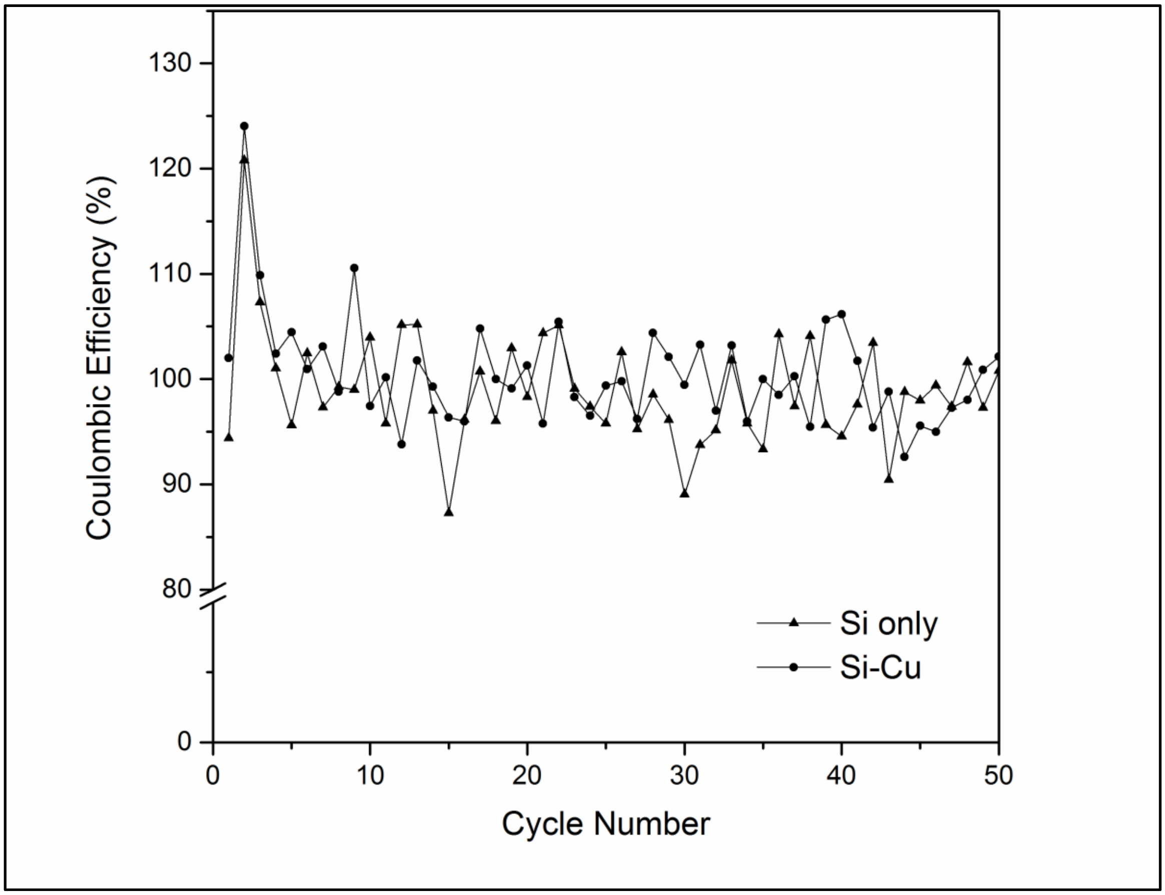

Fig. 25: Coulombic efficiency results for the Si only and Si-Cu ball-milled anodes. Efficiency results are also similar to the initial low-temperature results.

As shown in Fig. 24, the ball milled low-temperature anodes show similar performance behavior to that of the anodes that were not ball milled. Both data sets exhibit a steep capacity fade within the first 10 cycles of the test and follow a modest decline in capacity value for the remaining cycles. A wider disparity between the capacity values for the Si only and Si-Cu anodes is apparent from the graph. Initial capacities were 346 mAg^{-1} and 966 mAg^{-1} for Si only and Si-Cu anodes, respectively; capacities for the fiftieth cycle are 159 mAg^{-1} and 314 mAg^{-1} for Si only and Si-Cu, respectively. Though similar behavior was observed, the capacity retention from these anodes was improved over the previous anodes at 46% for Si only and 33% for Si-Cu anodes.

Coulombic efficiency for both anodes also followed a similar trend as previously described. The efficiency values were erratic and exceed 100% often throughout the duration of the testing. However, the efficiencies for the ball milled anodes showed a wider range of variability. This instability was also vaguely present in the data shown in Fig. 24 as the capacity curves were not as smooth as those shown in Fig. 22. Though noticeably different, this level of erraticism was fairly common and accepted in literature and was visible in the data presented in the report by Cetinkaya *et al.* [98]. It is also not uncommon for efficiency curves to be absent in literature, but reported curves do not exhibit this type of behavior when included.

The electrochemical results obtained from testing both batches of low-temperature anodes showed room for improvement in capacity retention with generally less than 50% capacity retained after 50 charge/discharge cycles. These results were comparable with similar experiments in literature. The silicon and silicon-graphite composite anodes tested by Cetinkaya *et al.* exhibited similar behavior of high initial discharge capacities (930 mAhg^{-1}) that degrade to 45% of this value on the fiftieth cycle [98]. Fang *et al.* also tested anodes with compositions of silicon and silicon with increasing amounts of copper nanoparticles; results from electrochemical testing of these anodes yielded capacity retentions of 11.4%, 27.2%, 44.4%, and 38.6%, respectively [78]. The increased retention values were stated in the report to be a result of the copper content in the anode, though the results from the low-temperature anode study in this report are unable to support this hypothesis. From this study, it was inconclusive whether or not the copper additive could contribute to the retention of the anode; however, it was shown that ball milled anodes displayed greater capacity retention despite having less stable performance behavior.

From the results, the initial and final capacity values of Si-Cu anodes were substantially increased relative to the Si only anodes; all Si-Cu anodes maintained higher capacity values throughout the 50-cycle test duration. The immediate improvement of the anodes was important considering the simplicity of the fabrication methods. With only a minor addition of copper and rudimentary methods of incorporation into the silicon structure, the anodes exhibited an appreciable difference in performance behavior.

Cycling results from these experiments also showed that an additional 30-minute ball milling step provided both an advantage and disadvantage for the material: though retention was improved, stability was noticeably reduced. As shown in Gauthier *et al.*, the greatest difference between the performances of as-received and ball milled materials is the retention: the Gauthier *et al.* report and this report both showed relatively unchanged initial capacity yet higher final capacity for ball milled anodes [97]. Longer ball milling time could be tested in conjunction with more in-depth particle size analysis; however, milling jars of alternative materials, such as stainless steel, should also be considered to increase material recovery.

One of the concerns from these results was the erratic behavior of the cells while cycling. For this reason and also in pursuance of greater improvement in anode performance, techniques for sample fabrication needed to be explored further.

These preliminary studies provided a sufficient proof-of-concept for the benefits of using copper additive with silicon-based anodes. Results were shown to be comparable to those in literature using similar procedures, and the increased capacity of anodes with copper additive was clearly demonstrated. The work also established the basis of the fabrication protocols, testing parameters, and data processing that would be used throughout subsequent studies. After analysis of the results, more literature was reviewed to identify alternative processing techniques that would yield anodes with greater improvement in performance characteristics. Many successful reports have described using a heat treatment step at much higher temperatures for the anode materials [65, 77, 87, 100, 101]. Thus, the initial study with high-temperature heat-treated anodes was performed.

3.2 Initial High-Temperature Anodes

This section includes the results from the qualitative observations, basic characterization, and electrochemical testing of the initial high-temperature anode materials. These were the initial experiments in using a higher temperature heat treatment procedure as described in Chapter 2. Discussion of the results is provided, and rationale for the adjustments made to this procedure to produce the final high-temperature anodes is included.

3.2.1 Sample Characterization

Anodes were prepared using the protocol as described in Chapter 2 using a high-temperature heat treatment step at 700 ºC. Following heat treatment, the coating surface did not share the same grainy texture of the low-temperature anodes; instead, surfaces were relatively smooth with faint cracking in some regions. Anode discs were punched and examined using the scanning electron microscope (SEM) with energy dispersive spectroscopy (EDS) capabilities. Images at 30x magnification of the general appearance of the anode disc surfaces for the Si only and Si-Cu anodes are shown in Fig. 26.

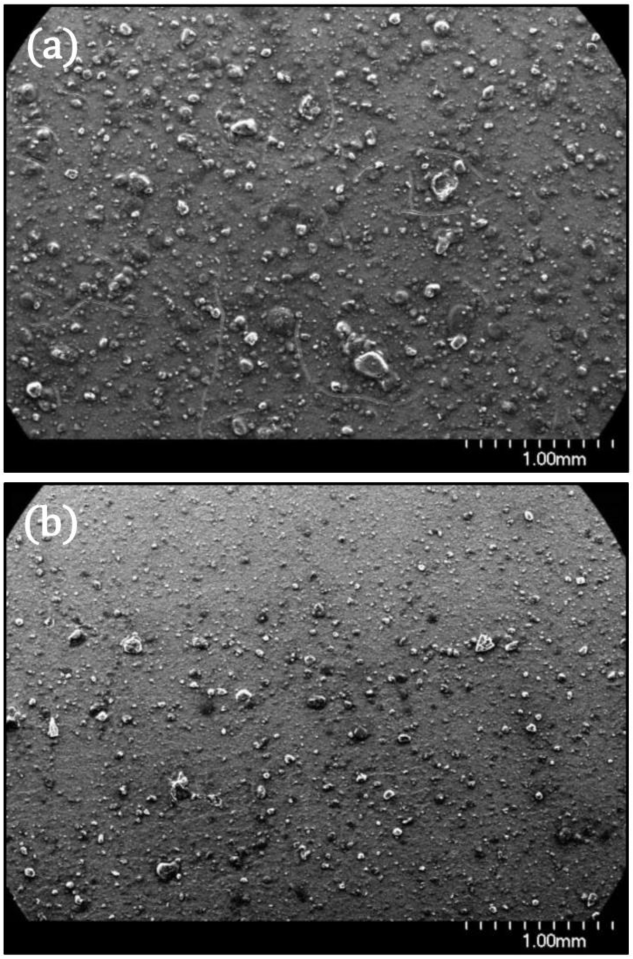

Fig. 26: SEM images of the overall surfaces of the (a) Si only and (b) Si-Cu anodes at 30x magnification. Surfaces are grainy in texture, but large grains are dispersed evenly across the surface for both materials.

As shown, both Si only and Si-Cu anode surfaces were comprised of multi-sized particles atop a fairly homogeneous base layer of smaller-sized particles. In both samples, faint cracks are evident across the surface but are short in length relative to the size of the anode. Images collected at 20k-x magnification provide greater insight into the structure of the base layer as shown in Fig. 27.

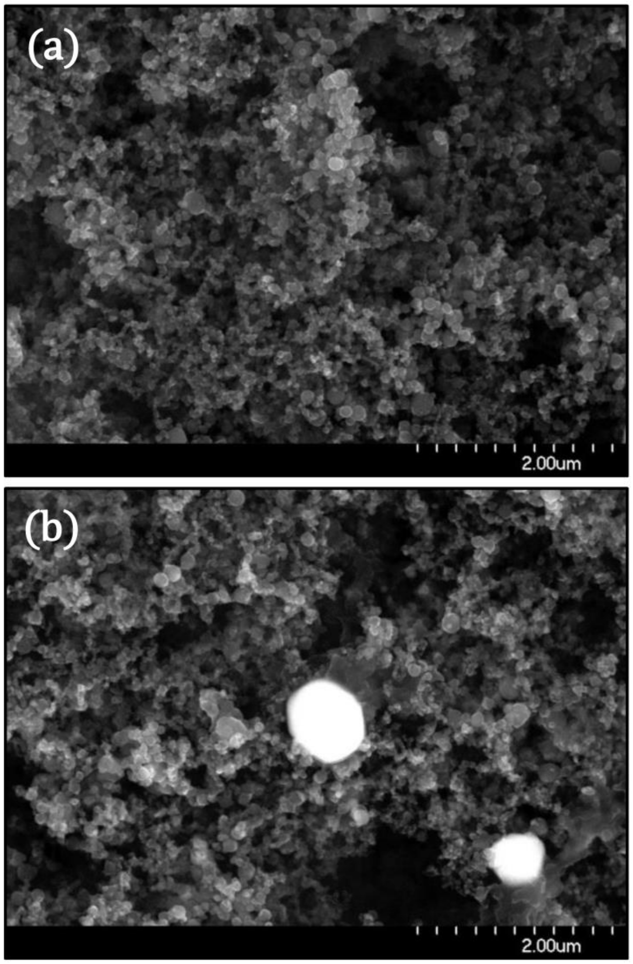

Fig. 27: SEM images showing the particle sizing and texture of the (a) Si only and (b) Si-Cu anodes at 20k-x magnification. Agglomerates of smaller particles ranging in size on the nanometer scale compose the base layer of the coating. Large copper particles are also found on the Si-Cu anode surface.

Images at 20k-x magnification show that the base layer is comprised of nanoscale particles in a homogeneous mixture across the surfaces. Si-Cu anodes also showed an even dispersion of larger copper particles of approximately 0.8 µm diameter atop the base layer. The particles were determined to be copper from an EDS line scan analysis at 40k-x magnification, and the results are shown in Fig. 28. In the spectra, the region of particles is shown to have a dramatic increase in copper and decrease in silicon content, and the surrounding background is a mixture of silicon, oxygen, carbon, and copper.

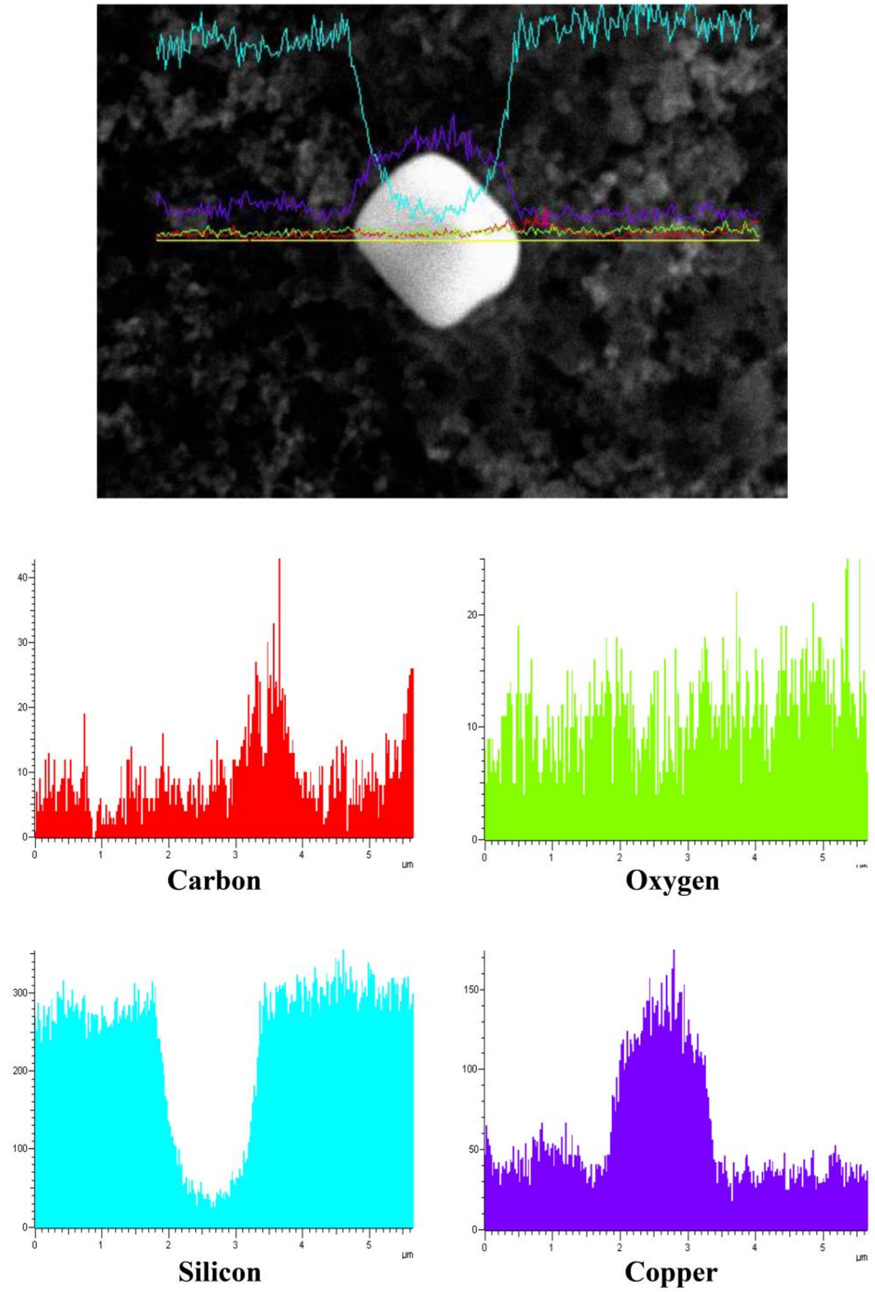

Carbon

Oxygen

Silicon

Copper

Fig. 28: EDS line scan of a copper particle on the anode surface at 40k-x magnification. Colored graphs show the elemental composition across the sample scan line through the particle, and they indicate a clear confirmation that the particle is copper against the primarily silicon base layer.

The characterization techniques used in this study provided a qualitative analysis of the surface of the Si only and Si-Cu anodes. A network of nanoscale particles provides the structure of the base layer of the coating, and larger particles and structures are visible on top. Copper is shown to be both integrated into this base layer and also as larger particles evenly scattered atop the surface. Small cracks are visible at lower magnification which could contribute to the anode degradation over electrochemical testing.

3.2.2 Electrochemical Measurement

The experimental anode discs were also used in the fabrication of coin cells with lithium foil discs so that their performance characteristics during electrochemical testing could be analyzed. Charge/discharge tests for the cells used the parameters described in Chapter 2, and the duration of the tests was extended to 100 cycles to observe longer-term cycling behaviors. Figure 29 shows the graph of the specific capacities of the Si only and Si-Cu anodes as a function of cycling. The results for the Coulombic efficiencies of both anodes are shown in Fig. 30.

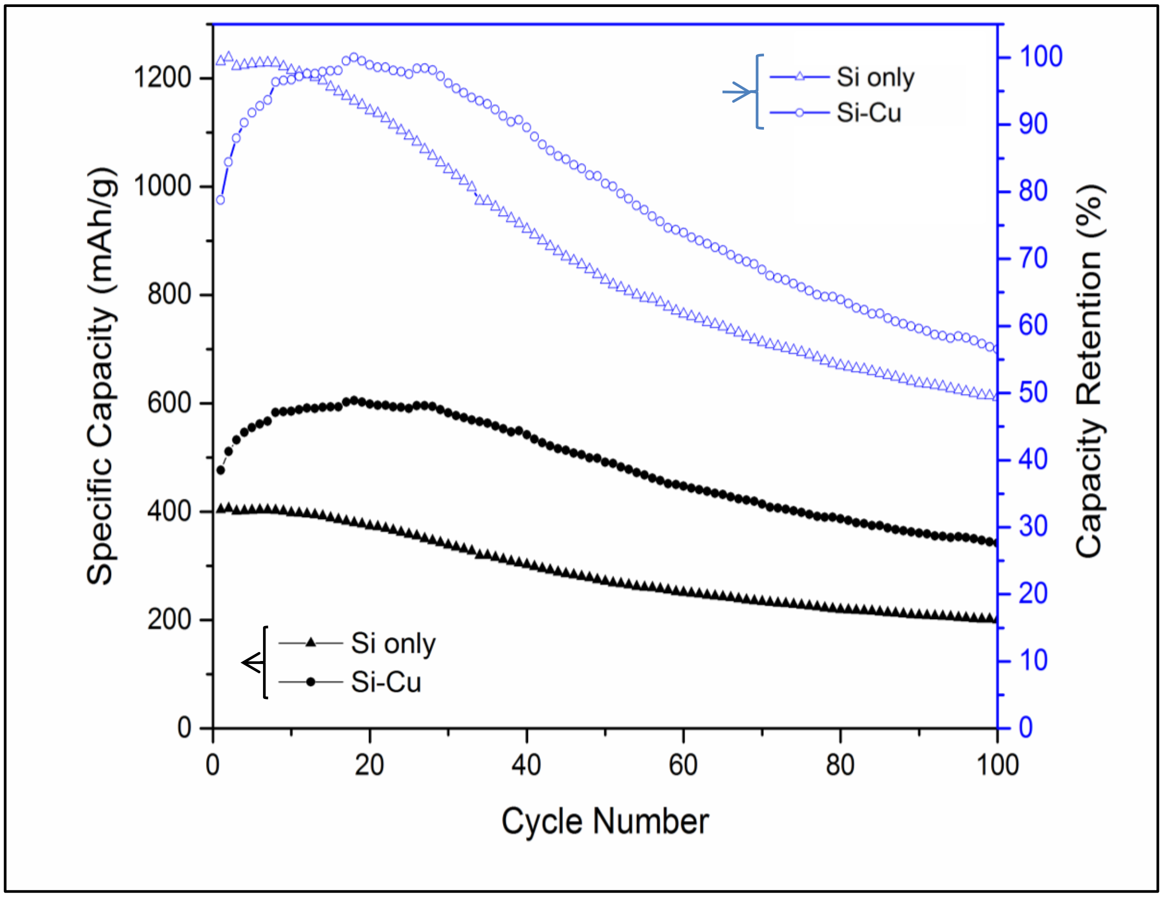

Fig. 29: Charge/discharge cycling results for 100 cycles for Si only and Si-Cu initial high-temperature anodes cycled at 250 mAg^{-1} current density. Though results yield lower initial capacity values than those of the low-temperature anodes, capacity retention and long-term stability is much improved.

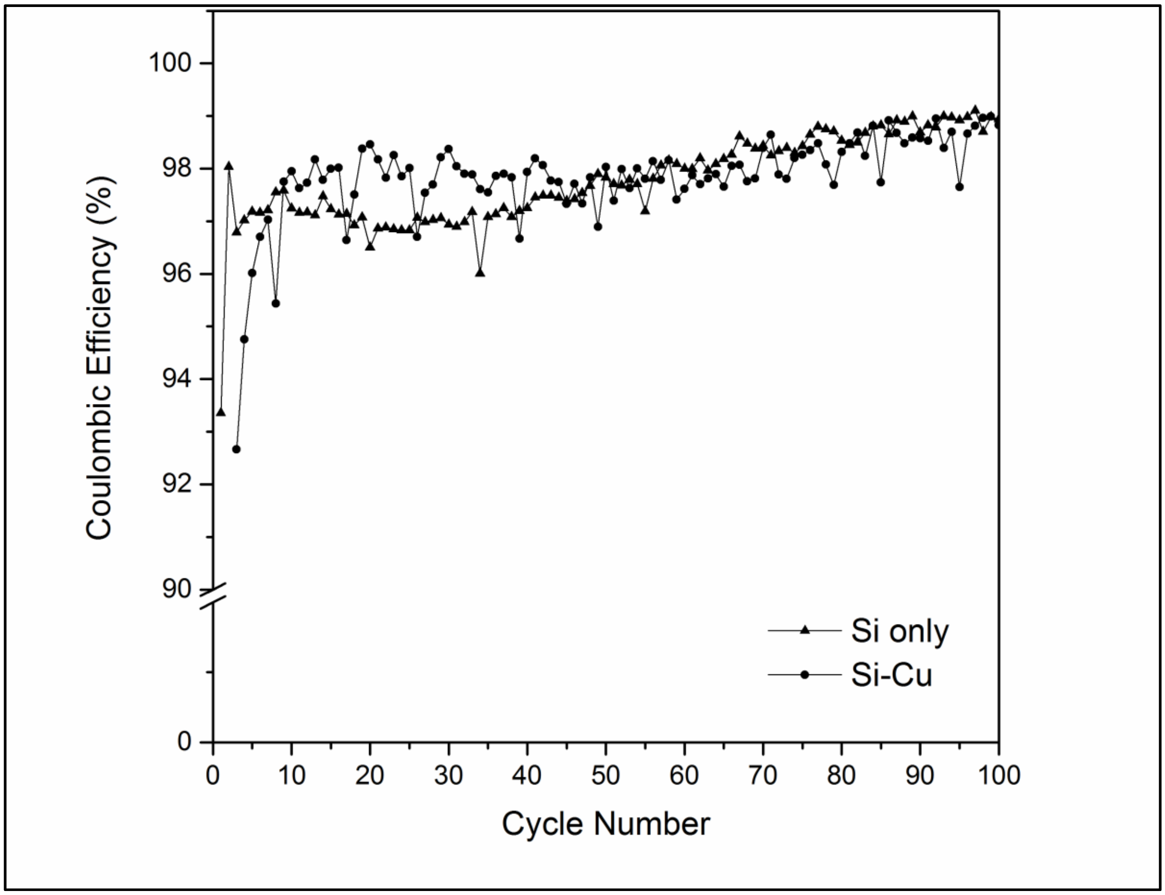

Fig. 30: Coulombic efficiency results for the Si only and Si-Cu initial high-temperature anodes. Efficiency results show greater stability compared to low-temperature results and overall improvement over cycling duration.

The initial specific capacity of the Si-Cu anode was lower than the capacities previously discussed in Section 3.1 at 481 mAg^{-1}, but it rose to 604 mAg^{-1} within the first 20 cycles; the initial and highest capacity for the Si only anode was 405 mAg^{-1}. The final capacity after 100 cycles for the Si-Cu anode was also higher at 349 mAg^{-1} than that of the Si only anode at 199 mAg^{-1}. The capacity retentions of the anodes were therefore 49% and 58% for Si only and Si-Cu, respectively. The overall capacity curves showed a different initial behavior from the curves for the low-temperature anodes: the dramatic initial capacity fade was absent, and the fade was more evenly distributed across the 100 cycles. Final capacities of the high-temperature anodes at 100 cycles were also higher than those of the low-temperature anodes after only 50 cycles.

The Coulombic efficiencies of the high-temperature anodes were also improved. The trend of the plot was a more accurate representation of the expected behavior of cell efficiency: lower in initial cycles with steady improvement and values less than 100%. The Si-Cu cell showed slightly more scattered behavior in early cycles, but both anodes reached nearly 99% efficiency by the completion of the cycle testing.

Electrochemical testing of the anodes showed further support that copper additive increased the specific capacity. Capacity retention was also improved for both Si only and Si-Cu anodes compared to the low-temperature anodes, indicating that high-temperature heat treatment can enhance cycling performance. Perhaps the most significant improvement was the stability of the efficiency obtained in this study. Efficiencies for these anodes showed reasonable behavior and reached approximately 99% upon the conclusion of cycling.

These tests served as a first step in understanding the effects of high temperature heat treatment for the anodes and reinforced the concept of silicon anode enhancement via copper additive. Though the presence of copper was detected in the base layer from the EDS analysis, it became of concern that the copper was not as well incorporated into the silicon structure of the anode as initially planned. Much of the copper content appeared to have manifested as larger particles despite efforts to grind down and thoroughly mix the $CuCl_2$ material. Considering this, $CuCl_2$ of finer particle size was purchased for use in the next study for this project. In the next set of experiments, there was also greater focus on explicating the mechanisms of the new anode materials through more rigorous characterization and electrochemical analysis.

3.3 Final High-Temperature Anodes

This section includes the characterization and electrochemical results for the final high-temperature anode materials. Details concerning the smaller-sized $CuCl_2$ used in this study and the fabrication methods are included in Chapter 2. Discussion of the results is provided with a greater emphasis in understanding the benefits of the copper additive and processing techniques. For this study, a third batch was made with $CuCl_2$ and no added carbon black to assess the viability of the copper as the only conductive additive for the material. Anodes of this composition are denoted as “Si-Cu (NC)” throughout the report. It was also noted that many reports in literature perform characterization of the materials prior to important fabrication steps – such as heat treatment – and therefore are not examining an accurate representation of the material to be used in electrochemical applications. In this thesis, anode materials were characterized after all processing steps and just prior to use in electrochemical testing.

3.3.1 Sample Characterization

Qualitative observations of the three anode materials were made using SEM and EDS. To assess the main visual differences between the initial and final high-temperature anodes, anode discs of each Si-Cu batch were examined together. The larger copper particles on the surfaces were highly visible using the backscattered electron (YAG BSE) mode of the SEM as they appear bright white in imaging. The particles were identified as copper. The images for the different high-temperature Si-Cu anodes at 1k-x magnification are included in Fig. 31.

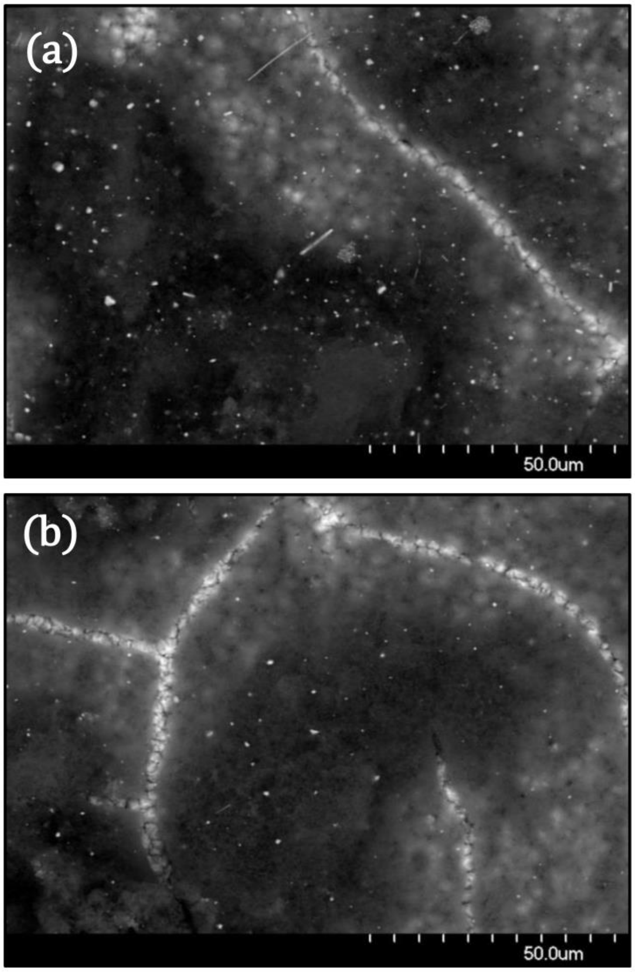

Fig. 31: SEM images showing the particle sizing and texture of the (a) Si-Cu initial high-temperature and (b) Si-Cu final high-temperature anodes at 1k-x magnification and YAG BSE mode. The initial Si-Cu anode visibly has larger copper particles in greater amount than the final Si-Cu anode.

As shown in the images, the high-temperature Si-Cu surface discussed in the previous section had copper particles that are visibly larger than those on the final Si-Cu anode surface. The initial Si-Cu anode also had more of these particles in general across the surface. These observations indicated that the copper additive used for the final Si-Cu anodes was smaller and had improved integration with the silicon structure.

In producing the anode slurry coatings, homogeneity of the copper distribution in the mixture was important to maximize the contact of the copper and silicon for greater conductivity. Figure 32 compares the SEM micrographs of the Si only, Si-Cu, and Si-Cu (NC) anode disc surfaces at 40k-x magnification to examine the distribution of particles.

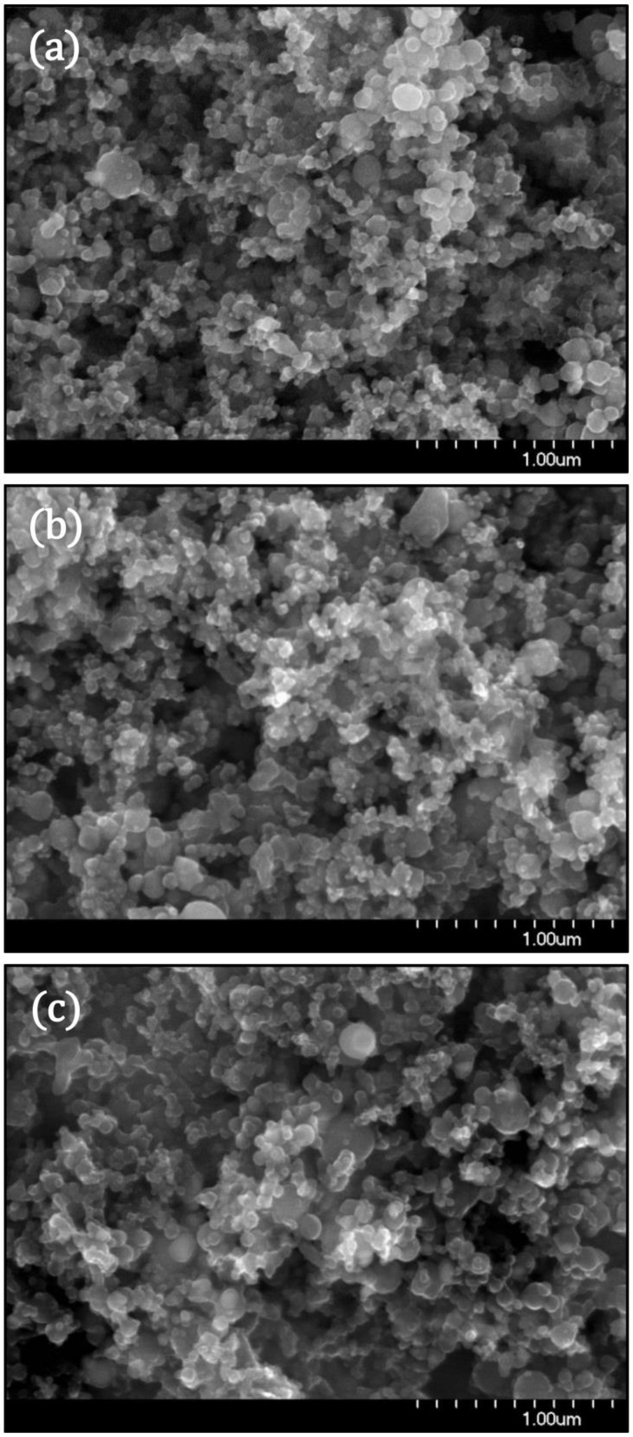

Fig. 32: SEM images using 20 kV accelerating voltage at 40k-x magnification of the anode surfaces prior to cycle testing for (a) Si only, (b) Si-Cu, (c) Si-Cu (NC). The initial surfaces of all three coatings show a similar, homogeneous dispersion of particles with an average size range from 5 nm to 20 nm.

As shown, the surfaces were comprised of particles with nanoscale diameters, and the particles form clusters as previously shown for the initial high-temperature anodes. Particles seen on the anode surface were in the range of 5 nm to 20 nm. Little visual difference can be seen between the three samples, indicating that the use of anhydrous $CuCl_2$ additive did not substantially alter the surface morphology. The particle distribution also appears consistent across the surfaces of the anode discs as there are no anomalous formations.

EDS was utilized to verify the even dispersion of the copper in the base layer of the coating. For this procedure, coatings were annealed on tantalum foil, as described in Chapter 2, to eliminate interference from the copper current collector foil used for the anode discs. The coatings were then removed from the foil following heat treatment and adhered to a stage for EDS analysis. Figure 33 includes the results of EDS elemental mapping of copper for the Si-Cu and Si-Cu (NC) samples where copper content is designated with lighter-colored dots. The elemental mapping was conducted at 40k-x magnification for direct comparison with the images shown in Fig. 32.

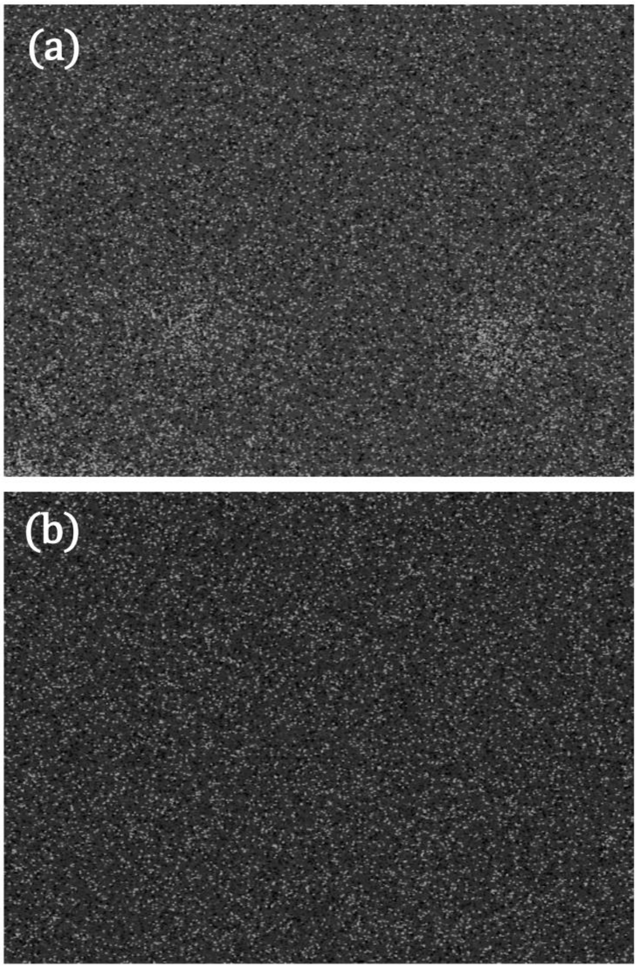

Fig. 33: EDS elemental mapping of the dispersion of copper for the (a) Si-Cu and (b) Si-Cu (NC) samples at 40k-x magnification shows the confirmation of the integrated copper nanoparticles. Copper was uniformly distributed in the silicon-based coating.

From the images, it was confirmed that the copper was uniformly distributed throughout the silicon-based coatings. Elemental mapping of all three anode materials was also conducted to assess the silicon, oxygen, and copper content of the coatings. The approximate weight percentages are included in Table 5.

Table 5: Weight percentages of silicon, oxygen, and copper for the Si only, Si-Cu, and Si-Cu (NC) anodes determined using EDS mapping analysis. Results confirm the low copper content present in Si-Cu and Si-Cu (NC) materials.

	Si only	**Si-Cu**	**Si-Cu (NC)**
Si Content (wt%)	76.6	71.2	73.5
O Content (wt%)	23.1	26.7	25.3
Cu Content (wt%)	0.00	1.7	1.0

EDS analysis confirmed the low weight percentages of copper present in the Si-Cu and Si-Cu (NC) anode materials following all fabrication steps. Relatively small amounts of the copper additive were originally used to promote the goal of cost-effectiveness, and the use of smaller quantities of additive metals has been shown in previous reports to have a significant effect on anode performance [65, 77].

It was also noticed that recent literature does not generally include SEM images collected after the electrochemical testing of silicon anodes. After completing the electrochemical analysis of completing over 100 charge/discharge cycles, the Si only, Si-Cu, and Si (NC) anodes were extracted from their cells inside the glove box. The established procedure was followed in preparing anodes for characterization, and the SEM was used to examine the surface changes. Figure 34 shows the images collected at 30x magnification to provide a general overview of the three surfaces. Figure 35 shows the three surfaces at 40k-x magnification for greater structure detail.

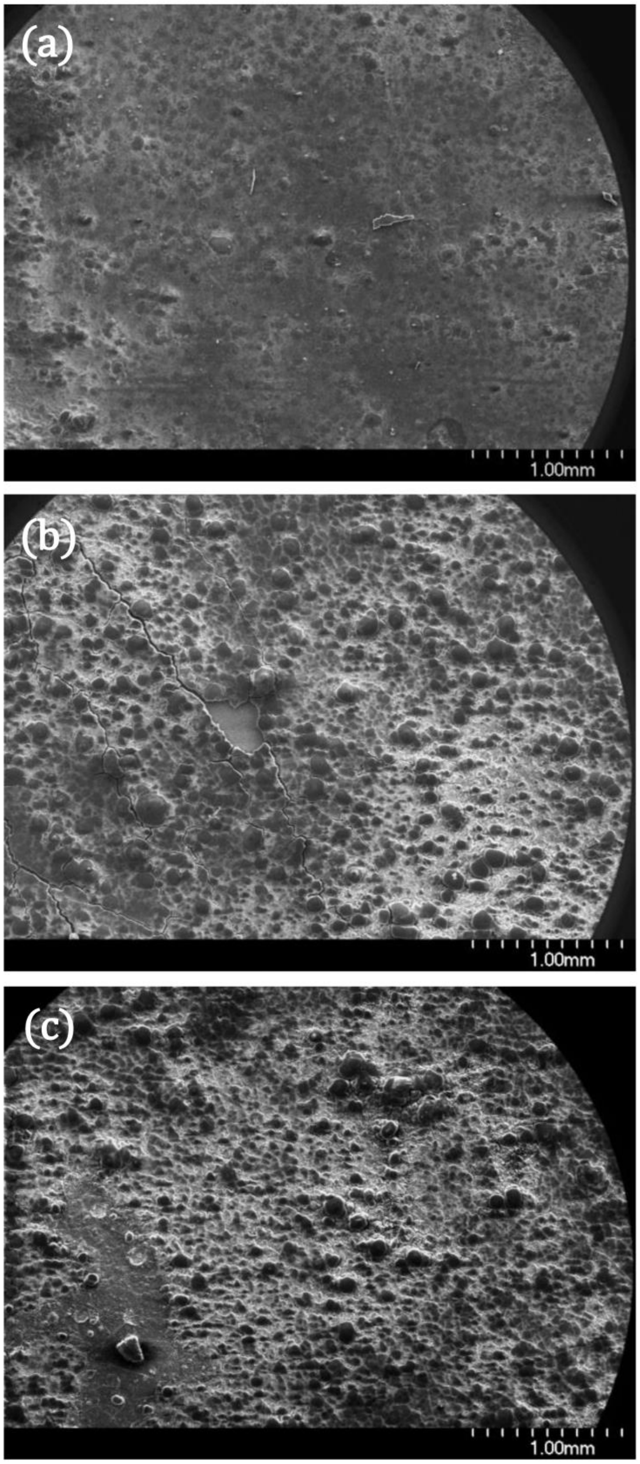
(a)
1.00mm
(b)
1.00mm
(c)
1.00mm

Fig. 34: SEM images using 20 kV accelerating voltage at 30x magnification of the anode surfaces after cycle testing for (a) Si only, (b) Si-Cu, (c) Si-Cu (NC).

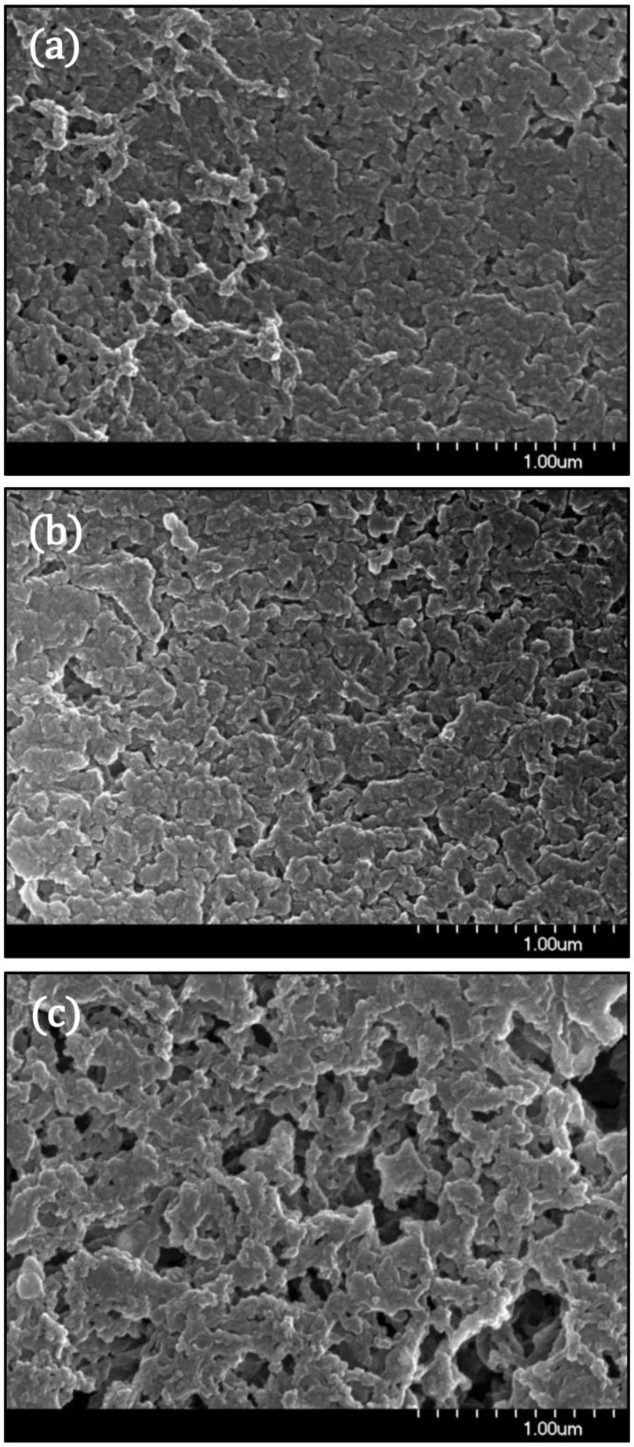
(a)
1.00um
(b)
1.00um
(c)
1.00um

Fig. 35: SEM images using 20 kV accelerating voltage at 40k-x magnification of the anode surfaces after cycle testing for (a) Si only, (b) Si-Cu, (c) Si-Cu (NC).

Post-cycling images can be important to show how the surface morphology of the anode changes with cycling and to identify degradation features. The low magnification images from Fig. 34 show considerable changes from pre-cycled overview images such as those included in Fig. 26. There still appeared to be a distinct difference between the base layer and larger structures on top as shown before; however, the distinction was abstracted by the swelling of the larger structures in the post-cycling anodes. Most notably, the Si-Cu anode had dramatic cracking across the surface. The Si-Cu and Si-Cu (NC) anodes displayed very similar characteristics, whereas the Si only anode had the least evidence of change of the three samples.

The images from Fig. 35 show that all three samples have undergone a considerable transformation in appearance following cycle testing. There was some semblance of the pre-cycling structure visible from the vague outlines of particles and the overall surface arrangement. However, the particles seemed to have swelled to sufficiently lose their definition. Unlike the low magnification view, all three images looked relatively similar as to be undistinguishable from one another. To provide a clear comparison of the effects of cycle testing, images of the Si-Cu anodes before and after cycle testing at 1k-x magnification are included together in Fig. 36.

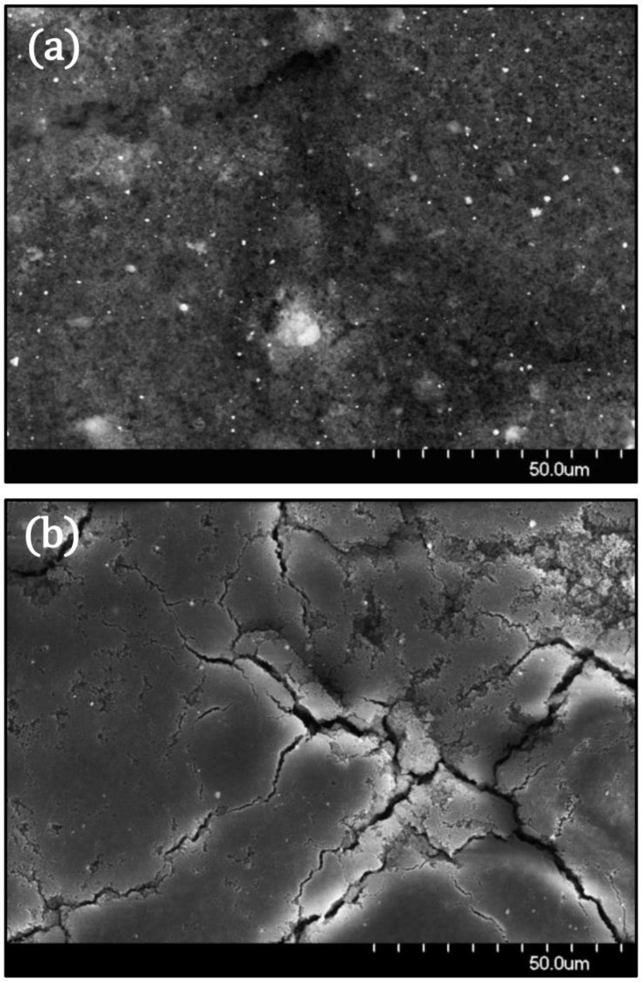

Fig. 36: SEM images showing the surface characteristics of the Si-Cu final high-temperature anodes (a) before cycling and (b) after cycling at 1k-x magnification.

As shown in the images, significant cracking was evident after cycle testing the Si-Cu anode. Despite the clear degradation of the anode surface, it was interesting to note the relatively unchanged presence of the larger copper nanoparticles between both images. The copper particles shown in white were starkly visible in the pre-cycling image, but they were also faintly visible and similarly dispersed in the post-cycling image as well. Though cycling imposed great stress on the anode material, the copper remained an integrated part of the structure.

In all post-cycling images, the distinction between the initial anode material and the decomposed SEI layer was difficult to identify. Because the entire anode surface had come into contact with the electrolyte and solvent following the coin cell assembly process, EDS results showed fairly inconclusive results for this endeavor. A variety of techniques have been used in literature to observe the degradation of electrodes, and the same general effects of cycling have been documented such as cracking, loss of adhesion to the base foil, film formation, and clogging of pores between particles [99].

To corroborate the results of the elemental make-up determined by the EDS analysis, ICP-OES was also conducted on the Si only, Si-Cu, and Si-Cu (NC) materials. The measured amounts of copper present in each sample after the fabrication processes as determined by the ICP-OES analysis are shown in Table 6.

Table 6: ICP-OES results showing the copper content of the Si only, Si-Cu, and Si-Cu (NC) materials following the heat treatment process.

	Si only	**Si-Cu**	**Si-Cu (NC)**
Cu Content (%)	0.00	3.04	2.12

From the results, no copper was detected in the control sample as expected. The Si-Cu and Si-Cu (NC) samples contained 3.04% and 2.12% of copper, respectively. These values supported those determined via EDS in confirming the relatively small copper content present after all processing steps.

To confirm the chemical composition of the anode materials and to elucidate further differences between the samples, Raman spectroscopy was used on the Si only, Si-Cu, and Si-Cu (NC) anode discs. Data were collected at several spots on each anode surface at 10x magnification, and the average data set was selected as representational of the batch using the previously described methodology. Figure 37 shows a comparison of the Raman spectra of the three samples.

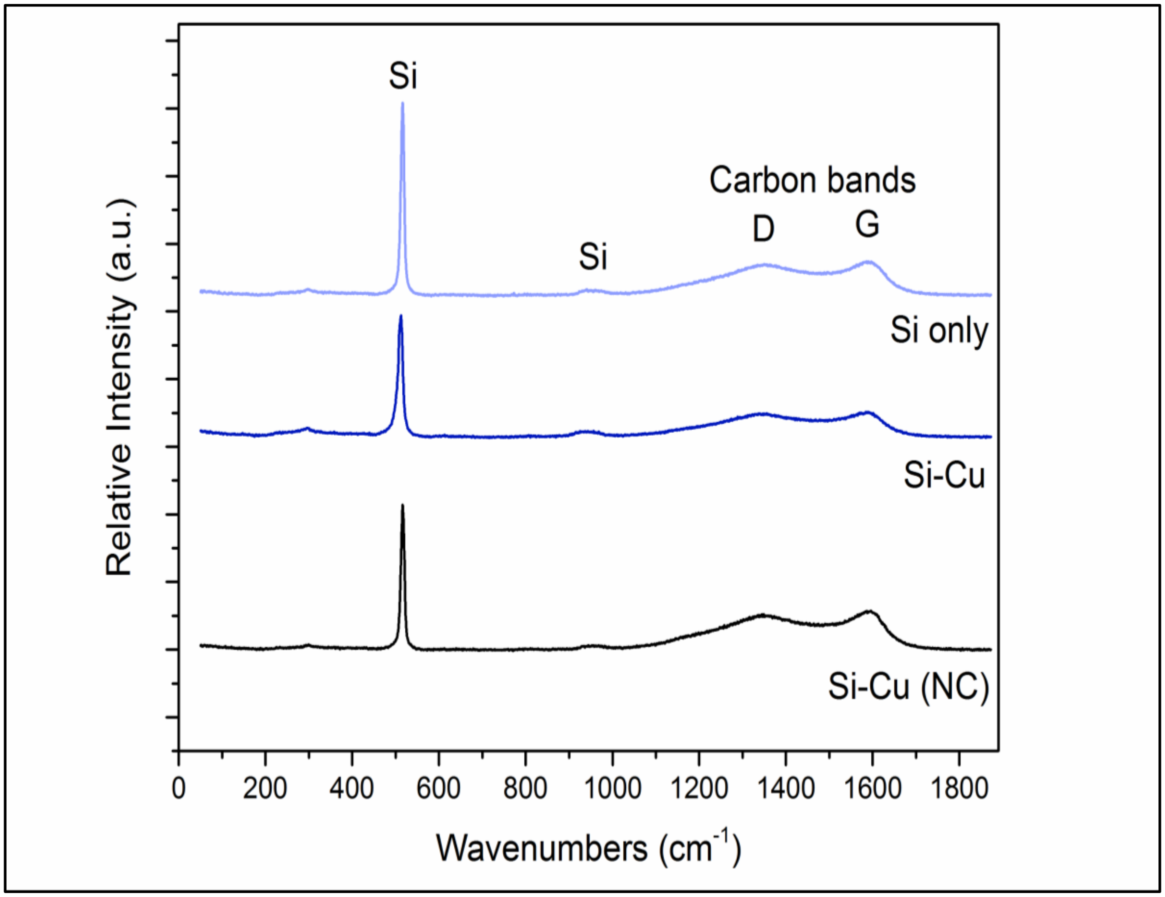

Fig. 37: Raman spectra of Si only, Si-Cu, and Si-Cu (NC) anode disc surface at 10x magnification. Silicon peaks are visible at 520 cm^{-1} and 950 cm^{-1}, and the prevalence of the amorphous carbon structure is shown from the D and G carbon bands at 1350 cm^{-1} and 1580 cm^{-1} in each of the three samples.

All samples exhibited the same four prominent peaks: two corresponding to silicon at approximately 520 cm^{-1} and 950 cm^{-1} [102-105] and two corresponding to graphite carbon [54, 96, 106]. The graphite D band and G band are visible at approximately 1350 cm^{-1} and 1580 cm^{-1} and have similar relative intensity between all three samples. The calculated intensity ratios for the two carbon bands (I_D/I_G) of the Si only, Si-Cu, and Si-Cu (NC) were 0.92, 0.96, and 0.95, respectively. The values of these ratios indicated that the carbon in the materials was of significantly amorphous quality. The prevalence of the amorphous carbon was thought to be derived from the PVP binding material during the annealing step, and groups such as Zhong *et al.* have shown in previous work that the decomposition of the PVP forms a carbonaceous structure surrounding the other particulates [107]. Though the Si-Cu (NC) sample did not have added carbon in its mixture, the amorphous carbon from the PVP and high weight percentage of PVP used seemed to have been sufficiently large enough to nullify the lack of carbon.

Raman spectroscopy revealed the presence of amorphous carbon in all three anode materials despite that no carbon was added to the Si-Cu (NC) slurry mixture. These results suggested that the addition of conductive carbon may be redundant when another conductive additive is used because carbon can be sufficiently present in the material from the carbonization of the binding agent.

To detect the presence of copper and to determine the chemistry of the anode materials following the fabrication processes, the Si only, Si-Cu, and Si-Cu (NC) samples were analyzed using XRD. Powders of the samples prepared on tantalum foil were used for this analysis. The three overall XRD patterns of the samples in the range of 2θ = 20° to 100° are shown in Fig. 38. A narrower region in the range of 2θ = 40° to 60° of the pattern for the Si-Cu (NC) material is illustrated in Fig. 39 to clearly show the first and second peaks for Cu_3Si. Table 7 includes a listing of the peak numbers, peak positions, phase and plane identifications, and the designated symbols for the patterns in Fig. 38 and Fig. 39.

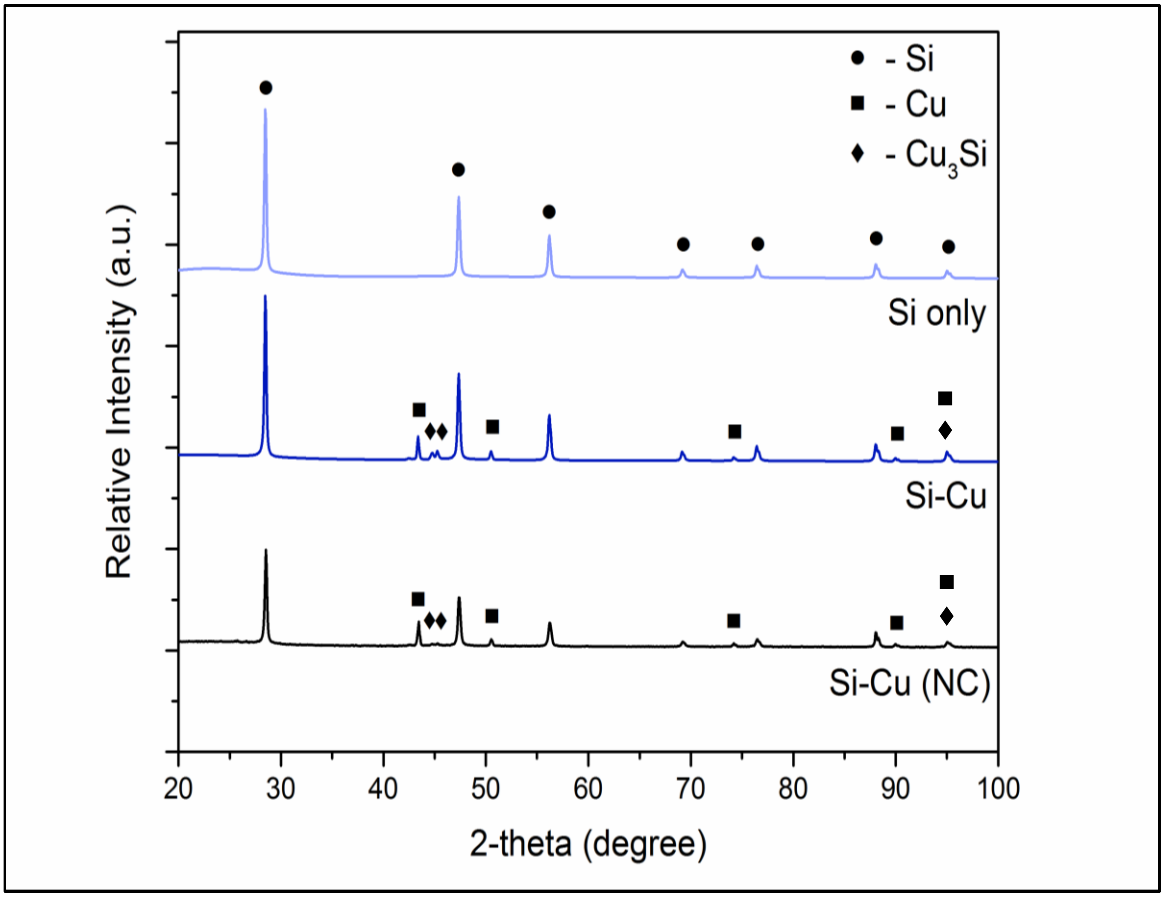

Fig. 38: XRD patterns of the Si only, Si-Cu, and Si-Cu (NC) materials between the range of 2θ = 20° to 100°. Peaks indicating the presence of Si, Cu, and Cu_3Si were identified for anodes with copper additive.

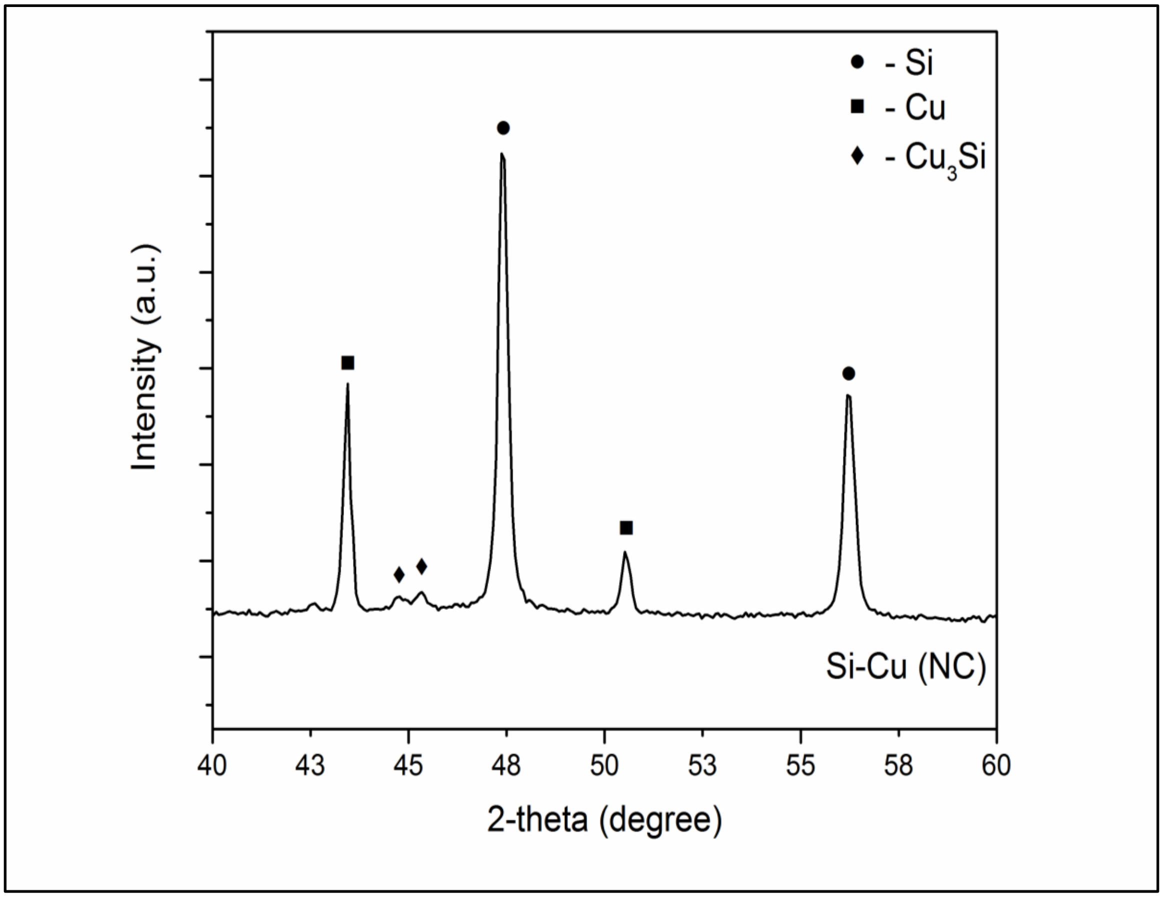

Fig. 39: Narrower region of the XRD pattern for the Si-Cu (NC) material in the range of 2θ = 40° to 60° shows the distinguished first and second Cu_3Si peaks.

Table 7: Peak positions and identification from the XRD patterns for final high-temperature anodes with copper additive.

Peak Number	2θ (deg)	Phase	Plane (h.k.l)	Symbol
1	28.48	Silicon, syn	(1 1 1)	●
2	43.37	Copper	(1 1 1)	■
3	44.73	Copper silicide	(1 1 0)	♦
4	45.24	Copper silicide	(1 0 3)	♦
5	47.35	Silicon, syn	(2 2 0)	●
6	50.50	Copper	(2 0 0)	■
7	56.16	Silicon, syn	(3 1 1)	●
8	69.16	Silicon, syn	(4 0 0)	●
9	74.15	Copper	(2 2 0)	■
10	76.41	Silicon, syn	(3 3 1)	●
11	88.07	Silicon, syn	(4 2 2)	●
12	89.99	Copper	(3 1 1)	■
13	94.98	Silicon, syn Copper Copper silicide	(5 1 1) (1 1 6) (2 2 2)	● ■ ♦

The peaks for Si are consistent with JCPDS 00-005-0565, and peaks indicating crystalline Cu (JCPDS 00-004-0836) and Cu_3Si (JPCDS 00-059-0262) are well matched with the index. It is important to recognize that copper is identified in this analysis in the metallic form and not as the original $CuCl_2$ precursor material. The XRD patterns for Si-Cu and Si-Cu (NC) also suggest that the formation of the Cu_3Si compound occurred during high-temperature heat treatment step from the copper additive, and this method of formation is well supported in literature [75, 77, 87].

Several publications attest to the benefits of Cu_3Si in the anode composition to improve stability [75, 81, 82] and electrical conductivity [81, 87], but the compound does not seem to actively participate during electrochemical reactions with lithium [82, 87]. The importance of the formation of Cu_3Si is also manifested when comparing the electrochemical results of the low-temperature anodes and high-temperature anodes in this report. As shown by the XRD analysis included in the report by Fang, *et al.*, Cu_3Si is not formed, and this absence could be contributory in part to the poor long-term performance of the anodes [78]. The results of this research reinforce the hypothesis that Cu_3Si has a distinct role in enhancing the capacity stability of the anodes; however, other structural and chemical changes in the coating from the high-temperature heat treatment may also contribute to the enhancement of anode performance.

3.3.2 Electrochemical Measurement

One of the primary goals of the initial project proposal, the enhancement of the conductivity of silicon anodes, needed to be directly addressed. To determine the effects of the copper additive on the anode resistance, EIS was performed prior to any cycle testing of the cells. The Nyquist plot of the results for the three anodes is shown in Fig. 40.

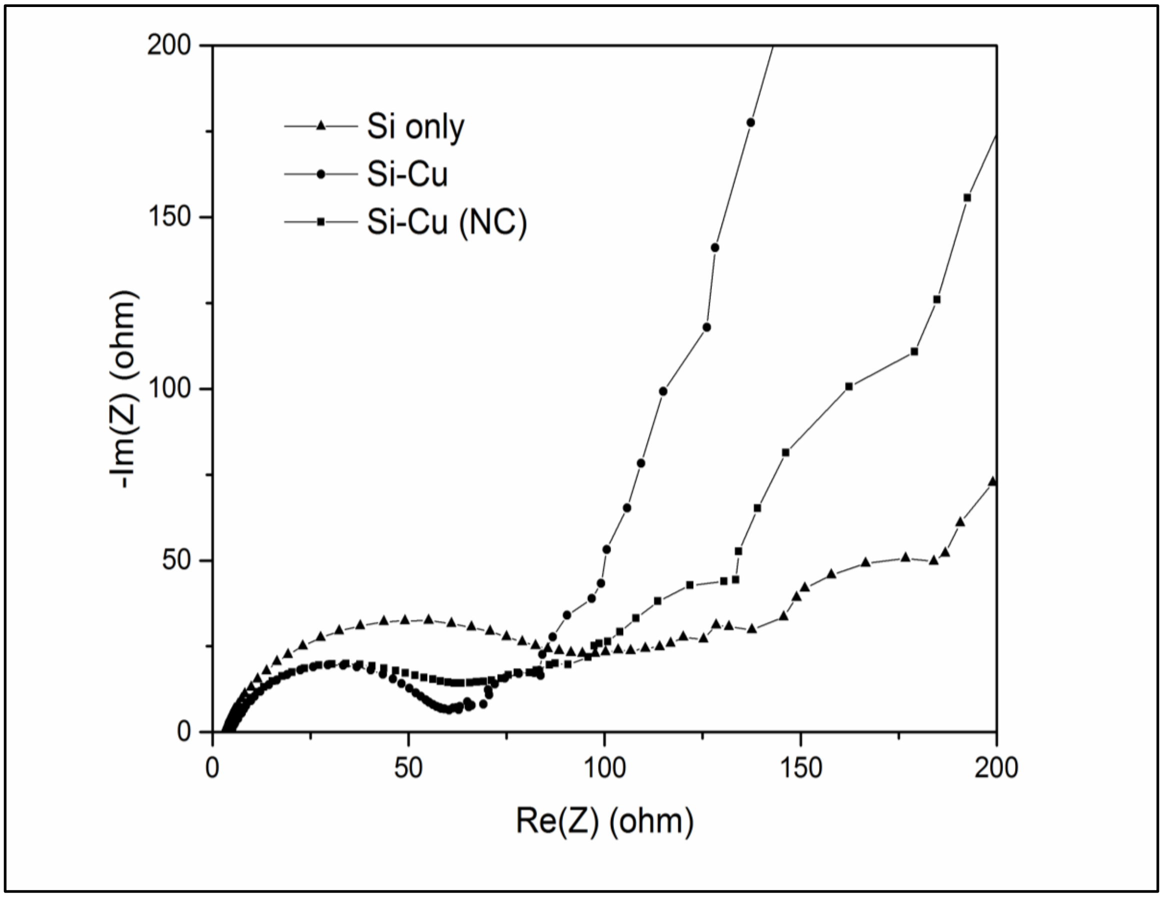

Fig. 40: EIS curves of the experimental data for the sample anodes prior to cycle testing. Resistance values are 94.04 Ω, 55.39 Ω, and 57.28 Ω for the Si only, Si-Cu, and Si-Cu (NC) samples, respectively. Thus, the addition of copper leads to increased conductivity in anodes.

As shown in the Nyquist plot, two dominant sections of each curve were apparent: the first semicircle-shaped portion and the second near-linear portion. The semicircle-shaped portion had a span in the high-to-medium frequency range, and the portion was attributed to the charge transfer resistance of the anode. The near-linear second portion in the low frequency range was attributed to the Warburg diffusion element as previously modeled in literature [101, 108]. The plot illustrated visible differences in the charge transfer resistances of the samples. The curves also confirmed that the addition of copper lead to the lowered resistivity of the anodes as shown by the resistance values of 94.04 Ω, 55.39 Ω, and 57.28 Ω for the Si only, Si-Cu, and Si-Cu (NC) samples, respectively. From the resistance value results, it was inferred that the copper additive had effectively enhanced the electrical conductivity of the anode. These results provided insight into understanding the increased performance for anodes with copper additive that have been shown throughout the entirety of this study.

EIS testing showed that Si-Cu and Si-Cu (NC) anode materials had significantly reduced resistivity than Si only, supporting the assertion that material conductivity plays an important role in anode performance. Resistivity values of the anodes with copper showed a reduction of over 40% the value of the Si only resistivity, and the overall resistivity values were generally lower than comparable results for anodes with additives reported in literature [65, 77, 78].

To assess the performance characteristics of the final high-temperature materials, the Si only, Si-Cu, and Si-Cu (NC) anode discs were also used in the fabrication of coin cells. The fabrication processes and the parameters for charge/discharge cycle testing are described in Chapter 2, and the tests were conducted for 100 cycles. The graph of the specific capacities of the three anode types as a function of cycling are shown in Fig. 41. The results for the Coulombic efficiencies of the three anodes are shown in Fig. 42.

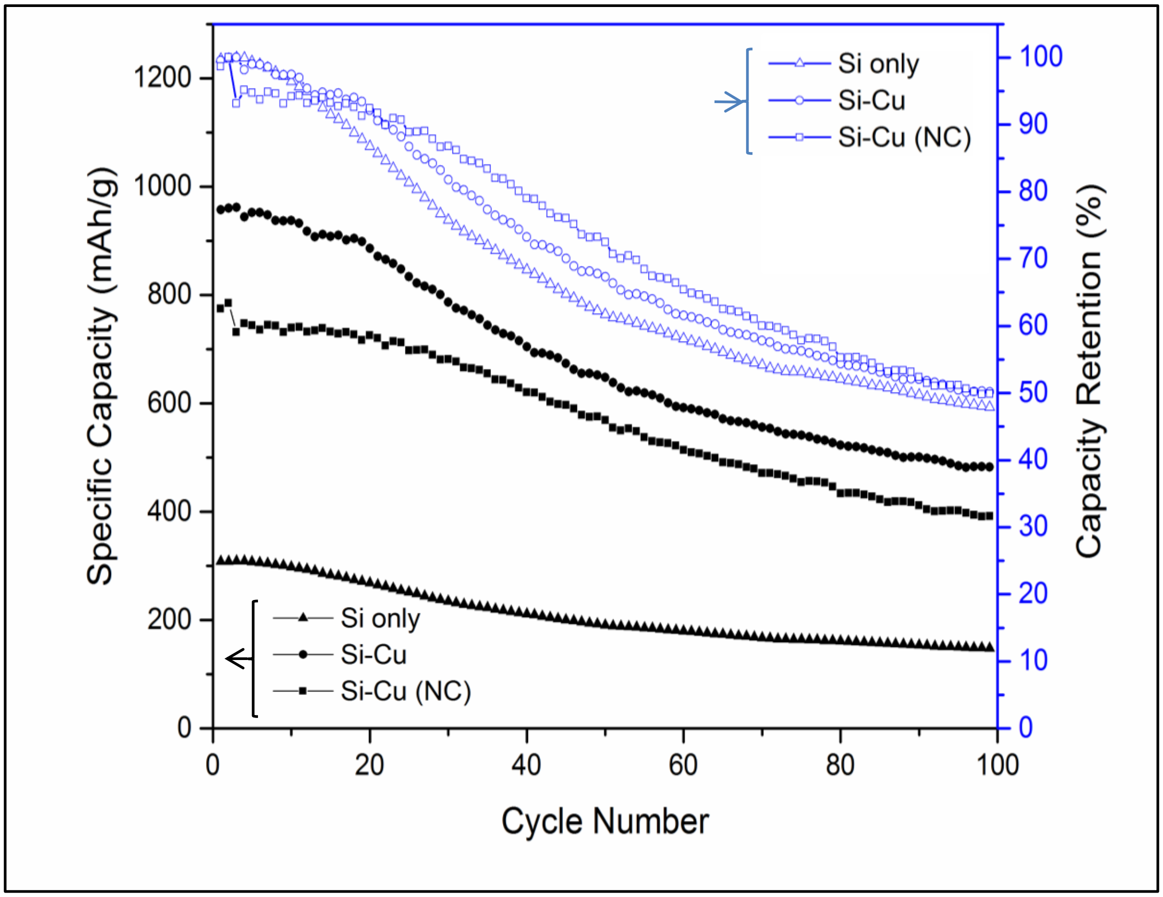

Fig. 41: Charge/discharge cycling results for 100 cycles for Si only and Si-Cu final high-temperature anodes cycled at 250 mAg^{-1} current density. Results show high initial capacity compared to previous high-temperature anodes, improved capacity retention compared to low-temperature anodes, and increased capacity for anodes with copper additive.

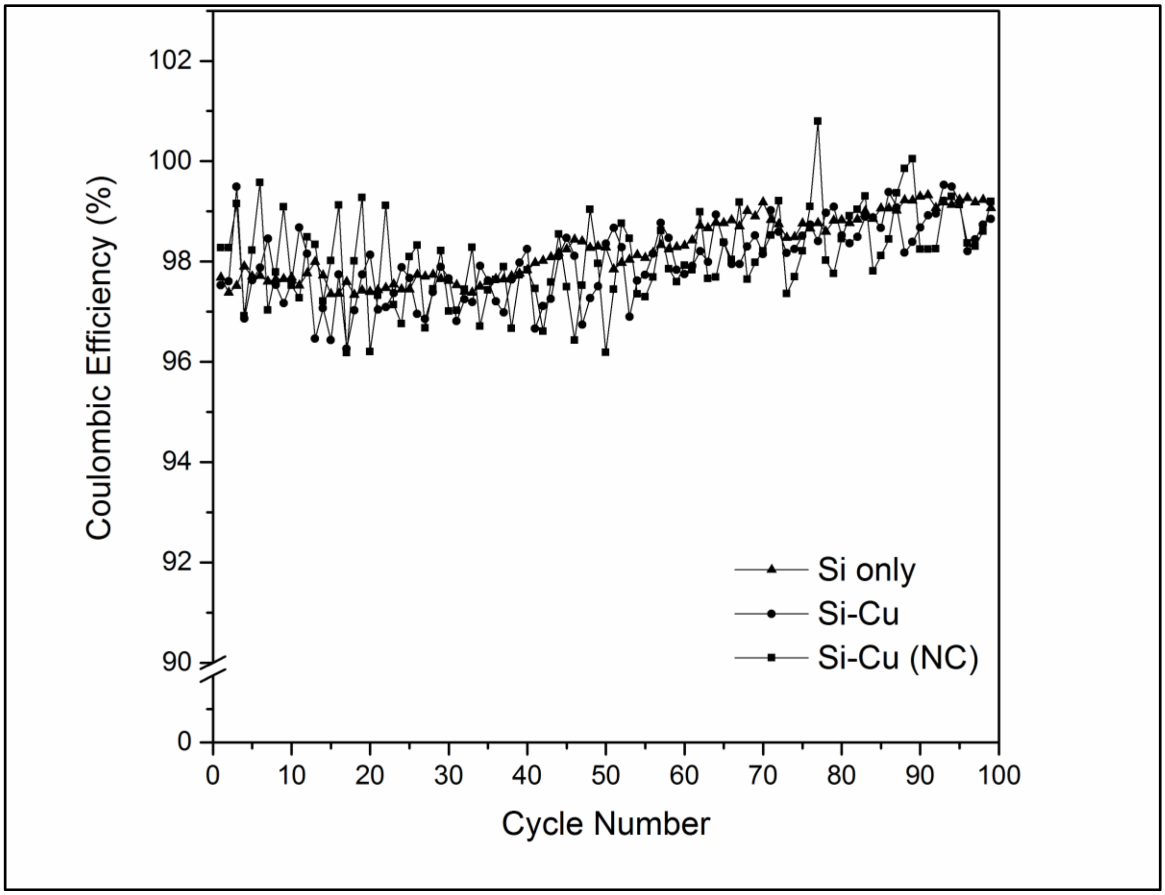

Fig. 42: Coulombic efficiency results for the Si only and Si-Cu final high-temperature anodes. Efficiency results show relative consistency between samples and overall improvement over the cycling duration.

As shown in the capacity plot, the initial specific capacities for the samples were 309 mAg^{-1}, 957 mAg^{-1}, and 775 mAg^{-1}, for the Si only, Si-Cu, and Si-Cu (NC) anodes, respectively. The final specific capacities for the one-hundredth cycle were 148 mAg^{-1}, 482 mAg^{-1}, and 391 mAg^{-1}, for the Si only, Si-Cu, and Si-Cu (NC) anodes, respectively. After 100 cycles, both anodes with copper additive had over twice the capacity of the Si only anode. These results were also comparable to similarly-fabricated anodes: samples formed by Cheng *et al.* with small quantities of added copper precursor yielded an average specific capacity of 990 mAh g^{-1} at 200 mA g^{-1} current density during cycle testing [77]. Samples prepared by Kim *et al.* also used $CuCl_2$ – though in a $CuCl_2$ to Si ratio of 2.683:1 – and achieved an initial discharge capacity of 680 mAh g^{-1} for the material during cycle testing at a constant current of 50 mAh g^{-1} [87]. The results provided in Fig. 41 showed that anodes fabricated using fewer processes and significantly less $CuCl_2$ additive were able to perform at an equal, if not advanced, level compared with anodes described in the literature.

The capacity retentions for each anode were 48% for Si only, 50% for Si-Cu, and 50% for Si-Cu (NC). These retention values were comparable to the retentions of the initial high-temperature anodes. The similarity of the Si-Cu (NC) anode with the Si-Cu anode in capacity value supported that conductivity of the anode affected cycle performance and that copper additive was capable of functioning as the sole conductive element in the coating mixture. From these results, it was again confirmed that even small quantities of copper additive dispersed in the anode structure had a noteworthy effect on the cycling performance of the anode.

Coulombic efficiencies of these anodes were relatively stable and comparable to those of the initial high-temperature anodes. Samples with copper additive displayed visibly greater variations in efficiency, but the deviations remained less than 2% of the Si only sample. Si-Cu and Si-Cu (NC) sample efficiencies were also consistently greater than 96%, reaching over 99% efficiency in the final testing cycles. The overall trend of the efficiency curves resembled the same traditional trend showed in the initial high-temperature anode results as well.

To provide an overarching comparison amongst the cycling performances of the four anode types (low-temperature, low-temperature ball milled, initial high-temperature, and final high-temperature), Fig. 43 was compiled.

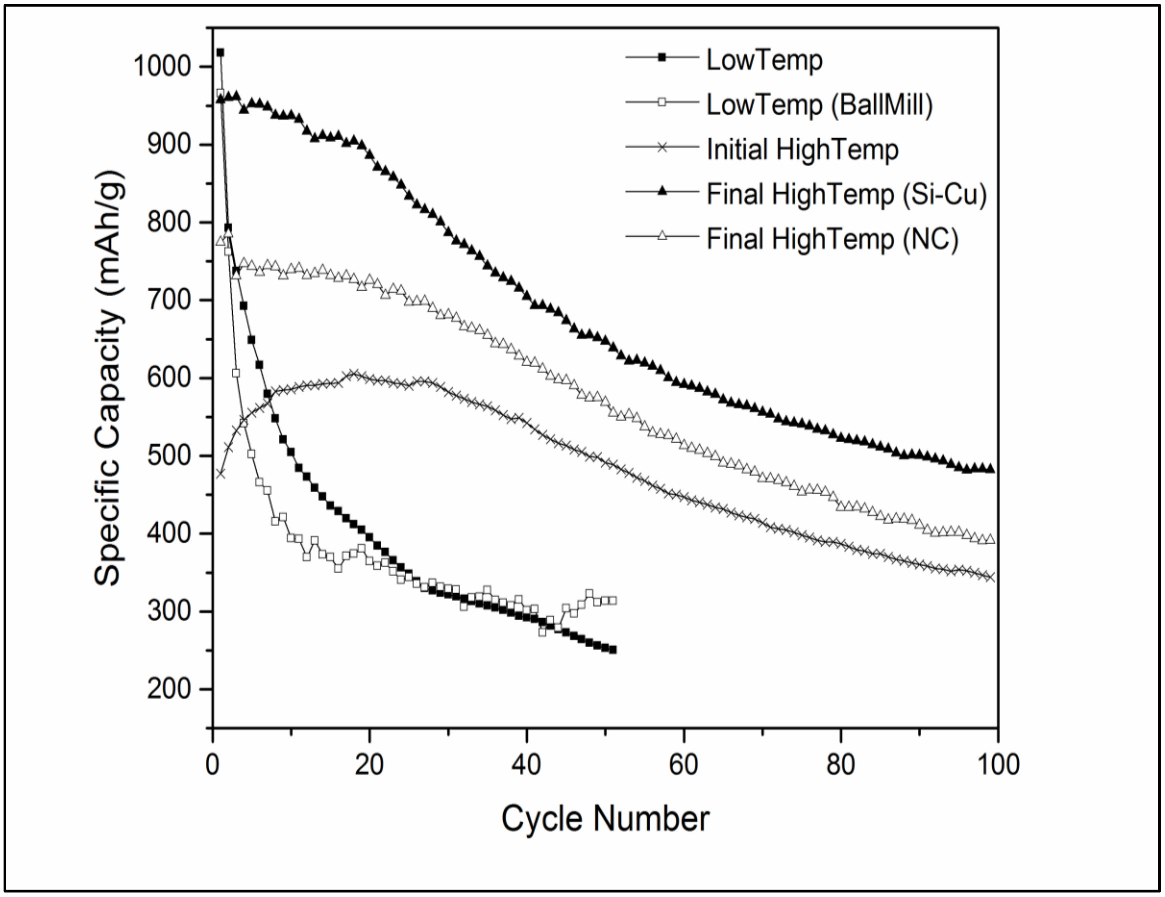

Fig. 43: Compilation graph showing the specific capacities of all anode types from this study with respect to cycling. Final high-temperature anodes demonstrated high initial and final capacity with gradual capacity fade with cycle testing.

As shown, final high-temperature anodes showed high initial and final capacity and more gradual capacity fading when compared with other anode types. Though low-temperature anodes displayed the highest initial capacities, the graph shows how quickly this becomes irreverent due to the anodes' subsequent severe capacity fading. The excellent performance of the final high-temperature anodes with copper additive functioning as the only conductive additive is also important to note as it demonstrates one of the primary goals of the final-temperature anode experiment.

Chapter 4: Conclusions

To address the need for higher-performing lithium-ion batteries, methods to improve silicon-based anode materials were explored throughout the studies in this report. Three primary studies were conducted to test the viability of using a copper additive to increase the conductivity and electrochemical performance of silicon anodes. The initial part, using low-temperature anodes, provided a proof of concept for the endeavor, and it served to establish the basic protocols for anode fabrication and testing. In this part, initial capacities of 346 mAg^{-1} and 966 mAg^{-1} were reported for Si only and Si-Cu anodes, respectively, though capacity values experienced rapid fading within the first 10 cycles. Low capacity retention and erratic efficiency data proved to be necessary issues to address in subsequent experiments. The second part, using a higher temperature heat treatment step, yielded further improvements in anode performance and higher quality data. Initial capacity values were noticeably lower than the capacity values from the first part; however, capacity retention and efficiency were improved.

The last part serves as a culmination of the knowledge gained from the previous studies. High-temperature heat treatment and optimized techniques were used to fabricate anodes with initial capacities of 309 mAg^{-1}, 957 mAg^{-1}, and 775 mAg^{-1}, for the Si only, Si-Cu, and Si-Cu (NC) anodes, respectively. Cycle testing data showed that anodes prepared with the copper additive had increased discharge capacities of over 200% compared to anodes without copper, and high efficiencies of over 96% were achieved. Electrochemical testing showed that the copper additive improved the conductivity of the anode, thus contributing to the more effective utilization of the active layer composition and enabling higher cycling performance. Results also showed that Si-Cu (NC) anodes had superior specific capacity compared to Si only anodes, indicating that copper can replace carbon black to function as the sole conductive additive. Characterization of these anode materials provided insight into the surface morphology before and after the electrochemical testing, and copper was shown to be well-integrated into the silicon-based structure. Further analysis confirmed the small percentages of copper present in the Si-Cu and Si-Cu (NC) materials, and the formation of the beneficial compound Cu_3Si following annealing was reported. These results provided an understanding of the effects of the copper additive and the mechanisms for the improvement of the anode performance characteristics.

Though the technical performance challenges were met with this study, the overarching goal of promoting methods that were economically viable, industry compatible, and sustainably minded, was also achieved. This research offers a potential low-cost, straightforward process for improving silicon anode performance. The fabrication of these anodes involved off-the-shelf ingredients with equipment and protocols that are already commonly utilized in commercial electrode manufacturing. Materials such as silicon are nontoxic and more abundant, and ethanol has garnered attention as a replacement solvent for more hazardous option such as NMP. High-temperature heat treatment is the only step that is energy-intensive, and it is also of short duration. Although anodes in this study had excellent performance relative to silicon-based anodes described in the literature, further research is necessary to form silicon anodes with cycling lifetimes comparable to commercial Li-ion battery anodes.

Chapter 5: Future Work

There are many possible avenues for future work stemming from this research. The initial experiments in the low-temperature anode study should be revisited to optimize the fabrication techniques and gain deeper insight into the mechanisms for the dramatic capacity fading within the anode's first cycles. Because low-temperature processes are desirable to conserve energy and cost at the commercial scale, improvements in the performance of these anodes would be of great value. The grainy texture of the anodes prepared in this report was thought to potentially contribute to the degradation of the anode over its cycling lifetime, so future projects could focus on ball milling strategies or particle size analysis.

It was also shown that the carbonization of the binding agent during high-temperature heat treatment in the later studies potentially played an important role in improving anode performance. Future studies could compare different binding agent materials in this application and determine a ratio of binder to active material that provides the optimum amount of carbon coating to benefit the anode and maintain proper adhesion to the current collector foil. When examining SEM images of the high-temperature anodes, small cracks in the slurry coating were already visible prior to electrochemical testing. There are several opportunities for improvement in the fabrication process that could potentially mitigate these defects. The thickness of slurry coatings and the post-casting drying techniques could be altered; the heating rate, cooldown rate, and final temperatures in heat treatment are also varying parameters throughout literature that can be assessed. Cracking could also be prevented through optimized binding agent materials.

Further evaluation of the effects of cycle testing on these types of anodes would also be a valuable contribution to the field. The advancement of silicon anodes requires improvements in several areas, notably including long-term cycling ability. Providing in-depth analysis into the failure mechanisms of these anodes through further characterization and longer-term cycling of over 100 cycles could determine which aspects of the anode are most critical to address.

Finally, there are numerous opportunities for future studies in exploring alternative conductive additives and combinations of additives therein. Novel, creative methods of incorporating metal components into the silicon structure of the anode could prove successful, and determination of the optimum quantities of additives would be helpful to balance cost and performance for the materials.

Scholarly Work

Publications:

G. Bachand, D. Chidambaram, *Improved Performance of Silicon Anodes Using Copper Nanoparticle Additive.* (Submitted for peer-reviewed journal).

Professional Presentations:

G. Bachand, D. Chidambaram, Improved Performance of Silicon Anodes Using Copper Nanoparticle Additive. Symposium Batteries and Energy Storage: Student Battery Slam A. The 232nd Meeting of the Electrochemical Society. National Harbor, MD. October 1-6, 2017.

G. Bachand, D. Chidambaram, Understanding the Degradation of Electrodes in Lithium Based Battery Systems. Fall 2016 Graduate Poster Symposium. University of Nevada, Reno Graduate Student Association. Reno, NV. November 14, 2016.

G. Bachand, D. Chidambaram, Understanding the Degradation of Electrodes in Lithium Based Battery Systems. Symposium Energy Storage VI: Materials, Systems and Applications. Materials Science & Technology 2016. Salt Lake City, UT. October 23-27, 2016.

Awards:

First Prize Presentation: Improving Silicon Anode Performance Using Copper Nanoparticle Additive. Spring 2017 Three Minute Thesis Competition, Master’s Thesis Category. University of Nevada, Reno Graduate Student Association. Reno, NV. April 20, 20167.

References

1. U.S. Energy Information Administration (EIA), *International Energy Outlook 2017*. 2017.

2. Gerland, P., et al., *World population stabilization unlikely this century.* Science, 2014. **346**(6206): p. 234-237.

3. World Energy Council (WEC), *World Energy Resources 2016*. 2016.

4. Intergovernmental Panel on Climate Change (IPCC), *Climate Change 2014 Synthesis Report Summary for Policymakers.* 2014.

5. National Institute of Environmental Health Sciences (NIEHS), *A Human Health Perspective on Climate Change: A Report Outlining the Reserach Needs on the Human Health Effects of Climate Change.* 2010.

6. McMichael, A.J., R.E. Woodruff, and S. Hales, *Climate change and human health: present and future risks.* Lancet, 2006. **367**(9513): p. 859-869.

7. Panwar, N.L., S.C. Kaushik, and S. Kothari, *Role of renewable energy sources in environmental protection: A review.* Renewable & Sustainable Energy Reviews, 2011. **15**(3): p. 1513-1524.

8. Renewable Energy Policy Network for the 21st Century (REN21), *Renewables 2017 Global Status Report.* 2017.

9. Hasanuzzaman, M., et al., *Global electricity demand, generation, grid system, and renewable energy polices: a review.* Wiley Interdisciplinary Reviews-Energy and Environment, 2017. **6**(3): p. 18.

10. Mahlia, T.M.I., et al., *A review of available methods and development on energy storage; technology update.* Renewable & Sustainable Energy Reviews, 2014. **33**: p. 532-545.

11. AECOM, *Energy Storage Study: A Storage Market Review and Recommendations for Funding and Knowledge Sharing Priorities for Australian Renewable Energy Agency.* 2015.

12. Kousksou, T., et al., *Energy storage: Applications and challenges.* Solar Energy Materials and Solar Cells, 2014. **120**: p. 59-80.

13. Moller, K.T., et al., *Hydrogen - A sustainable energy carrier.* Progress in Natural Science-Materials International, 2017. **27**(1): p. 34-40.

14. SBC Energy Institute, *SBC Energy Institute Electricity Storage FactBook.* 2013.

15. Gielen, D., F. Boshell, and D. Saygin, *Climate and energy challenges for materials science.* Nature Materials, 2016. **15**(2): p. 117-120.

16. Reddy, T.B., ed. *Linden's Handbook of Batteries, Fourth Edition*. Fourth Edition ed., ed. D. Linden. 2011, McGraw-Hill: New York, NY.

17. Poullikkas, A., *A comparative overview of large-scale battery systems for electricity storage.* Renewable & Sustainable Energy Reviews, 2013. **27**: p. 778-788.

18. Ren, G.Z., G.Q. Ma, and N. Cong, *Review of electrical energy storage system for vehicular applications.* Renewable & Sustainable Energy Reviews, 2015. **41**: p. 225-236.

19. Cho, J., S. Jeong, and Y. Kim, *Commercial and research battery technologies for electrical energy storage applications.* Progress in Energy and Combustion Science, 2015. **48**: p. 84-101.

20. Kazempour, S.J., et al., *Electric energy storage systems in a market-based economy: Comparison of emerging and traditional technologies.* Renewable Energy, 2009. **34**(12): p. 2630-2639.

21. Baumann, M., et al., *CO2 Footprint and Life-Cycle Costs of Electrochemical Energy Storage for Stationary Grid Applications.* Energy Technology, 2017. **5**(7): p. 1071-1083.

22. U.S. Energy Information Administration (EIA), *U.S. Energy Information Administration Monthly Energy Review: September 2017.* 2017.

23. Bollino, C.A., et al., *A Note on Medium- and Long-Term Global Energy Prospects and Scenarios.* Sustainability, 2017. **9**(5): p. 25.

24. Franchini, M., et al., *Association between particulate air pollution and venous thromboembolism: A systematic literature review.* European Journal of Internal Medicine, 2016. **27**: p. 10-13.

25. Center for Entrepreneurship and Technology (CET) with University of California, Berkeley, *Electric Vehicles in the United States: A New Model with Forecasts to 2030.* 2009.

26. Organization for Economic Co-Operation and Development (OECD) with International Energy Agency (IEA), *Global EV Outlook 2016: Beyond One Million Electric Cars.* 2016.

27. Wu, Y. and L. Zhang, *Can the development of electric vehicles reduce the emission of air pollutants and greenhouse gases in developing countries?* Transportation Research Part D-Transport and Environment, 2017. **51**: p. 129-145.

28. Falcao, E.A.M., A.C.R. Teixeira, and J.R. Sodre, *Analysis of CO2 emissions and techno-economic feasibility of an electric commercial vehicle.* Applied Energy, 2017. **193**: p. 297-307.

29. Hannan, M.A., et al., *Review of energy storage systems for electric vehicle applications: Issues and challenges.* Renewable & Sustainable Energy Reviews, 2017. **69**: p. 771-789.

30. Barkenbus, J., *Electric Vehicles Climate Saviors, or Not?* Issues in Science and Technology, 2017. **33**(2): p. 55-59.

31. Blomgren, G.E., *The Development and Future of Lithium Ion Batteries.* Journal of the Electrochemical Society, 2017. **164**(1): p. A5019-A5025.

32. Dell, R.M. and D.A.J. Rand, *Understanding Batteries*. 2001, Thomas Graham House, Science Park, Milton Road, Cambridge CB4 0WF, UK: The Royal Society of Chemistry.

33. Peled, E. and S. Menkin, *Review-SEI: Past, Present and Future.* Journal of the Electrochemical Society, 2017. **164**(7): p. A1703-A1719.

34. Vincent, C.A. and B. Scrosati, *Modern Batteries: An Introduction to Electrochemical Power Sources, Second Edition*. 1997, Linacre House, Jordan Hill, Oxford OX2 8DP; 200 Wheeler Road, Burlington, MA 01803: Butterworth-Heinemann.

35. Brett, C.M. and A.M. Oliveira Brett, *Electrochemistry: Principles, Methods, and Applications*. 1998, New York: Oxford Univeristy Press Inc.

36. Goodenough, J.B., *Batteries and a Sustainable Modern Society.* Electrochemical Society Interface, 2016. **25**(3): p. 66-69.

37. MTI Corporation. *Product Equipment: Battery Structure*. 2013. November 01, 2017; Available from: http://www.mtixtl.com/productimages/battery-equipment/spring%20and%20spacer%20structure-2.jpg.

38. Goodenough, J.B., *Evolution of Strategies for Modern Rechargeable Batteries.* Accounts of Chemical Research, 2013. **46**(5): p. 1053-1061.

39. Suciu, G., A. Pasat, and Ieee, *Challenges and Opportunities for Batteries of Electric Vehicles.* 2017 10th International Symposium on Advanced Topics in Electrical Engineering (Atee), 2017: p. 113-117.

40. Thackeray, M.M., C. Wolverton, and E.D. Isaacs, *Electrical energy storage for transportation-approaching the limits of, and going beyond, lithium-ion batteries.* Energy & Environmental Science, 2012. **5**(7): p. 7854-7863.

41. Armand, M. and J.M. Tarascon, *Building better batteries.* Nature, 2008. **451**(7179): p. 652-657.

42. Nitta, N. and G. Yushin, *High-Capacity Anode Materials for Lithium- Ion Batteries: Choice of Elements and Structures for Active Particles.* Particle & Particle Systems Characterization, 2014. **31**(3): p. 317-336.

43. Ma, D.L., Z.Y. Cao, and A.M. Hu, *Si-Based Anode Materials for Li-Ion Batteries: A Mini Review.* Nano-Micro Letters, 2014. **6**(4): p. 347-358.

44. Beattie, S.D., et al., *Si electrodes for li-ion batteries - A new way to look at an old problem.* Journal of the Electrochemical Society, 2008. **155**(2): p. A158-A163.

45. Su, X., et al., *Silicon-Based Nanomaterials for Lithium-Ion Batteries: A Review.* Advanced Energy Materials, 2014. **4**(1): p. 23.

46. Grey, C.P. and J.M. Tarascon, *Sustainability and in situ monitoring in battery development.* Nature Materials, 2017. **16**(1): p. 45-56.

47. Teki, R., et al., *Nanostructured Silicon Anodes for Lithium Ion Rechargeable Batteries.* Small, 2009. **5**(20): p. 2236-2242.

48. Beaulieu, L.Y., et al., *Reaction of Li with alloy thin films studied by in situ AFM.* Journal of the Electrochemical Society, 2003. **150**(11): p. A1457-A1464.

49. Baker, D.R., M.W. Verbrugge, and A.F. Bower, *Swelling and Elastic Deformation of Lithium-Silicon Electrode Materials.* Journal of the Electrochemical Society, 2016. **163**(5): p. A624-A631.

50. Orcutt, M. *The Tesla Model 3 May Depend on This Battery Breakthrough*. 2016. October 26, 2017; Available from: https://www.technologyreview.com/s/601178/the-tesla-model-3-may-depend-on-this-battery-breakthrough/.

51. Yang, Y., et al., *New Nanostructured Li2S/Silicon Rechargeable Battery with High Specific Energy.* Nano Letters, 2010. **10**(4): p. 1486-1491.

52. Son, S.B., B. Kappes, and C.M. Ban, *Surface Modification of Silicon Anodes for Durable and High-Energy Lithium-Ion Batteries.* Israel Journal of Chemistry, 2015. **55**(5): p. 558-569.

53. Zhang, Y.Z., et al., *Towards reducing carbon content in silicon/carbon anodes for lithium ion batteries.* Carbon, 2017. **112**: p. 72-78.

54. Kim, H., et al., *Preparation of silicon nanoball encapsulated with graphene shell by CVD and electroless plating process.* Journal of Industrial and Engineering Chemistry, 2017. **50**: p. 115-122.

55. Loveridge, M.J., et al., *Towards High Capacity Li-ion Batteries Based on Silicon-Graphene Composite Anodes and Sub-micron V-doped LiFePO4 Cathodes.* Scientific Reports, 2016. **6**: p. 11.

56. Ng, S.H., et al., *Highly reversible lithium storage in spheroidal carbon-coated silicon nanocomposites as anodes for lithium-ion batteries.* Angewandte Chemie-International Edition, 2006. **45**(41): p. 6896-6899.

57. Yoo, J.K., et al., *Scalable Fabrication of Silicon Nanotubes and their Application to Energy Storage.* Advanced Materials, 2012. **24**(40): p. 5452-5456.

58. Liu, W.R., et al., *Electrochemical characterizations on Si and C-coated Si particle electrodes for lithium-ion batteries.* Journal of the Electrochemical Society, 2005. **152**(9): p. A1719-A1725.

59. Zhang, R.Y., et al., *Highly Reversible and Large Lithium Storage in Mesoporous Si/C Nanocomposite Anodes with Silicon Nanoparticles Embedded in a Carbon Framework.* Advanced Materials, 2014. **26**(39): p. 6749-6755.

60. Sourice, J., et al., *Core-shell amorphous silicon-carbon nanoparticles for high performance anodes in lithium ion batteries.* Journal of Power Sources, 2016. **328**: p. 527-535.

61. Tocoglu, U., et al., *Cyclic Performance Study of Silicon/Carbon Nanotube Composite Anodes Using Electrochemical Impedance Spectroscopy.* Acta Physica Polonica A, 2014. **125**(2): p. 290-292.

62. Wang, C.S., et al., *Lithium insertion in carbon-silicon composite materials produced by mechanical milling.* Journal of the Electrochemical Society, 1998. **145**(8): p. 2751-2758.

63. Liang, B., Y.P. Liu, and Y.H. Xu, *Silicon-based materials as high capacity anodes for next generation lithium ion batteries.* Journal of Power Sources, 2014. **267**: p. 469-490.

64. Yang, X.L., et al., *Electrochemical performances of silicon electrode with silver additives.* Solid State Ionics, 2006. **177**(26-32): p. 2807-2810.

65. Zhong, L., et al., *Tin nanoparticles as an effective conductive additive in silicon anodes.* Scientific Reports, 2016. **6**: p. 8.

66. Chan, C.K., X.F. Zhang, and Y. Cui, *High capacity Li ion battery anodes using Ge nanowires.* Nano Letters, 2008. **8**(1): p. 307-309.

67. Wachtler, M., J.O. Besenhard, and M. Winter, *Tin and tin-based intermetallics as new anode materials for lithium-ion cells.* Journal of Power Sources, 2001. **94**(2): p. 189-193.

68. Winter, M. and J.O. Besenhard, *Electrochemical lithiation of tin and tin-based intermetallics and composites.* Electrochimica Acta, 1999. **45**(1-2): p. 31-50.

69. Zhang, H.G. and P.V. Braun, *Three-Dimensional Metal Scaffold Supported Bicontinuous Silicon Battery Anodes.* Nano Letters, 2012. **12**(6): p. 2778-2783.

70. Guan, H., et al., *Coaxial Cu-Si@C array electrodes for high-performance lithium ion batteries.* Chemical Communications, 2011. **47**(44): p. 12098-12100.

71. Wang, N., et al., *Highly Conductive Cu Nanoneedle-Array Supported Silicon Film for High-Performance Lithium Ion Battery Anodes.* Journal of the Electrochemical Society, 2016. **163**(3): p. A380-A384.

72. Chen, H.X., et al., *Silicon nanowires coated with copper layer as anode materials for lithium-ion batteries.* Journal of Power Sources, 2011. **196**(16): p. 6657-6662.

73. Murugesan, S., et al., *Copper-Coated Amorphous Silicon Particles as an Anode Material for Lithium-Ion Batteries.* Chemistry of Materials, 2012. **24**(7): p. 1306-1315.

74. Polat, B.D. and O. Keles, *Improving Si Anode Performance by Forming Copper Capped Copper-Silicon Thin Film Anodes for Rechargeable Lithium Ion Batteries.* Electrochimica Acta, 2015. **170**: p. 63-71.

75. Kim, J.W., et al., *Improvement of silicon powder negative electrodes by copper electroless deposition for lithium secondary batteries.* Journal of Power Sources, 2005. **147**(1-2): p. 227-233.

76. Joyce, C., et al., *Metallic Copper Binders for Lithium-Ion Battery Silicon Electrodes.* Journal of the Electrochemical Society, 2012. **159**(6): p. A909-A914.

77. Cheng, Y., et al., *Influence of copper addition for silicon-carbon composite as anode materials for lithium ion batteries.* Rsc Advances, 2016. **6**(62): p. S6756-S6764.

78. Fang, K., et al., *Facile Fabrication of Silicon Nanoparticle Lithium-Ion Battery Anode Reinforced with Copper Nanoparticles.* Digest Journal of Nanomaterials and Biostructures, 2017. **12**(2): p. 243-253.

79. Xu, K.Q., et al., *Core-shell Si/Cu nanocomposites synthesized by self-limiting surface reaction as anodes for lithium ion batteries.* Functional Materials Letters, 2017. **10**(3): p. 5.

80. Ling, L., et al., *Copper-Nanoparticle-Induced Porous Si/Cu Composite Films as an Anode for Lithium Ion Batteries.* Acs Nano, 2017. **11**(7): p. 6893-6903.

81. Kim, S.O. and A. Manthiram, *Low-cost carbon-coated Si-Cu3Si-Al2O3 nanocomposite anodes for high-performance lithium-ion batteries.* Journal of Power Sources, 2016. **332**: p. 222-229.

82. Woo, J.Y., et al., *Cu3Si-doped porous-silicon particles prepared by simplified chemical vapor deposition method as anode material for high-rate and long cycle lithium-ion batteries.* Journal of Alloys and Compounds, 2017. **701**: p. 425-432.

83. Yoon, S., et al., *Enhancement of capacity of carbon-coated Si-Cu3Si composite anode using metal-organic compound for lithium-ion batteries.* Journal of Power Sources, 2006. **161**(2): p. 1319-1323.

84. Zhou, J.B., et al., *Cu3Si@Si core-shell nanoparticles synthesized using a solid-state reaction and their performance as anode materials for lithium ion batteries.* Nanoscale, 2015. **7**(37): p. 15075-15079.

85. Kim, I.C., et al., *Electrochemical characteristics of copper silicide-coated graphite as an anode material of lithium secondary batteries.* Electrochimica Acta, 2006. **52**(4): p. 1532-1537.

86. Johnson, D.C., et al., *Synthesis of copper silicide nanocrystallites embedded in silicon nanowires for enhanced transport properties.* Journal of Materials Chemistry, 2010. **20**(10): p. 1993-1998.

87. Kim, J.H., H. Kim, and H.J. Sohn, *Addition of Cu for carbon coated Si-based composites as anode materials for lithium-ion batteries.* Electrochemistry Communications, 2005. **7**(5): p. 557-561.

88. Olesinski, R.W., G. J. Abbaschian, *The Cu-Si (Copper-Silicon) System.* Bulletin of Alloy Phase Diagrams, 1986. **7**(2): p. 170-178.

89. Solberg, J.K., *Crystal Structure of Eta-Cu3Si Precipitates in Silicon.* Acta Crystallographica Section A, 1978. **34**(SEP): p. 684-698.

90. Mima, G., M. Hasegawa, *The Diagram of Cu−Si−Zn Alloys III.* Technol. Rep. Osaka Univ., 1960. **10**: p. 157-169.

91. Mitrašinović, A., *Characterization of the Cu-Si System and Utilization of Metallurgical Techniques in Silicon Refining for Solar Cell Applications* in *Department of Materials Science and Engineering* 2010, University of Toronto: Ontario, Canada.

92. Cytermann, C., et al., *Unusual Room-Temperature Intermixing and Oxidation in Copper Deposited on a Fluorinated Amorphous-Silicon System.* Applied Physics Letters, 1988. **52**(3): p. 191-193.

93. Kasavajjula, U., C.S. Wang, and A.J. Appleby, *Nano- and bulk-silicon-based insertion anodes for lithium-ion secondary cells.* Journal of Power Sources, 2007. **163**(2): p. 1003-1039.

94. Thompson, R.D. and K.N. Tu, *Low-Temperature Gettering of Cu, Ag, and Au Across a Wafer of Si by Al.* Applied Physics Letters, 1982. **41**(5): p. 440-442.

95. Jeong, M., et al., *New approach for enhancing electrical conductivity of electrodeposited Si-based anode material for Li secondary batteries: Self-incorporation of nano Cu metal in Si-O-C composite.* Nano Energy, 2016. **28**: p. 51-62.

96. Han, P., et al., *Copper Nanoparticle-Incorporated Carbon Fibers as Free-Standing Anodes for Lithium-Ion Batteries.* Nanoscale Research Letters, 2016. **11**: p. 8.

97. Gauthier, M., et al., *A low-cost and high performance ball-milled Si-based negative electrode for high-energy Li-ion batteries.* Energy & Environmental Science, 2013. **6**(7): p. 2145-2155.

98. Cetinkaya, T., et al., *Electrochemical Characterization of the Powder Silicon Anodes Reinforced with Graphite Using Planetary Ball Milling.* Acta Physica Polonica A, 2013. **123**(2): p. 393-395.

99. Waldmann, T., et al., *Review-Post-Mortem Analysis of Aged Lithium-Ion Batteries: Disassembly Methodology and Physico-Chemical Analysis Techniques.* Journal of the Electrochemical Society, 2016. **163**(10): p. A2149-A2164.

100. Chae, O.B., et al., *Nano-scale uniform distribution of Ge/Cu3Ge phase and its electrochemical performance for lithium-ion batteries.* Electrochimica Acta, 2010. **55**(8): p. 2894-2900.

101. Guo, J.C., et al., *Cyclability study of silicon-carbon composite anodes for lithium-ion batteries using electrochemical impedance spectroscopy.* Electrochimica Acta, 2011. **56**(11): p. 3981-3987.

102. Nadimpalli, S.P.V., et al., *Quantifying capacity loss due to solid-electrolyte-interphase layer formation on silicon negative electrodes in lithium-ion batteries.* Journal of Power Sources, 2012. **215**: p. 145-151.

103. Sethuraman, V.A., V. Srinivasan, and J. Newman, *Analysis of Electrochemical Lithiation and Delithiation Kinetics in Silicon.* Journal of the Electrochemical Society, 2013. **160**(2): p. A394-A403.

104. Uchinokura, K., T. Sekine, and E. Matsuura, *Raman Scattering By Silicon.* Solid State Communications, 1972. **11**(1): p. 47.

105. Parker, J.H., D.W. Feldman, and M. Ashkin, *Raman Scattering By Silicon and Germanium.* Physical Review, 1967. **155**(3): p. 712.

106. Wang, C., et al., *A Well-Defined Silicon Nanocone-Carbon Structure for Demonstrating Exclusive Influences of Carbon Coating on Silicon Anode of Lithium-Ion Batteries.* Acs Applied Materials & Interfaces, 2017. **9**(3): p. 2806-2814.

107. Zhong, L.L., J.C. Guo, and L. Mangolini, *A stable silicon anode based on the uniform dispersion of quantum dots in a polymer matrix.* Journal of Power Sources, 2015. **273**: p. 638-644.

108. Sharma, N., et al., *Tin oxides with hollandite structure as anodes for lithium ion batteries.* Chemistry of Materials, 2005. **17**(18): p. 4700-4710.

Appendix A: Silicon Anodes

This appendix includes notes and best-practice techniques discovered during the course of the high-temperature silicon anode studies. Figure 1 shows a good example of the slurry-coated copper foil when prepared on the graphite stage. The foil was air-dried and exhibits little to no cracking on the surface. Edges on either side of the foil were folded under the stage to keep the foil flat and in place while transporting in and out of the tube furnace. The exposed top surface of the foil is approximately 15 cm long with several centimeters on either edge to accommodate folding.

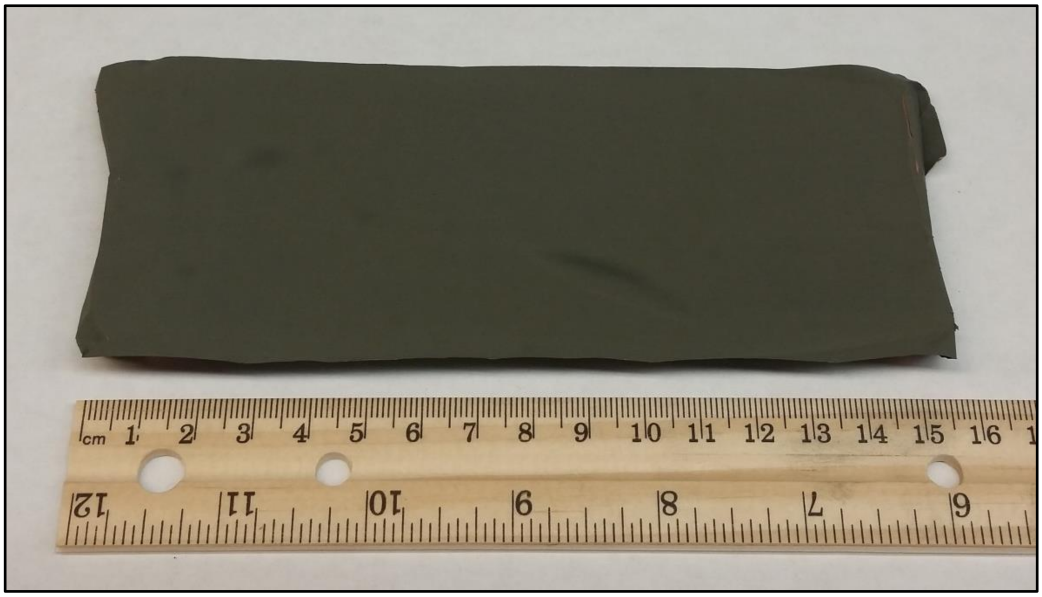

Fig. 1: A dried, slurry-coated foil prepared on the graphite stage prior to heat treatment. Edges are folded under the stage to keep the foil in flat and in place. A ruler is shown to indicate the length of the foil (approximately 15 cm exposed surface).

Cracking of the anode slurry coating was documented on several occasions, though two separate causes were determined. An example of the first form of cracking is shown in Fig. 2. The mixing step played a significant role in the success of the slurry mixture; mixing was conducted in small beakers (approximately 50 mL in size), and dry contents have the propensity to accumulate in the bottom edge of the beaker. This example shows a slurry casting where it was later noticed that the binding agent had accumulated in the edge and not fully mixed with the remainder of the slurry.

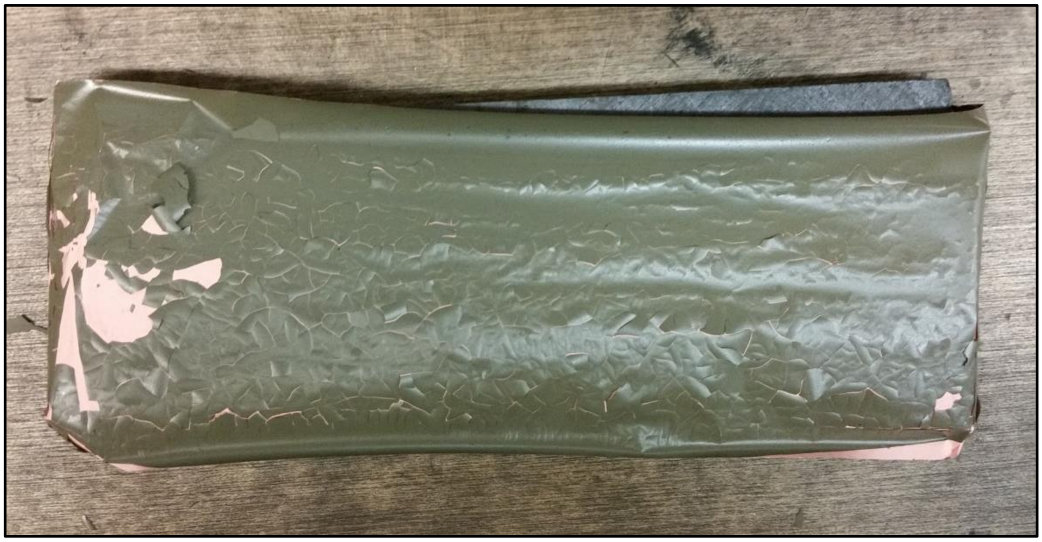

Fig. 2: A dried, slurry-coated foil with severe cracking and poor adhesion visible on the surface. During mixing, the binder was not fully integrated into the slurry.

As a result of this, the slurry is cracked and has poor adhesion to the copper foil surface. To prevent this occurrence, a spatula was used to occasionally scrape the bottom beaker edges throughout the stirring duration to ensure full mixing of the slurry contents.

Another example of cracking is shown in Fig. 3 and is attributed to the fast ramp-up heating rate programmed for the tube furnace. The foil shown had little to no evidence of cracking prior to heat treatment; following heat treatment, the foil has uniform cracking across the surface. Additional operational manuals for tube furnace heating and in literature detailing fabrication processes were consulted and suggested a slower heating rate to prevent material cracking.

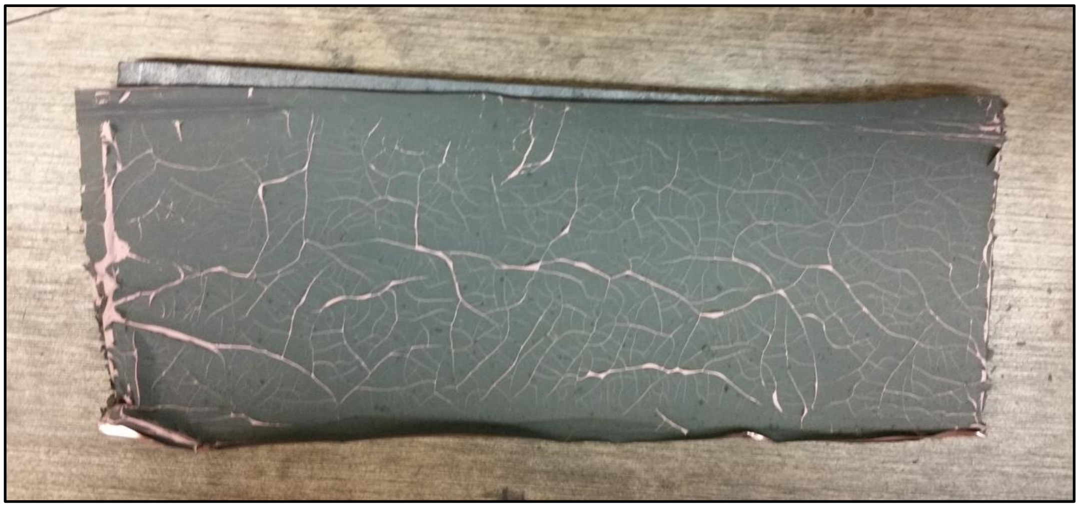

Fig. 3: A slurry-coated foil following the high-temperature heat treatment step in the tube furnace. It is speculated that the ramp-up heating rate programmed for the furnace was too fast.

A recommended rate of 5 ºC per minute was subsequently used for heat treatment, and less cracking was evident. This issue should be further explored to mitigate as much of the cracking on the anode surface as possible as cracking can propagate the degradation of the electrode.

The stirring duration of the slurry mixtures also proved to have an effect on the quality of the slurry casting on the foil. In the images included in Fig. 4, two examples of slurries with differing stirring durations are shown.

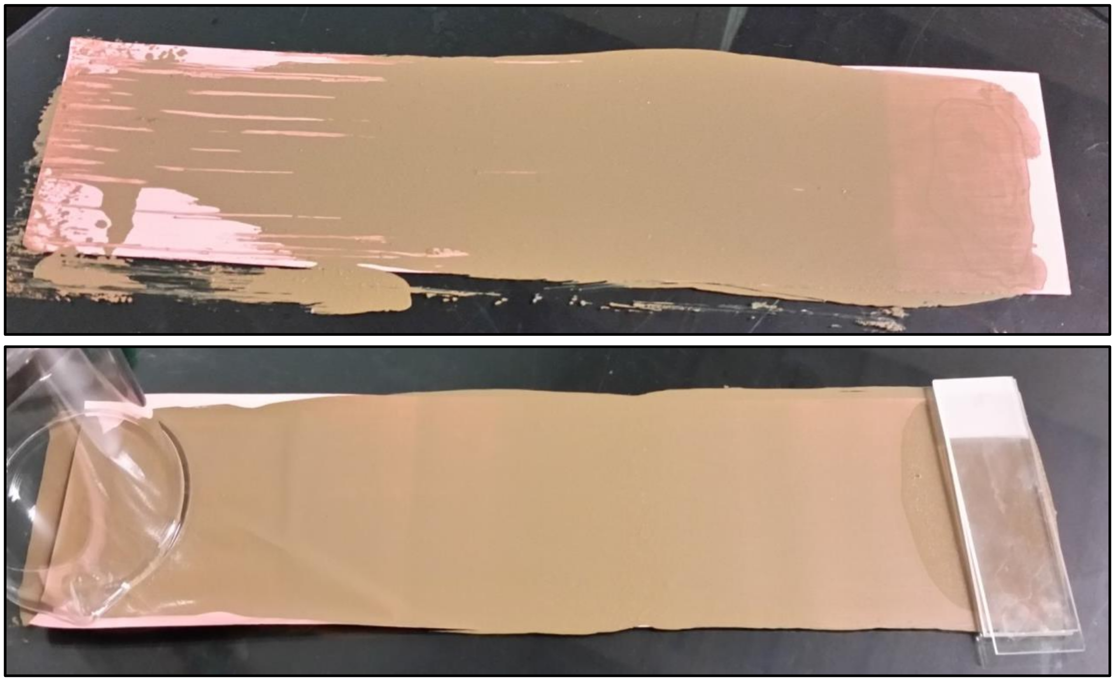

Fig. 4: Two slurry-coated foils demonstrating the importance of mixture stirring duration. The slurry in the top image was stirred for approximately five minutes and has a grainy texture. The slurry in the bottom image was stirred for over 15 minutes and has a smoother texture.

The slurry from the top image was stirred for approximately five minutes, and the slurry has a visibly grainy texture. The tail-end of the casting on the left side shows multiple scratches in the surface as a result of the large grains. The slurry in the bottom image has a stirring duration of over 15 minutes, and it shows a much smoother, more consistent texture. The slurry shows no blemishes from grains and extends the full length of the foil. Longer mixing affects the homogeneity of the slurry, and it also seems to either reduce grain size or allow more complete dissolution of the material in the solvent.

Following this preliminary test, it was determined that slurries should be mixed for an hour, and this requirement is used in all studies in this report.

Scanning electron microscopy (SEM) and energy-dispersive X-ray spectroscopy (EDS) were used to examine the samples as shown in this report. On the surface of high-temperature anodes only, the presence of contaminant particles was occasionally noticed. These particles were generally larger than surrounding particles on the surface and showed dissimilar characteristics to surroundings. Figure 5 shows the results of EDS elemental mapping of the particle located on a high-temperature anode disc. The particle is visibly comprised of aluminum and oxygen, and the background particles (and current collector foil) are shown as copper and silicon. Because this phenomenon occurs only on high-temperature anodes and because alumina blocks were used for insulating material in the tube furnace, it was concluded that the contamination was from the alumina block dust deposited on the anode surface during the vacuum purge and argon filling of the tube. Further studies should consider using a different insulating material or coating alumina blocks in a protective coating to reduce contamination.

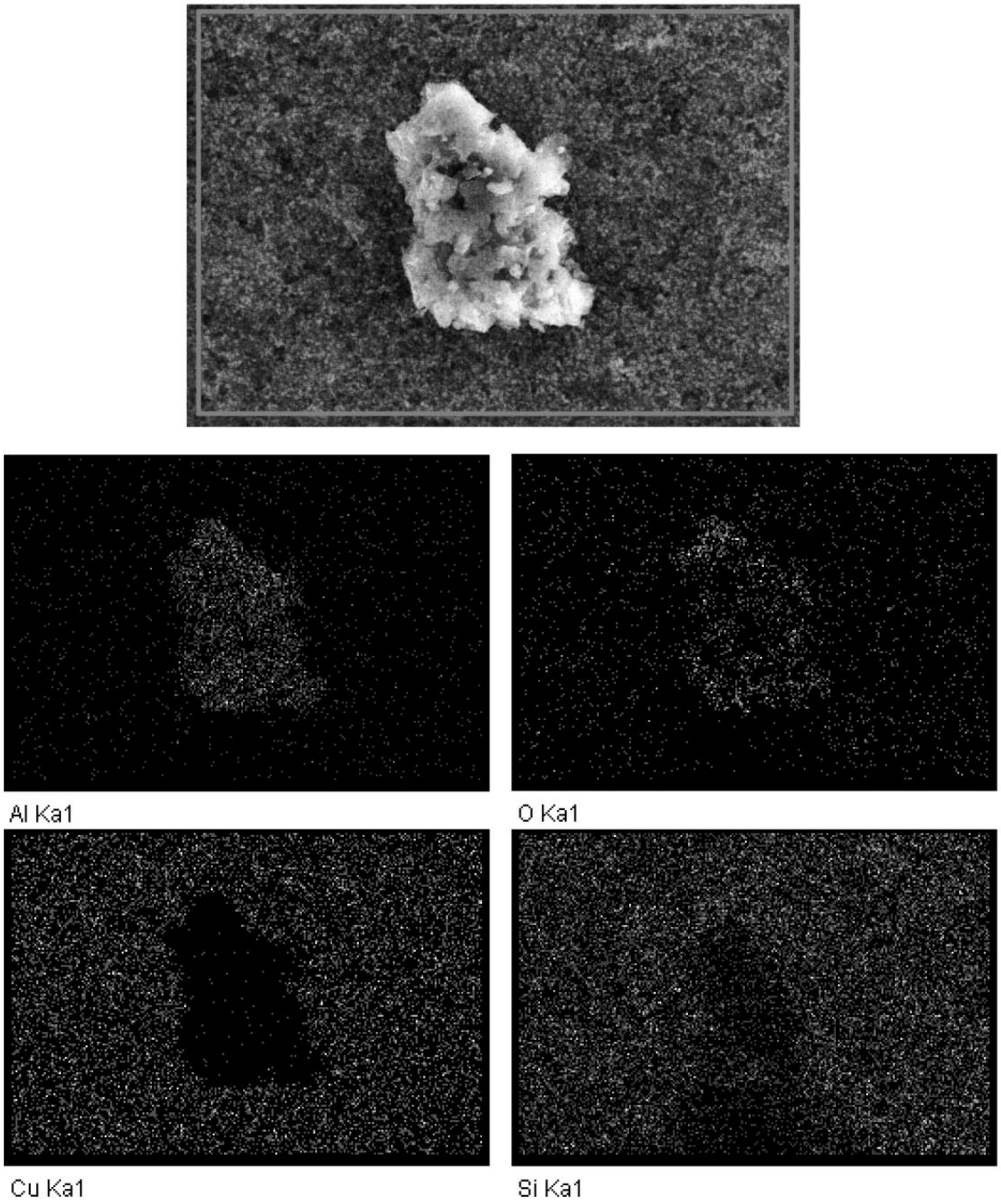

Fig. 5: SEM-EDS elemental mapping results of a contaminant on the surface of a silicon-based anode. The large particle is identified as alumina, allegedly from the alumina blocks used as insulating material in the tube furnace.

Appendix B: Fundamental Electrode Work

This appendix includes procedures and notes for the author's previous studies in electrode fabrication and in developing the Battery Laboratory protocol. Initial studies were conducted to test the functionality of electrodes using the new laboratory equipment. Graphite, the commercial standard option, was used in the fabrication of anodes; an assortment of cathodes was also made using compounds such as $LiCoO_2$, $Li(NiMnCo)O_2$, $LiMn_2O_4$, and $LiFePO_4$. The two materials with layered structure, $LiCoO_2$, $Li(NiMnCo)O_2$, were used for a general comparison study. The electrodes were fabricated using a preliminary version of the methodology described in the report for silicon anodes. Table 1 details the materials and quantities used in these experiments. The term "active material" refers to the primary electrode material: graphite was used for the anode, and $LiCoO_2$ or $Li(NiMnCo)O_2$ was used for the cathode.

Table 1: Materials and quantities for the fundamental electrode studies. The active materials used were $LiCoO_2$ or $Li(NiMnCo)O_2$ for the cathodes and graphite for the anodes.

Material	Abbreviation	Details	Manufacturer	Amount
Active Material	-	powder	MTI	4.00 g
Polyvinylidene fluoride	PVDF	powder	MTI	0.09 g
Carbon black (Super P)	CB	powder	MTI	0.09 g

The materials were dry mixed and then dissolved in approximately 3 mL of n-methyl-2-pyrrolidone (NMP, MTI) to form a homogeneous slurry. Mixtures were stirred using a magnetic stirrer at room temperature for approximately two hours. Slurries were spread on current collector foils – copper for anodes and aluminum for cathodes – using a doctor blade. Coated foils were then allowed to air dry for one hour and were heat treated in a vacuum oven at 120 ºC for three hours. Following this step, electrodes were punched into discs of 1.3 cm diameter from the coated foils.

Electrodes and 18 mm diameter cell separator discs (Celgard tri-layer PP/PE/PP membrane with 25 μm thickness) were brought into the argon-filled glove box for coin cell assembly. Membranes were allowed approximately 15 minutes to soak in electrolyte, which was a solution of 1.0M lithium hexafluorophosphate (LiPF6) in ethylene carbonate (EC) and diethyl carbonate (DEC) with a 1:1 volume ratio (Sigma-Aldrich). Coin cells were constructed using graphite anodes and various cathodes, and cells were sealed with the electric crimper. Electrochemical testing of the cells was conducted using the MTI battery analyzer; cells were cycled galvanostatically in the voltage range of 2.0 V to 4.0 V with a current density of 100 mAhg^{-1} at room temperature. Cells were typically tested for 50 cycles; longer tests were also conducted for the $LiCoO_2$ cathodes for 1000 cycles to observe long-term degradation.

The results from the cycle testing for the $LiCoO_2$ and $Li(NiMnCo)O_2$ cathodes are shown in Fig. 1 in terms of specific capacity and in Fig. 2 in terms of Coulombic efficiency. $Li(NiMnCo)O_2$ are designated as "$Li(NMC)O_2$" in the following figures.

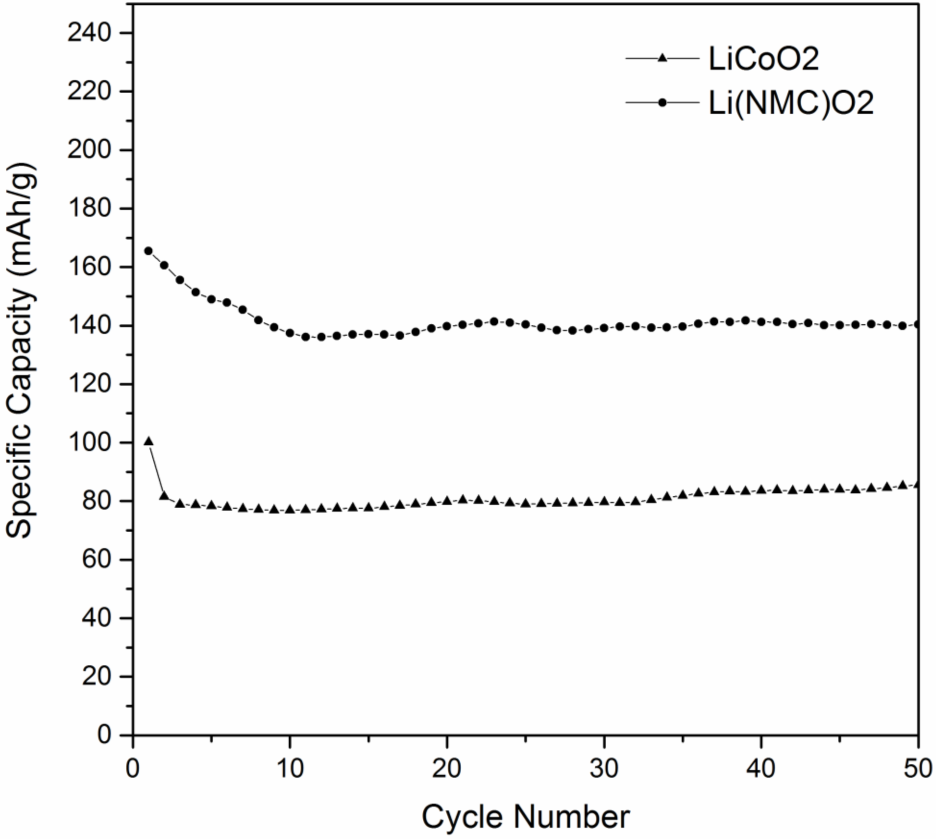

Fig. 1: Charge/discharge cycling results for 50 cycles for the $LiCoO_2$ and $Li(NiMnCo)O_2$ cathodes at 100 $mAhg^{-1}$ current density. $LiCoO_2$ and $Li(NiMnCo)O_2$ cathodes are comparable in specific capacity and exhibit significant capacity fade only within the first 10 cycles.

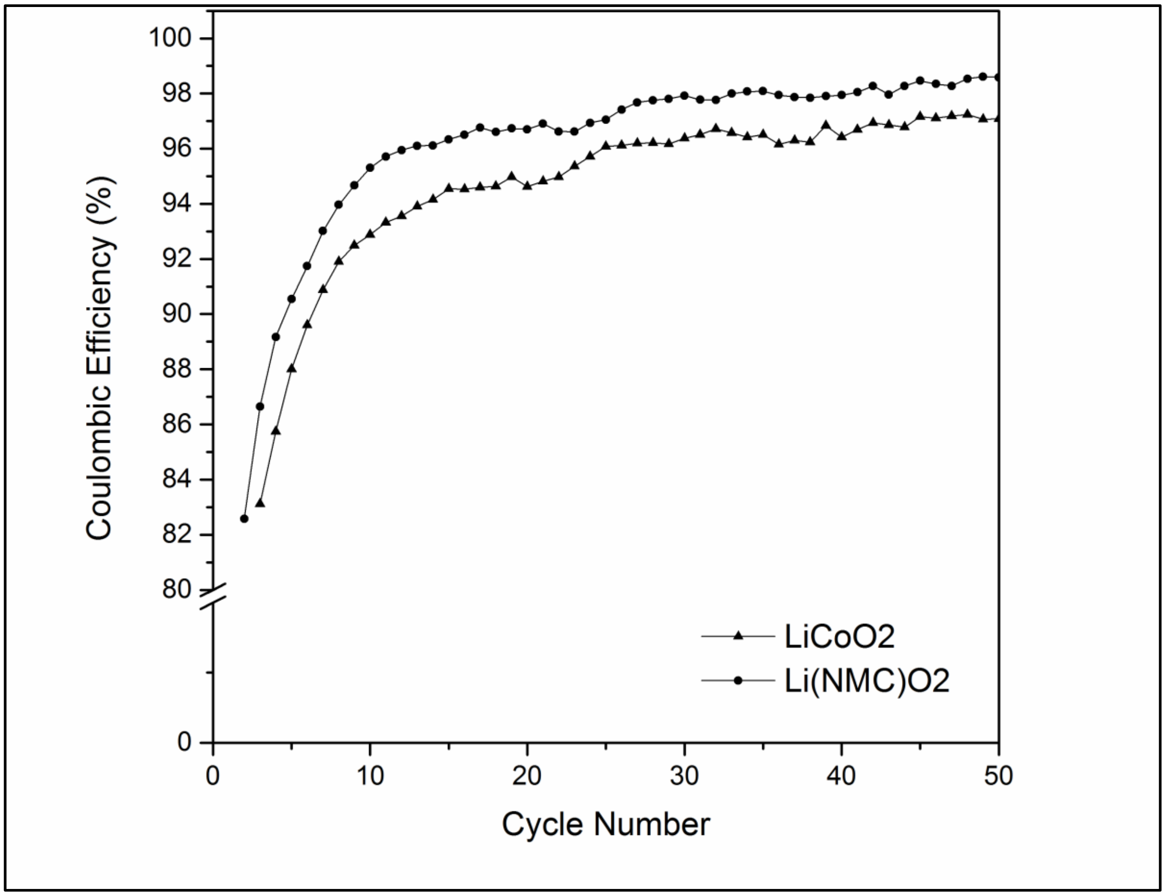

Fig. 2: Coulombic efficiency resulst for the $LiCoO_2$ and $Li(NiMnCo)O_2$ cathodes are shown. Efficiencies for both cathodes increase rapidly within the first 10 cycles and converge towards values above 96% towards the end of testing.

$LiCoO_2$ and $Li(NiMnCo)O_2$ cathodes show comparable specific capacity values and behaviors for the 50-cycle testing. The most significant capacity fade is apparent within the first 10 cycles for both cathode materials, and capacity remains stable for the remainder of testing. Coulombic efficiencies for both cathode materials are well-over 90% after the first few cycles of stabilization. Both capacity and efficiency results are representative of the already well-known characteristics of these cathode materials: these materials are commercial favorites due to their high, lasting capacity and efficiency.

To examine the long-term degradation behavior of the cells, a 1000-cycle test was conducted using the $LiCoO_2$ cathode and graphite anode. Figure 3 shows the combined capacity and efficiency results for this cathode material.

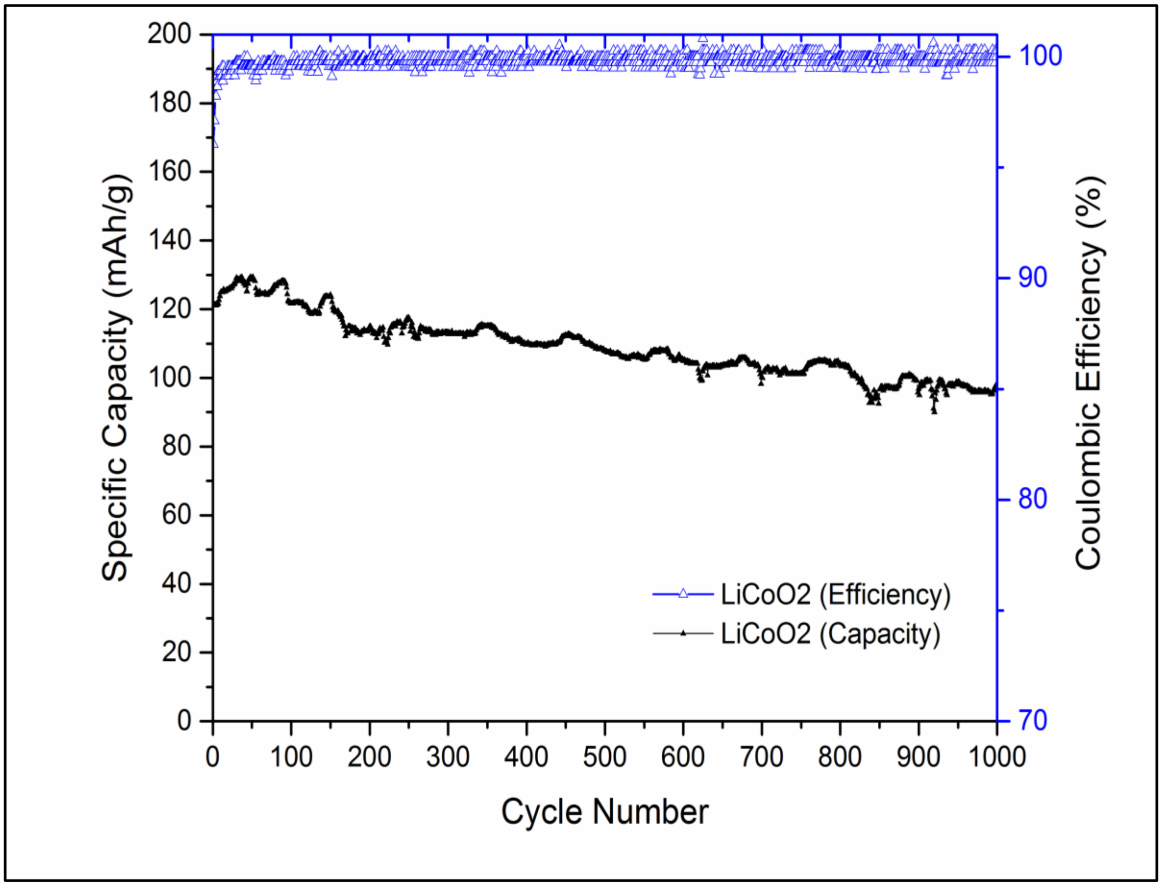

Fig. 3: Charge/discharge cycling and Coulombic effiiency results for 1000 cycles for the $LiCoO_2$ cathode at 100 $mAhg^{-1}$ current density. This test shows the long-term degradation of the cathode: the high capacity of approximately 130 $mAhg^{-1}$ eventually drops to approximately 100 $mAhg^{-1}$ after 1000 cycles. Efficiency of nearly 100% is maintained for the majority of the test duration.

Results from this study illustrate the capacity fading of the cathode over long-term cycling: though the capacity of this cathode material appeared to stabilize in the 50-cycle test, the gradual decay of the capacity is more apparent over 1000 cycles. The effiicency remains relatively stable around 100% for the duration.

Scanning electron microscopy (SEM) was also used to assess the degradation effects of cycle testing on the electrode materials. The previously described cells containing $LiCoO_2$ and $Li(NiMnCo)O_2$ cathodes and graphite anodes were cycle tested and then deconstructed for extraction of the electrodes. Electrodes were dried in the argon-filled glove box prior to SEM analysis. Cycled electrodes showed visible degradation of the material particles as shown in the images in Fig. 4. Overall views of the electrode surfaces taken at 1k-x magnification are included, and additional higher magnification images illustrate cracking on the material surfaces.

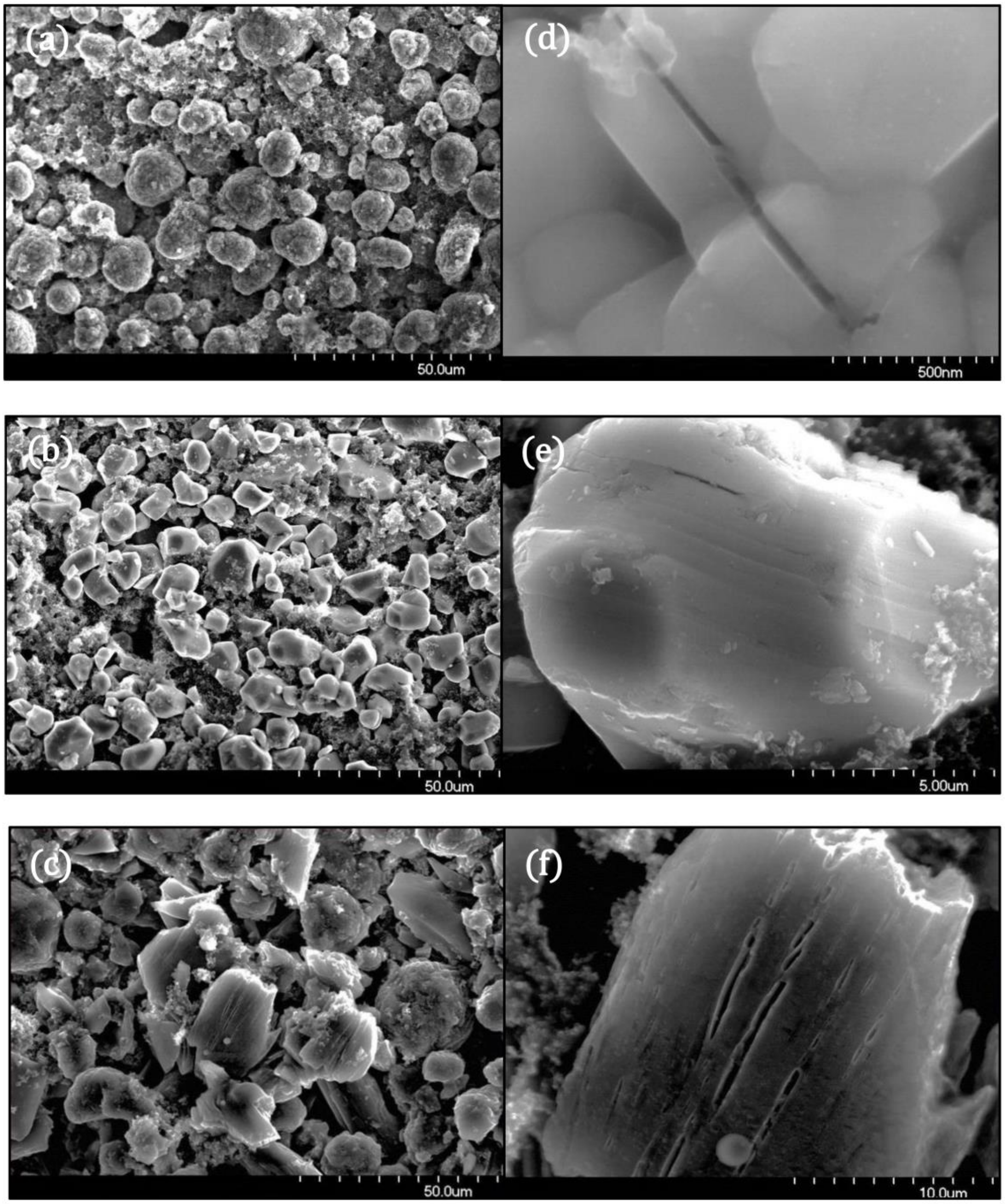
(a)
50.0um
(d)
500nm
(b)
50.0um
(e)
5.00um
(c)
50.0um
(f)
10.0um

Fig. 4: SEM images using 20 kV accelerating voltage of the anode and cathode surfaces after cycle testing for (a) Li(NiMnCo)O_2 at 1k-x magnification , (b) $LiCoO_2$ at 1k-x magnification, (c) graphite at 1k-x magnification. Detailed images showing degradation effects are shown for (d) Li(NiMnCo)O_2 at 80k-x magnification, (e) $LiCoO_2$ at 10k-x magnification, and (f) graphite at 5k-x magnification.

These images show the effects of the cycling process on the electrode materials and provide visual evidence of the electrode degradation. These results support the bulk of reports throughout literature that discuss the behaviors of commercial graphite anodes and layered cathode materials.

These experiments in the fundamentals of electrode fabrication and electrode surface analysis served three key purposes: 1) to establish fabrication protocol and effective processing techniques in the Battery Laboratory, 2) to explore testing and characterization methods to assess electrode performance and behavior, and 3) to develop methods of data collection and repeatability so that results may be compared to literature standards. These purposes were achieved, and the knowledge gained in this study provided a basis for future Battery Laboratory research in Li-ion batteries.

Appendix C: Permission for Figure Publication

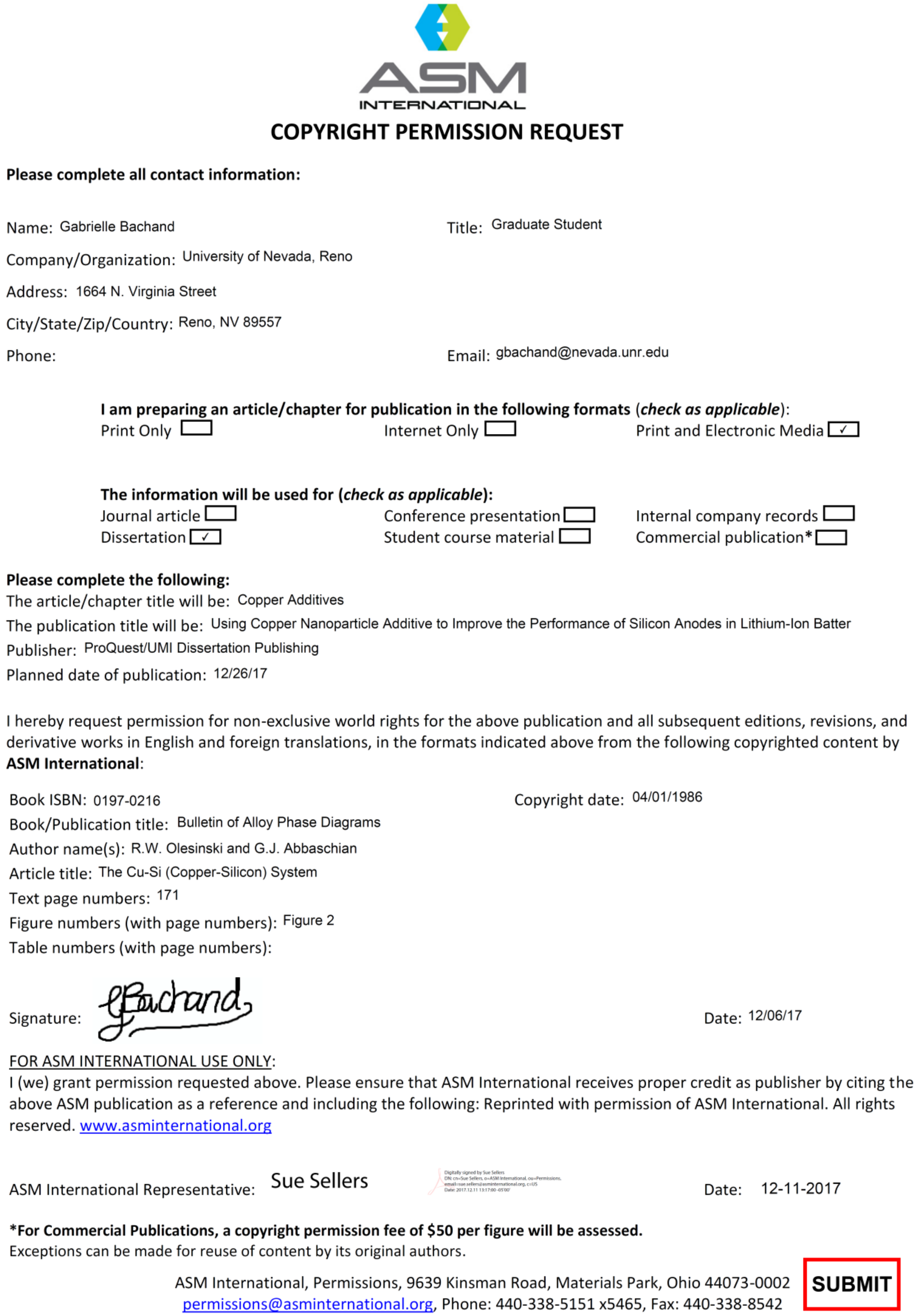

ASM INTERNATIONAL

COPYRIGHT PERMISSION REQUEST

Please complete all contact information:

Name: Gabrielle Bachand
Title: Graduate Student
Company/Organization: University of Nevada, Reno
Address: 1664 N. Virginia Street
City/State/Zip/Country: Reno, NV 89557
Phone:
Email: gbachand@nevada.unr.edu

I am preparing an article/chapter for publication in the following formats (***check as applicable***):

Print Only ☐
Internet Only ☐
Print and Electronic Media ☑

The information will be used for (*check as applicable*):

Journal article ☐
Dissertation ☑
Conference presentation ☐
Student course material ☐
Internal company records ☐
Commercial publication* ☐

Please complete the following:

The article/chapter title will be: Copper Additives
The publication title will be: Using Copper Nanoparticle Additive to Improve the Performance of Silicon Anodes in Lithium-Ion Batter
Publisher: ProQuest/UMI Dissertation Publishing
Planned date of publication: 12/26/17

I hereby request permission for non-exclusive world rights for the above publication and all subsequent editions, revisions, and derivative works in English and foreign translations, in the formats indicated above from the following copyrighted content by **ASM International**:

Book ISBN: 0197-0216
Copyright date: 04/01/1986
Book/Publication title: Bulletin of Alloy Phase Diagrams
Author name(s): R.W. Olesinski and G.J. Abbaschian
Article title: The Cu-Si (Copper-Silicon) System
Text page numbers: 171
Figure numbers (with page numbers): Figure 2
Table numbers (with page numbers):

Signature: GBachand
Date: 12/06/17

FOR ASM INTERNATIONAL USE ONLY:

I (we) grant permission requested above. Please ensure that ASM International receives proper credit as publisher by citing the above ASM publication as a reference and including the following: Reprinted with permission of ASM International. All rights reserved. www.asminternational.org

ASM International Representative: Sue Sellers
Digitally signed by Sue Sellers
DN: cn=Sue Sellers, o=ASM International, ou=Permissions, email=sue.sellers@asminternational.org, c=US
Date: 2017.12.11 13:17:00 -05'00'
Date: 12-11-2017

***For Commercial Publications, a copyright permission fee of $50 per figure will be assessed.**
Exceptions can be made for reuse of content by its original authors.

ASM International, Permissions, 9639 Kinsman Road, Materials Park, Ohio 44073-0002
permissions@asminternational.org, Phone: 440-338-5151 x5465, Fax: 440-338-8542

SUBMIT